Dynamic Stall Control: A Review

Preprint · July 2025

DOI: 10.13140/RG.2.2.21254.89924

1 author:

David Greenblatt
Technion – Israel Institute of Technology
204 PUBLICATIONS **5,527** CITATIONS

Dynamic Stall Control: A Review

David Greenblatt

Faculty of Mechanical Engineering, Technion – Israel Institute of Technology, Haifa, Israel

Abstract

The control of dynamic stall associated with wind turbine and helicopter blades, fixed-wings, flapping wings, as well as alternating flow separation and attachment produced by cyclical control inputs, is reviewed. Different airfoil and wing stall types are described, control metrics are identified, and the generality of harmonic pitch oscillations is clarified. A major emphasis is placed on nominally incompressible flows, and includes dynamic stall management, passive control devices, steady and unsteady active control techniques, scheduled control, iterative learning control, closed-loop control, flapping-wing flight, and computational predictions. Large control authority is attained by suppressing and inducing dynamic stall by means of low-frequency leading-edge slot blowing on thick airfoils, appropriate for horizontal axis wind turbine blade load control. High-frequency unsteady dynamic stall control is effective because its resultant stall-controlling leading-edge vortices are generated at more than an order-of-magnitude faster than the dynamic stall vortices. Alternating flow separation and attachment can be exploited to achieve secondary objectives, like the control of trailing vortices and enhanced turbulent mixing. Simple closed-loop control is achieved by adaptation of stall warning methods, and a feedforward/feedback control architecture is shown to be expedient and practical for gust alleviation on small vehicles. On flapping wing flyers, the roles of dynamic stall and its control are different for propulsive flight and hovering flight. For propulsive flight, active flow control can potentially be used to increase propulsive efficiency. For hovering, a relationship appears to exist between Strouhal numbers associated with insect flight, leading-edge forcing on flat-plate airfoils and low aspect-ratio flat wings, and vortex shedding. Accurate numerical predictions of dynamic stall control, namely, code validations against experimental data, have not been adequately performed, and dedicated experimental test cases for this purpose are proposed. Under subsonic compressible conditions, dynamic stall is driven by shock-induced separation, where passive leading-edge modifications with vortex generators, discrete wall-normal jet or micro-jet blowing, and dielectric barrier discharge actuation all show significant control potential.

Nomenclature

Roman Symbols

A	=	wind turbine projected area
A_j	=	blowing-slot area
A_w	=	wake-width of flapping-wing flyers
AR	=	aspect ratio, $b/\bar{c}$
AR_R	=	semi-span aspect ratio, $R/\bar{c}$
a	=	isentropic speed of sound (m/s)
b	=	wingspan (m)
C_D	=	wing drag coefficient, $F_D/q_\infty S$
C_d	=	airfoil drag coefficient, $F_d/q_\infty c$
C_L	=	wing lift coefficient, F_L/qS
C_l	=	airfoil drag coefficient, $F_l/q_\infty c$
C_m	=	¼ chord airfoil pitching moment, $m_{c/4}/q_\infty c^2$
C_n	=	airfoil normal coefficient, $F_n/q_\infty c$
$C_{\bar{P}}$	=	turbine power coefficient, $\bar{P}/q_\infty U_\infty A$
C_p	=	pressure coefficient, $(p-p_\infty)/q_\infty$
C_μ	=	steady-blowing momentum coefficient, $\rho U_j^2 h_s b/q_\infty S$ or $F_p/q_\infty c$
$\tilde{C}_\mu$	=	unsteady excitation or forcing momentum coefficient, $(1/q_\infty A_{\text{ref}})\int_{\text{act}} \rho U_{\text{act}}^2 dA_{\text{act}}$
c	=	airfoil chord-length (m)
$\bar{c}$	=	wing average chord-length (m)
D	=	diameter (m)
D_t	=	turbulent diffusion (m^2/s^3)
d.c.	=	duty cycle
F	=	force per unit span (N/m)
F_p	=	plasma axial body force per unit span (N/m)
F^+	=	airfoil (section) reduced frequency, $f_p c/U_\infty$ or $f_p c/V_{\text{rel}}$
f	=	airfoil pitching frequency (Hz)
f_f	=	wing flapping frequency (Hz)
f_{ion}	=	plasma ionization frequency (Hz)
f_p	=	perturbation or pulse-modulation frequency (Hz)
f_{shed}	=	vortex shedding frequency (Hz)
h	=	time-dependent plunging amplitude (m)
h_0	=	plunging motion amplitude (m)
h_j	=	blowing-slot-jet width (m)
k	=	airfoil reduced pitching frequency $\pi fc/U_\infty$
k_f	=	flapping wing reduced frequency, $\pi f_f c/U_\infty$
$k_i(\phi)$	=	instantaneous reduced pitching frequency $\pi fc/U_\infty(\phi)$
k_n	=	nominal reduced frequency in a surging flow, $\omega c/2\bar{U}_\infty$
L	=	body dimension in the perpendicular to the freestream (m)
M	=	isentropic Mach number, U_∞/a
N	=	number of blades
P	=	wind turbine power output (W)
$\bar{P}$	=	average power input (W)
$\bar{P}_{\text{in}}$	=	average power input to plasma actuators (W)
q_∞	=	dynamic pressure, $\frac{1}{2}\rho U_\infty^2$ (Pa)
R	=	rotor radius or wing semi-span (m)

Re = airfoil Reynolds number, $U_\infty c/\nu$
r = radial distance (m)
$\hat{r}$ = dimensionless radial distance, r/R
S = wing planform area (m^2)
St = conventional Strouhal number, $f_{\text{shed}}L/U_\infty$
St_{hf} = hovering flight Strouhal number
St_{pf} = flapping-wing Strouhal number, $f_f A_w/\bar{V}$
St^+ = actuation Strouhal number, $F^+ \sin\alpha$
T = characteristic time-scale (s)
$\bar{T}$ = average thrust (N)
U_0 = circular jet core velocity (m/s)
U_∞ = freestream wind speed (m/s)
$\bar{U}_\infty$ = average freestream velocity in a surging flow (m/s)
U_j = jet-slot velocity (m/s)
U_e = boundary layer edge velocity (m/s)
U_r = rotor blade speed (m/s)
$\bar{V}$ = forward flight speed
V_{rel} = velocity relative to the blade or wing (m/s)
V_{tip} = blade tip speed
$V_\parallel$ = velocity component parallel to the chord
W = wind speed (m/s)
X = internal dynamic variable for Goman-Khrabrov model
X_p = distance from perturbation location to trailing-edge (m)
x = chordwise coordinate from the leading-edge (m)
x_c = strut blade connection point (m)
x_p = pitch axis
y = spanwise coordinate direction (m)
x_s = chordwise slot location (m)
z = coordinate normal to the chord plane (m)
z' = virtual camberline (m)

Greek Symbols

α = angle-of-attack (° or rad)
α_{eff} = maximum effective angle-of-attack (° or rad)
α_m = average angle-of-attack (° or rad)
α_1 = angle-of-attack amplitude (° or rad)
α_s = static stall angle-of-attack (° or rad)
$\dot{\alpha}$ = angle-of-attack pitchrate (rad/s)
β = flapping-wing stroke plane
Γ = circulation (m^2/s)
γ = vortex sheet strength (m/s)
δ_f = flap deflection angle (° or rad)
ε = chord-to-radius ratio, c/R
ζ_z = z component of vorticity
θ = wind turbine azimuthal angle (° or rad)
$\hat{\theta}$ = flapping-angle normal to the stroke-plane (° or rad)
κ = dimensionless pitchrate, $\dot{\alpha}c/2U_\infty$
λ = wind turbine tip-speed ratio, $\omega R/U_\infty$

λ_f = inter-flap spacing (m)
μ = helicopter rotor advance ratio, $\bar{V} / \Omega R$
ν = fluid kinematic viscosity (m^2/s)
Ξ_{cycle} = cycle-averaged aerodynamic damping
ρ = fluid density (kg/m^3)
σ = relative surging velocity amplitude
τ_1, τ_2 = Goman-Khrabrov time-constants (s)
$\tilde{\tau}$ = dimensionless characteristic time-scale
Φ = full-stroke (peak-to-peak) flapping amplitude (° or rad)
ϕ = phase angle with a cycle, ωt (° or rad)
$\hat{\phi}$ = flapping-angle within the stroke plane (° or rad)
$\Delta\phi$ = phase-difference between angle-of-attack and freestream velocity (° or rad)
Ψ = helicopter azimuthal angle (° or rad)
Ω = rotor rotational speed (rad/s)
ω = pitching cycle rotational frequency (rad/s)

Abbreviations

AC = alternating current
AFC = active flow control
AV = aft vortex
att = attachment
DC = direct current
FHAWT = floating horizontal axis wind turbine
FWUAV = flapping-wing unmanned aerial vehicle
HAWT = horizontal axis wind turbine
LES = large-eddy simulation
LEV = leading-edge vortex
LSB = laminar separation bubble
MAV = micro aerial vehicle
NAV = nano aerial vehicle
PSD = power spectral density
RBS = retreating-blade stall
sLEV = swept leading-edge vortex
sUAV = small unmanned aerial vehicle
sep = separation
TV = (wing) tip vortex
TDD = time delay-and-decay
UAV = unmanned aerial vehicle
VAWT = vertical axis wind turbine
VG = vortex generator

Table of Contents

1 Introduction

Dynamic stall commonly denotes the process of unsteady flow separation from a lifting surface, and is present in rotary-wing, fixed-wing, and flapping-wing engineering systems. It may occur due to a change in the body's motion or orientation with respect to the flow [1], a change in the external flowfield [2], a change in a control input [3], or seemingly spontaneously [4,5]. Two major drivers of cyclical dynamic stall research are helicopter and wind turbine blade aerodynamics. On helicopter blades, dynamic stall manifests mainly on the retreating blades when the static stall angle is exceeded, and results in asymmetric lift, large blade pitching moments, negative damping, and vibrations that affect control and fatigue life [6-8]. On horizontal and vertical axis wind turbines (VAWTs and HAWTs), dynamic stall affects both performance and fatigue loading [9,10]. On large-scale fixed wing aircraft dynamic stall does not occur routinely, and it can be exploited for enhanced maneuverability [11]. On smaller scale fixed-wing aircraft, like unmanned air vehicles and small unmanned aerial vehicles (UAVs and sUAVS), atmospheric gusts can compromise stability and controllability [2,12]. At even smaller scales, where flapping-wing biomimicry is exploited—typically in the micro and nano UAV range—dynamic stall is either a limiting factor, e.g. for propulsive flight [13], or a necessary factor, e.g., for hovering flight [14,15].

Fundamental and applied research performed up until the 1980s was summarized in the landmark reviews of [16] and [17]. Subsequently, detailed and informative reviews have appeared that address computational prediction methods [18], effects of compressibility [19,20] and experimental advances, including flow control [1]. Since the turn of the century, there has been a dramatic increase in dynamic stall research [1], and the demand for effective control has increased accordingly. The objectives of control depend on the specific technological or scientific objectives, and these vary considerably. For example, on helicopter blades [1], wind turbine blades [21], and small UAVs [22], the objective of control is usually the elimination or minimization of negative aerodynamic effects. In contrast, on rapidly pitching wings [11], flapping wings in hover [23], and high solidity VAWTs [24], the objectives are often aimed at exploiting dynamic stall to maximize performance.

Actuation methods for dynamic stall control are generally categorized as fluidic, mechanical, thermal, or plasma-based, as well combined-hybrid systems [25]. Independent of the actuation method, flow initially separated from a body can be forced to attach dynamically, following a change to the control input, e.g., amplitude or frequency [26]. Conversely, an initially attached flow can separate from a body, e.g., by terminating actuation [3]. The temporal

behavior of the flow and the resulting loads on the body, i.e., the timescales characterizing separation and attachment, determine the actuation bandwidth [27]. (We reserve the term "reattachment" to indicate flows that separate and re-attach on the same surface, for example, laminar separation bubbles, LSBs.) In addition, by varying control inputs, dynamic stall control can be used to achieve secondary objectives, unrelated to aerodynamic performance [28].

This review begins with a description of the most common occurrences of technological importance in section 2, and the main control objectives are identified. This is followed by a review of incompressible control in sections 3, which makes up a major part of this review: First, the different types of stall are identified and then different approaches to control are presented and discussed. Section 4 is dedicated to discussing the effects of compressibility, mainly with application to helicopter blade flows, and the unique challenges presented in this flow regime. Section 5 presents a summary of the review, with the author's own suggestions for future research and development.

2 Occurrences & Objectives

To set the scene, we will briefly describe the most commonly encountered, technologically relevant, occurrences of dynamic stall and the specific control objectives. These include occurrences on helicopter and wind turbine blades, fixed-wing aircraft wings, flapping wings, and those associated with control inputs. In this review, we take a broad perspective of dynamic stall control that includes unsteady separation and/or attachment of flows responding to a change in control input. For cyclical flows like those on helicopter and wind turbine blades, or those subjected to a periodic input we refer to the entire cycle—including attachment of the flow—as the dynamic stall cycle.

2.1 Helicopter Blades

On conventional (non-compound) helicopters in high-speed forward flight, the blade relative dynamic pressure on the rotor is imbalanced. Therefore, blades are required to periodically pitch, such that the changes in angle-of-attack produce a net average uniform lift force across the rotor [7,8]. As the forward flight speed increases, the angle-of-attack excursions increase, exceeding the static stall angle, which leads to dynamic stall—which is dominated by a leading-edge vortex (LEV). (In many studies, the LEV is referred to as the dynamic stall vortex (DSV); we will use LEV, to distinguish it from other vortices that may form during dynamic stall.) During the last two decades, increases in engine power have brought about renewed focus on dynamic stall control [29]. A major challenge for the control of retreating blade stall (RBS) is that compressibility effects are significant and dynamic stall near the blade tip is precipitated by shock-induced separation [16].

A rotor disk map for steady level flight of a Sikorsky UH-60A rotor is shown in Figure 1 (left) [30,31], where dynamic stall occurs predominantly on the retreating blade—hence the moniker RBS [32], i.e., in quadrants 3 and 4. Corresponding normal force and pitching moment, based on integrated surface pressures, are shown for the third and fourth quadrants at $r/R = 0.865$ (Figure 1, right). The map and data also show the following: two dynamic stall events, pitching moment stall always precedes lift stall, and the rate and amplitude of unsteady moment changes during attachment are at least as large as those during separation (dynamic stall). These effects are exacerbated during high maneuvers, such as a sudden pull-up or a high-speed diving turn, where dynamic stall extends to the first quadrant as well [30,31]. A Mach number map (Figure 1, center), based on the idealized representation of the in-plane normalized velocity magnitude distribution parallel to the chord-line, shows that dynamic stall occurs under both compressible and incompressible conditions. The primary objective, therefore, is to

eliminate dynamic stall, or at the very least to weaken its negative effects—particularly moment stall—in the both compressible and incompressible flow regimes. A major challenge is to develop effective and viable control methods that cut across the incompressible-compressible divide.

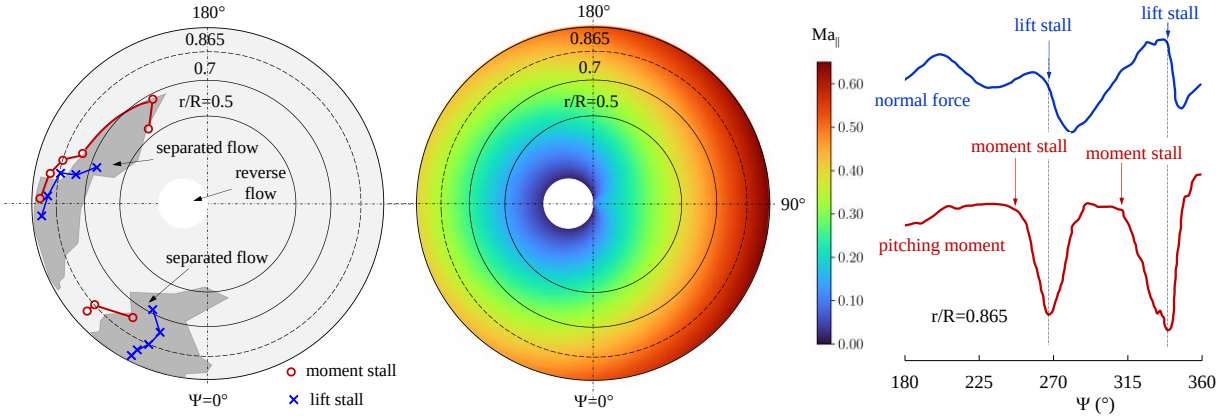

Figure 1. Left: Rotor disk map showing dynamic stall events on a Sikorsky UH-60A rotor in steady level flight at $\mu = 0.237$ (load factor = 1.01) [30,31]. Middle: Corresponding idealized in-plane Mach number map parallel to the chord-line. Right: Blade loads at $r/R = 0.865$ as a function of azimuthal angle in quadrants 3 and 4 [30,31].

Some compound helicopters [33-35] represent an attempt to eliminate RBS [20,1]. For example, coaxial, nominally rigid rotors [36-38], rotate in opposite directions, and achieve high advance ratios. An in-plane velocity map, is shown for a typical advance ratio $\mu = 0.77$ in Figure 2 [39]. While the blades avoid conventional RBS, they experience synchronous high-amplitude velocity oscillations, as well as pre-static-stall angle-of-attack $(\alpha < \alpha_s)$ oscillations due to aeroelasticity and interactions between the rotors [35]. Near the tips, blades experience chordwise flow oscillations—also called surging—amplitudes of up to 90% [39], while further blades are exposed to regions of reverse-flow $(\sigma > 1)$, i.e., flow from the trailing-edge to the leading-edge. In contrast to pitching and plunging airfoils (see reviews [1,40] amongst others), far less attention is paid to the surging problem [41-51], primarily due to technical difficulties at relevant flight Reynolds numbers and Mach numbers. Unsteady experimental surging studies with a reverse-flow component are limited to water tunnels and water-filled towing tanks with $\overline{Re} < 10^5$ [47,48]. In particular, very little is known about how surging dynamic stall occurs and how it affects rotor performance; in particular, the behavior of combined forward- and reverse-flow separation bubble-types shown illustratively in Figure 2 (adapted from [39,49,50]). For

these problems, the objectives are to first gain an understanding of dynamic stall and then to propose methods for effective control.

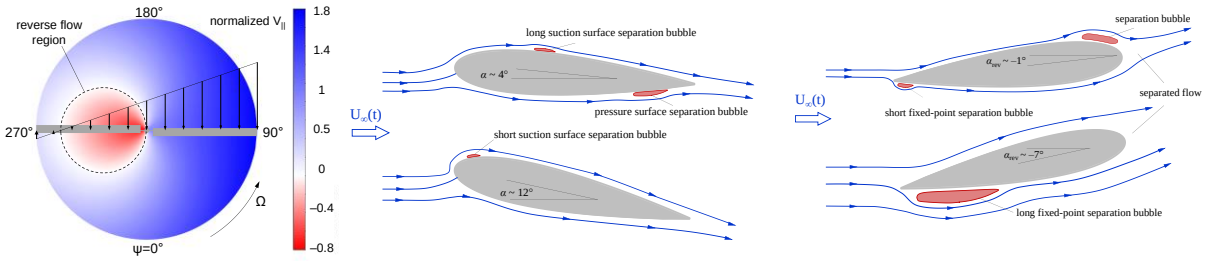

Figure 2. Left: Normalized velocity $V_{\|}/\bar{V}$ distribution within the rotor of a high-speed coaxial helicopter at $\mu = 0.77$ (adapted from [39]). Middle: Separation bubbles on a forward-flow symmetric airfoil (adapted from [49,50]). Right: Separation bubbles on a reverse-flow symmetric airfoil (adapted from [39]).

2.2 Wind Turbine Blades

While much of the early dynamic stall research was aimed at helicopter applications, dynamic stall has been identified as a major factor affecting the wind turbine blade aerodynamics. Of the two most well-known lift-based wind turbine configurations—namely, HAWTs and VAWTs—dynamic stall manifests in different ways. On HAWTs, it is observed when the wind direction is not perpendicular to the rotor disk, i.e., in yawed flows [52-54]. The simultaneous loss of lift and increase in drag reduces the rotor torque, and the resultant unsteady aerodynamic loads cause fatigue loading of the blades, yawing mechanism and the drive train. These effects can be exacerbated by atmospheric turbulence, wind shear, and tower shadow [54]. More recently, dynamic stall has been identified as a major factor on the blades of floating horizontal axis wind turbines (FHAWTs), due to the pitching motions of the floating platform in the direction normal to the disk plane [55]. The combination of large floater oscillation frequencies and amplitudes, coupled with blade height above the axis of rotation can result in post-stall angles-of-attack and, therefore, dynamic stall [56,57].

Two examples illustrating the root causes of HAWT dynamic stall are shown for arbitrary HAWT blade sections subjected to wind gusts, e.g., due to pitching motions of FHAWTs (in Figure 3, left), and under yawed inflow relative to the turbine disk in (Figure 3, right). While both scenarios produce angle-of-attack oscillations, gusts are generally in-phase with the angle-of-attack increases and yawed flows are generally in anti-phase. This is an important distinction because the relative dynamic pressure sets limit on flow dynamic stall control authority. Irrespective, a major objective is to decrease the flapping mode loads on the

blade, typically represented by normal or lift force oscillations. While the majority of methods propose some type of mechanical flap or blade morphing, we will show that dynamic stall control can be considered as a viable alternative.

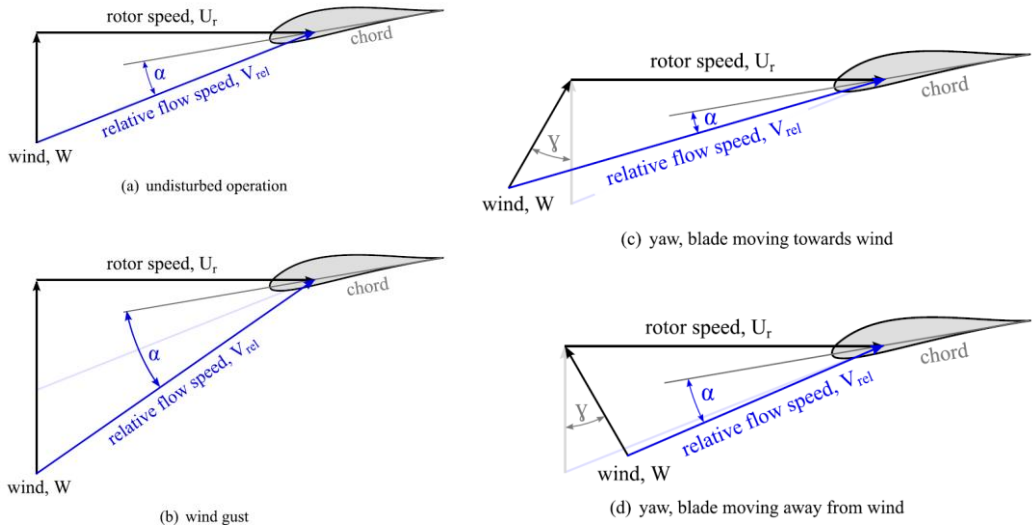

Figure 3. Schematic representations of a wind turbine blade section, subjected to: a wind gust, e.g. due to pitching motions of FHAWTs (left); and yawed inflow relative to the turbine disk (right).

The development of VAWTs—in particular low solidity Darrieus turbines—was motivated by the possibility of ground-based drive trains and insensitivity to wind direction [58]. However, these are inherently unsteady flow machines, because their blades experience periodic oscillation variations of the relative velocity vector (direction and amplitude), leading to large oscillatory loads. The problem is exacerbated at high wind speeds where turbines operate at low tip speed ratios and are therefore prone to dynamic stall [59]. It has long been recognized that dynamic stall increases peak torque on low-solidity Darrieus turbines [60,61], and neglecting dynamic stall effects results in an underprediction of peak power. The resultant large oscillatory loads can accelerate blade failure and may also damage the gearbox, bearings and other components of the drive-train. Recent decades have witnessed a renewed interest in the H-rotor concepts; both for potential offshore floating-platform installations and small wind turbine (<100 kW) applications.

Small high-solidity straight-bladed VAWTs—due to their low tip-speed ratios— are unusual in the sense that at peak power their blades are stalled for a large fraction of the azimuth. Blade aerodynamics depends strongly on the blade-radius ratio $\varepsilon \equiv c/R$. In particular, during the pitch-up motion, both the "virtual camber" $(z'/c)_{\max}$ and the dimensionless pitchrate

$\kappa_{up} \equiv \dot{\alpha} c / 2|V_{rel}|$ are proportional to ε [24,62]. Figure 4, based on idealized kinematics, illustrates the difference between the virtual camber, relative dynamic pressure, angle-of-attack, and pitch-rate for two turbines of identical solidity, namely $N = 2$, $\varepsilon = 0.75$ and $N = 5$, $\varepsilon = 0.3$. The blade static angle is assumed to be $\alpha_s = 13°$, and the shaded area on the graphs represents post-static-stall angles-of-attack, which makes up the majority of the upstream torque producing azimuth. Both the virtual camber and dimensionless pitchrates increase by a factor of 2.5. With the blades stalled dynamically over the majority of the azimuth, we can define two objectives. First, dynamic stall can be "managed" by blade design, i.e., the selection of ε and x_c / c to maximize performance and with acceptable unsteady loads [63,64]; and second, attempts can be made to suppress or eliminate dynamic stall.

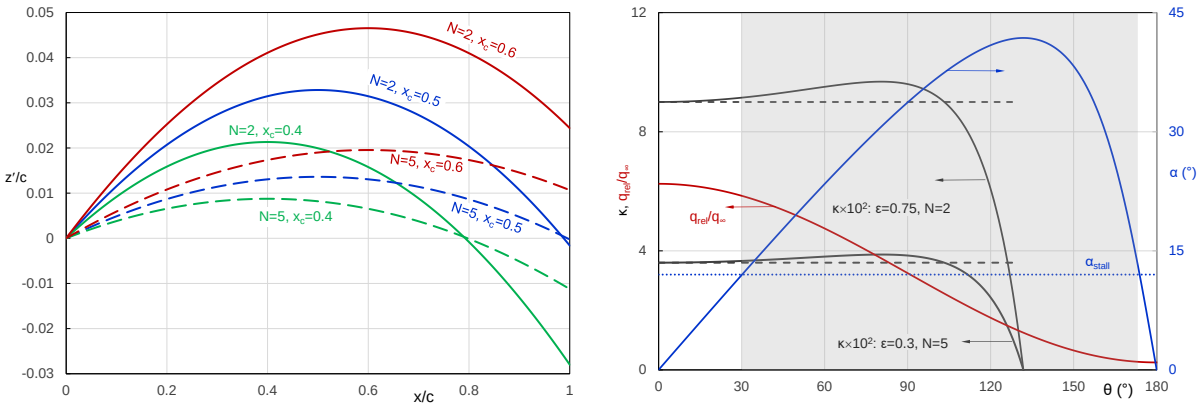

Figure 4. Virtual camberlines at different strut-blade connection points x_c / c (left), and angle-of-attack, pitch-rate and relative dynamic pressure (right) in the upwind quadrants of equal-solidity VAWTs ($N = 2$, $\varepsilon = 0.75$ and $N = 5$, $\varepsilon = 0.3$) operating at the Betz limit. Static stall is assumed to occur at 13° and the shaded area represents post-stall angles-of-attack [24,62].

2.3 Fixed Wing Aircraft

We can distinguish between cyclical phenomena—associated with helicopter and wind turbine blades and characterized by alternating dynamic stall and attachment—and transient phenomena produced by purely pitch-up or pitch-down motion. In transient dynamic stall, the external flowfield changes dynamically from one nominally steady state to another, often characterized by delay-and-decay-type behavior [65]. One example is the attainment of so-called supermaneuverable aircraft that exploit the transient effects of the lift overshoot associated with dynamic stall [66]. Here the objective is to exploit and harness dynamic stall effects, to facilitate controlled flight and stability at excessively high angles-of-attack.

Alternatively, a control objective may be the delay unsteady vortex breakdown—which can lead to large pitch oscillations or loss of control, or excessive structural loads—by means of external actuation.

Dynamic stall has also been identified as a factor leading to loss of control on small and medium-scale fixed-wing unmanned aerial vehicles (sUAVs and UAVs) that fly at relatively low altitudes. In these highly unsteady environments, dynamic stall is most acute when the gust characteristic velocity and/or length scales are comparable to those of the vehicle [67]. This can occur, for example, when a vortex encounters a wing, where the vortex peak velocity and core size are comparable [2]. On larger UAVs dynamic stall from control surfaces due to crosswind gusts during takeoff and landing can lead to a loss of control [12].

2.4 Flapping Wing Aircraft

For flapping wing aircraft, dynamic stall is a major factor for both hover and propulsion [68,15]. This class of aircraft is known as flapping wing unmanned air vehicles (FWAVs) [69] and spans mostly the micro to nano air vehicles (MAV and NAV) ranges [70]. For propulsive flight, typically at $Re < 10^5$, dynamic stall is associated with reduced thrust coefficients and reduced propulsive efficiency [13]. The objective therefore is to suppress or eliminate it, either by design or by passive or active methods. For hovering flight, commonly at $Re < 10^4$, massively separated unsteady flows are in fact exploited to generate lift [71,72]. Researchers turn to, *inter alia*, the field of biomimicry—in particular, insect and bird flight—to develop vehicles with these specifications. Aerodynamic factors that must be considered are low Reynolds numbers, low aspect ratios, and possibly, flexible, wings [72]. A major challenge is to develop flapping kinematics, together with wing shape and flexibility, to take full advantage of the lift-generating large-scale unsteady vortical flow structures. In this context, the objective is not to eliminate or ameliorate separation, but rather to manage or control the unsteady separated vortical structures.

An example of the role of the LEV, combined with the wingtip vortex (TV), is shown in Figure 3, which is a numerical simulation of hovering bumblebee, where the wings simultaneously flap and pitch [73]. The combination of the Q-criterion isosurface on the left wing and the pressure coefficient on the right wing, illustrates dominant instantaneous effect of the LEV. Wing flapping frequencies must correspond to time-scales that ensure at least one vortex above the wing at any instant, in order to extract beneficial aerodynamic forces. When viewed as a problem of dynamic stall control, the wing itself serves as the actuator, and in this sense, it can be considered to be a mechanical actuator. In this review, we will consider a significant simplification of the problem and attempt to explain leading aerodynamic

parameters in terms of vortex shedding frequencies and leading-edge active flow control perturbations.

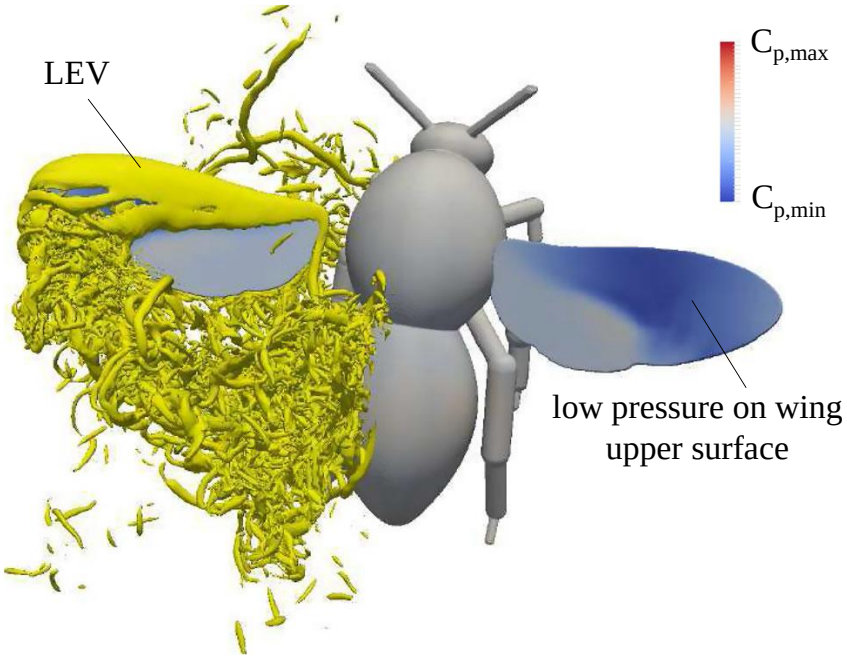

Figure 5. Results from a numerical simulation of a hovering bumblebee, with flapping and revolving wings, illustrating the effect of the LEV by the Q-criterion isosurface (left wing) and the pressure coefficient (right wing) (from [73]). Republished with permission.

3 Incompressible Flows

The vast majority of dynamic stall research has been performed in the incompressible flow regime, due to its appearance on helicopters and wind turbine blades, as well as fixed- and flapping-wing vehicles (see section 1) [1,2]. We will adopt the conventionally incompressible demarcation, namely $M < 0.3$, although at combined large pitchrates and high post-stall angles-of-attack, flow can become locally supercritical $M \approx 0.2$ [20]. The process of dynamic stall is not currently amenable to first principles theoretical analysis, and hence our empirical or semi-empirical understanding generally guides our control attempts. For incompressible flows, a common theme is that methods that are effective for static stall control are effective for dynamic stall control, once the appropriate dynamic effects are accounted for. In the subsections below, we will differentiate between different dynamic stall, review passive and active methods, justify reductions in parameter space, and survey different approaches to control. Compressible dynamic stall and its control are discussed in section 4.

3.1 Characterization of Dynamic Stall

Although dynamic stall generally occurs under combined pitching, plunging and surging, it is common to consider pure harmonic pitching, of the form:

$$\alpha(t) = \alpha_m + \alpha_1 \sin(\omega t) \tag{1}$$

under a constant freestream velocity U_∞. Justifications for, and limitations of, the idealized blade motion of equation (1) are discussed in section 3.6. In addition to the angle-of-attack parameters given in equation (1), the leading dimensionless parameters are reduced pitchrate $k \equiv \omega c / 2U_\infty$ and chord-based Reynolds number $Re \equiv U_\infty c / \nu$. (Mach number effects are discussed in section 4.) On finite wings, it is more common to consider a transient motion from one angle-of-attack to another, characterized by the dimensionless pitchrate $\kappa \equiv \dot{\alpha} c / 2U_\infty$.

3.1.1 Two-Dimensional Airfoils

Much like static stall studies, our main understanding of dynamic stall derives from the two-dimensional investigations. Similarly, under dynamic pitching, three main types of incompressible dynamic stall are generally identified, namely leading-edge, trailing-edge, and thin airfoil, stall. Representative examples of the principal aerodynamic coefficients C_n and C_m are shown in Figure 6 for a NACA 0012 airfoil (top row) and NACA 0018 airfoil (bottom row), where the pitch axis is the aerodynamic center $c/4$. A representative example of thin airfoil stall under pitch-up is shown in Figure 7.

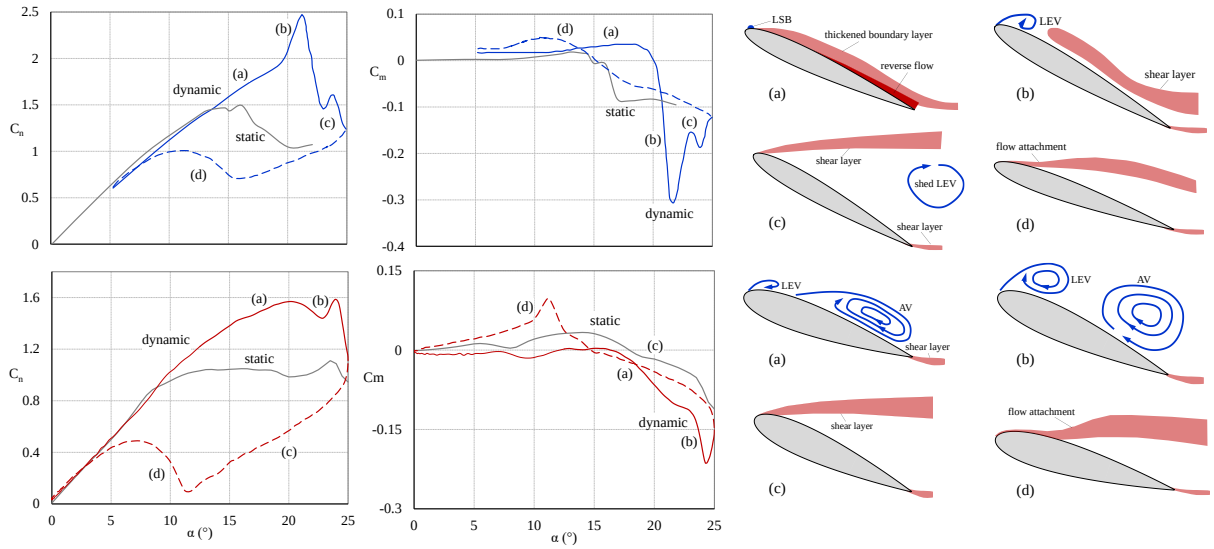

Figure 6. Aerodynamic coefficients and illustrations of leading-edge (NACA 0012 airfoil, $Re = 2.5\times10^6$, $k = 0.050$) [17,74,75] and trailing-edge (NACA 0018, $Re = 5\times10^5$, $k = 0.058$) [80,81] dynamic stall, under harmonic pitching about the aerodynamic center $c/4$.

3.1.1.1 Leading-Edge Stall

Leading-edge stall, often associated with helicopter blades, is the most widely studied and its characteristics can be understood with respect to the descriptions in [17,74,75] amongst others. Note that the reduced frequency is an idealization because, for a given radius, the velocity relative retreating blade varies with the azimuth. Typical helicopter blade values lie in the range $0.02 \le k \le 0.25$, with corresponding Reynolds numbers $2\times10^6 \le Re \le 6\times10^6$. The various stages described in [17] are condensed in Figure 6 (top row). During pitch-up, as the airfoil exceeds the static stall angle, flow reversal appears on the aft part of the airfoil and moves upstream with increasing α. Nevertheless, the streamlines do not deviate significantly from the airfoil surface, and the leading-edge bubble does not immediately burst. Thus, lift and moment stall are delayed, as exemplified by negligible changes to the lift and moment slopes $\partial C_l / \partial \alpha$ and $\partial C_m / \partial \alpha$. At an angle determined by k, $\alpha_{\max}$, and Re, the leading-edge bubble bursts [75]; this is often described as the formation and growth of a leading-edge vortex (LEV), which is identified by moment stall and an increase in the lift slope. Shedding of LEV precipitates lift stall and the shed vortex induces an upwash, identified as a second smaller lift peak, without significantly affecting the moment. The flow remains separated until the airfoil has pitched to below the static stall angle, and the cycle is completed when the boundary layer attaches to the surface.

The attachment process initiates at the leading-edge just below the static stall angle [76,77]. This is followed by a "pressure wave" that propagates from the leading-edge to the trailing-edge [78]—and is associated with the initial attachment of the shear layer, which is independent of airfoil shape [78], and driven by the freestream velocity [79]. The time taken for full attachment of the boundary layer depends upon pitchrate but saturates at approximately four convective time units.

There are several analytical and semi-analytical explanations for the stall delay: e.g., pressure gradient effects, effective camber, and the Magnus effect; and the formation and shedding of the LEV based on a Lagrangian analysis of the flow [20]. However, from a control authority viewpoint, it is pragmatic to consider static and dynamic stall as similar process, with the appropriate delays and decays accounted for. This viewpoint is based on static NACA 0012 airfoil's unsteady surface pressures at $\alpha_s + 1°$, where the flow separates dynamically, via the mechanism of bubble bursting, and attaches dynamically—both seemingly randomly. While it is not clear what triggers this behavior, the qualitative dynamic separation and attachment on the static airfoil are identical to those on the pitching airfoil. This observation serves as a basis for the assertion that effective static stall control strategies will also be effective under dynamic conditions.

3.1.1.2 Trailing-Edge Stall

Trailing-edge stall—describe here with respect to the NACA 0018 airfoil—has some important differences that are shown in Figure 6 (bottom row), and it is most commonly associated with wind turbine blades. On large HAWTs, typical reduced frequency and Reynolds number ranges are $0.02 \le k \le 0.1$ and $6\times10^6 \le Re \le 10^7$. (On high-solidity VAWTs, the dimensionless pitchrate pitch-rate κ_{up}, see section 2.2, is a more appropriate parameter and $10^5 \le Re \le 10^6$). As the airfoil pitches beyond the static stall angle, the trailing-edge separation present in the static case develops into an aft vortex (AV) that results gentle lift-stall, accompanied by gradual nose-down pitching moments [80,81]. In this particular case, the large leading-edge radius, combined with shedding of the AV results in weak leading-edge vortex LEV and hence no significant upwash in the wake. As in the leading-edge stall scenario, the flow attaches from the leading-edge and can also be viewed as delay-and-decay-type behavior, based on the observations and modeling of flow attachment under static versus dynamic conditions [82].

3.1.1.3 Thin Airfoil Stall

Thin airfoil stall is commonly studied with regard to pure pitch-up motions, as shown in Figure 7 [83,84]. Corresponding finite wing results, with $AR_R = 3.94$, are also shown for purposes of comparison. These studies are usually motivated by applications to rapidly pitching aircraft and flapping wing flyers, where large momentary lift is required, or where sustained flight requires that unsteady lift forces exceed corresponding steady values by several factors. The leading-edge bubble, which exists under static conditions, manifests as an LEV, whose size and strength increase with increasing pitchrate. This leads to lift coefficients that are several factors greater than the corresponding static values. Increasing pitchrate also affects the formations and shedding of the vortex, as can be seen by the $C_{m,c/2}$ peak. Furthermore, the vortex strength, and hence lift, increases with the distance from the pitch axis to $3c/4$. Thus, apart from non-circulatory components [85], the primary contribution to lift arises from the LEV as shown schematically in Figure 7. It is important to note that at sufficiently high Reynolds numbers, where skin friction plays a relatively minor role, both lift and drag are primarily dependent on the normal force, hence $C_d / C_l \approx \tan\alpha$.

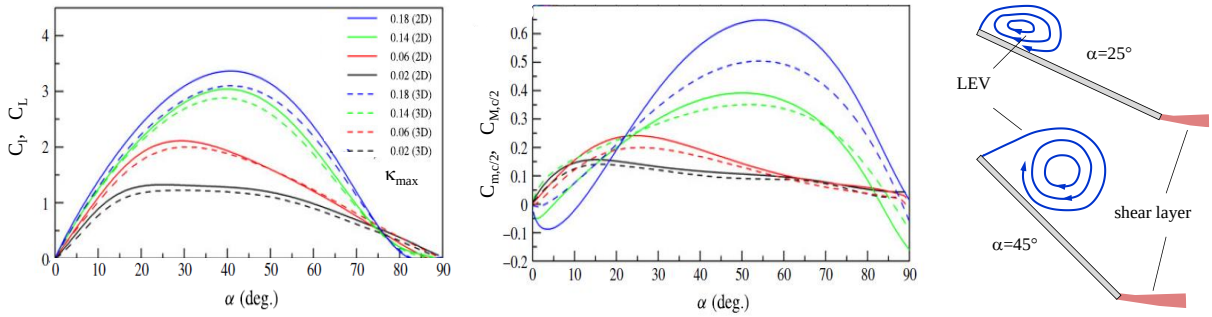

Figure 7. Aerodynamic coefficients [84] and illustrations (cf. [83]) of thin airfoil dynamic stall based on the pitch-up motion. Coefficients are for $\alpha \approx 45°(1-\cos\omega t)$, with $\kappa_{\max} \equiv \dot{\alpha}_{\max} c / 2U_\infty$ at $Re = 1.45\times10^4$ and the pitch axis at $c/2$. (For the 3D case $AR_R = 3.94$). Data reproduced with permission.

3.1.2 Finite Wings

On finite wings, dynamic stall, like its static counterpart, is strongly affected by three-dimensional and tip effects. For example, on an $AR_R = 2$, NACA 0012 profile with $k = \pi/16$ during pitch-up an LEV forms, while the tip vortices (TVs) maintain vortex lift at the leading-edge of the tips [86]. The combined LEV and TVs evolves into an arch and is finally shed as a ring vortex. The integrated loads, therefore, do not exhibit significant $\partial C_l / \partial\alpha$ changes during

pitch-up, as observed on airfoils [86,87,88]. A representative example is shown for an $AR = 1$ wing, under both light and deep stall in Figure 8 (left) [87]. There is also evidence to suggest that flow topologies associated with different planform shapes, for example, rectangular shapes with flat and rounded tips, tapered wingtips, and swept-back tips, exhibit strong similarities [89]. With the introduction of sweep [88], the arch vortices formed on each semi-span, move successively outboard with increasing sweep angle.

On delta wings, static lift is produced predominantly by the swept leading-edge vortices, sLEVs [90]. (We used this terminology to distinguish it from conventional swept-wing airfoil LEVs.) Under dynamic pitching, the presence of lift generating sLEVs that already exists, results mainly in delay-and-decay type aerodynamic behavior [91-97]. Consequently, the lift overshoot does not exhibit strongly non-linear slope change, because no new vortical structures are present. During pitch-up motion, vortex breakdown lags its steady state counterpart, leading to the lift overshoot. Vortex breakdown continues moving forward, and when it reaches the wing apex the flow is considered to be fully separated. During pitch-down, there is again a delay in the re-formation of the leading-edge vortices, and vortex breakdown is overcome from the apex to the trailing-edge. An example of a fighter aircraft model under free pitching, shown in Figure 8, is typical of the behavior observed on delta wings [65].

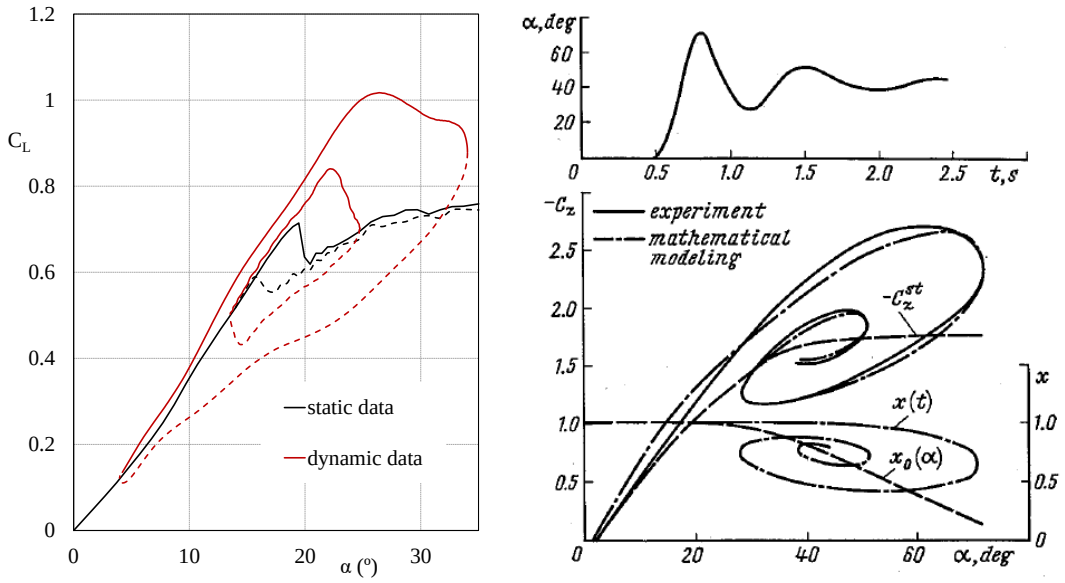

Figure 8. Left: Lift coefficient on a finite wing ($AR = 1$) undergoing harmonic pitching at $k = 0.03$ and $Re = 3.0 \times 10^5$ [87]. Right: Vertical lift coefficient on a fighter aircraft model under free pitching [65]. Permission to reprint image pending.

3.2 Common Control Metrics

The particular metric used to gauge the efficacy of dynamic stall control, depends upon the specific application. For example, on wind turbine blades, normal or lift force coefficient excursions, e.g., $C_{n,\mathrm{exc}} \equiv C_{n,\max} - C_{n,\min}$ must be constrained to bounds dictated by flapwise fatigue lift considerations [98]. On helicopter blades, higher $C_{l,\max}$ is desirable, but this must not come at the expense of negative pitching moment or moment excursions, $C_{m,\min}$ or $C_{m,\mathrm{exc}} \equiv C_{m,\max} - C_{m,\min}$, followed by lift stall. It was shown by [99] that for a given airfoil, a unique relationship exists between maximum lift, minimum moment and maximum form drag, expressed by so-called dynamic stall functions $C_{l,\max} = f(C_{m,\min})$ and $C_{l,\max} = f(C_{d,\max})$. These functions are useful because they allow an unambiguous evaluation of a control method, or a comparison between different methods. A different metric proposes increasing or maintaining $C_{l,\max}$ while containing $C_{m,\mathrm{exc}}$ to within an allowable bracket $\varepsilon C_{m,\mathrm{exc}}$, where ε is a factor slightly greater than 1.0 [100]. The bracket is subjective and is typically prescribed by practical design considerations.

On helicopter blades, dynamic stall can lead to torsional stall flutter, that occurs when the nonlinear unsteady aerodynamic loads couple with the torsional natural frequency of the blade to produce a self-sustaining oscillation [20]. This aeroelastic instability is distinct from classical flutter that occurs under pre-stall conditions. When advancing blade damping is small, negatively damped retreating blade stall can lead to "additive limit-cycle growth" [20]. For a single-degree-of-freedom airfoil within a constant freestream, the cycle-averaged aerodynamic damping is:

$$\Xi_{\mathrm{cycle}} \equiv -\frac{1}{\pi\alpha_1^2}\oint C_m \, d\alpha \tag{2}$$

and, more recently, techniques have been developed to calculate the intracycle aerodynamic damping [101]. It was shown that unstable loading is mostly prevalent in light stall, where the sense of the C_m-α loops are positive. Effective dynamic stall devices or methods should reduce, eliminate, or invert the clockwise C_m-α loops associated with dynamic stall.

3.3 Management of Dynamic Stall

In certain applications, the presence of dynamic stall is desirable because it produces a temporal lift increase that can be exploited. In these instances, dynamic stall must be "managed" in the sense that the convective times-scales governing the dynamic stall processed must be harnessed

to produce an aerodynamic benefit. We demonstrate this on high-solidity VAWT ($\sigma \equiv Nc/R > 0.5$, where N is the number of blades, c is the blade chord-length and R is the turbine radius), typically used for high-torque applications [102-105], where dynamic stall is not a bug—it's a feature, due to high angles-of-attack attained at low tip-speed ratios $\lambda \approx 1$ [24]. Dynamic stall, therefore, must be managed to increase torque without exceeding design fatigue loads.

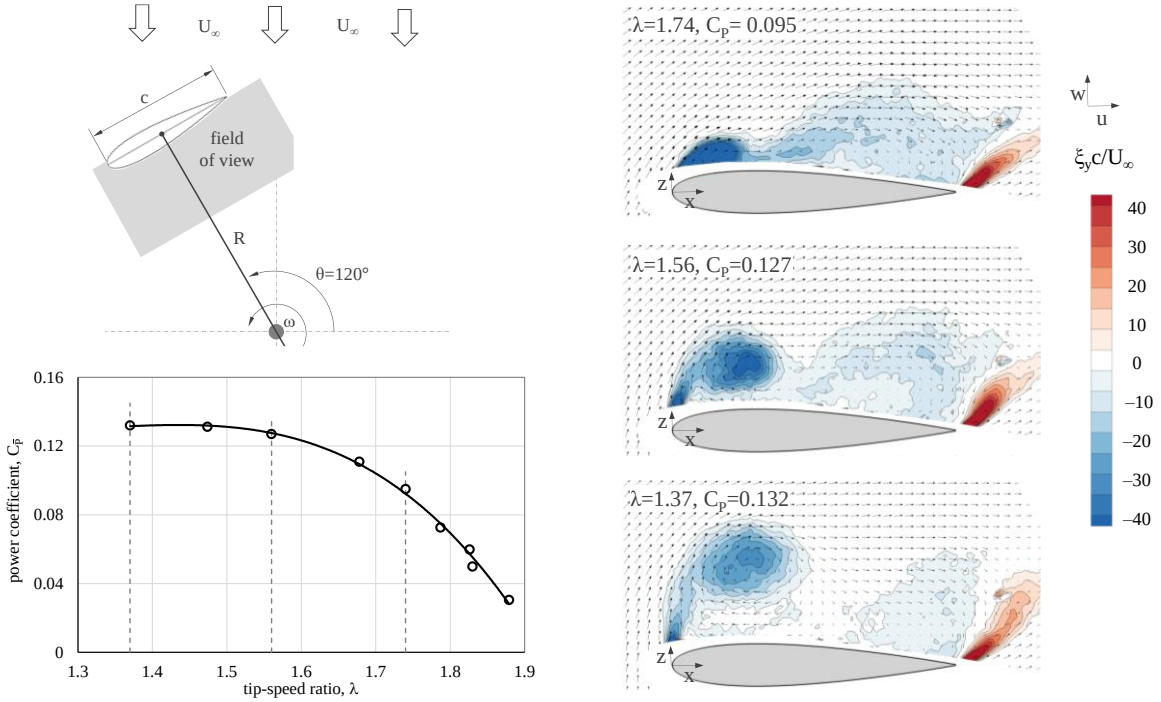

Figure 9. Left, top: VAWT blade schematic showing the particle image velocimetry (PIV) field of view. Left, bottom: Turbine performance map, showing tip-speed ratios corresponding to PIV measurements. Right: Velocity vectors relative to the blade and vorticity inboard of the upstream blade (adapted from [106]).

Solidity can be varied by either increasing N or the chord-radius ratio $\varepsilon \equiv c/R$, and this is an important distinction (see Figure 4), because both the dimensionless pitchrate $\kappa \equiv \dot{\alpha} c / V_{\text{rel}}$ and the virtual camber dz'/dx—in the upwind, torque-producing quadrants—are proportional to ε [24,62]. Figure 9 shows power coefficient data with flowfield images at $\theta = 120°$ inboard of the upstream blade of a two-bladed H-rotor VAWT model with $\varepsilon = 0.6$ (adapted from [106,63,24]). The velocity vectors (u, v) are rendered in the coordinates of a stationary blade; and dimensionless vorticity was calculated according to $\zeta_z c/U_\infty \equiv (\partial v/\partial x - \partial u/\partial y) c/U_\infty$. Increasing the turbine loading reduces λ and produces more advanced shedding of the LEV with a successively smaller AV—and further increases in

loading arrests the turbine. During pitch-up, both the LEV and AV are responsible for torque generation. The aerodynamic objective, therefore, is to maximize torque generation associated with the dynamic stall vortices when the relative dynamic pressure is high and to allow their shedding when the relative dynamic pressure is relatively low. In this way, the beneficial effects of dynamic stall on the aerodynamic coefficients can be harnessed and the detrimental effects can be ameliorated.

3.4 Passive Devices: Fixed and Deployable

The most common passive devices evaluated under conditions of dynamic stall are vortex generators (VGs) or some variation on VGs, leading-edge devices, backflow flaps, and trailing-edge flaps to Gurney-type flaps. VGs and micro VGs (10%-50% of the boundary layer thickness [107]) are the most widely used passive devices on wind turbine blades, particularly on the thick inboard sections [108,109], and they are often retrofitted to overcome poor aerodynamics due to leading-edge degradation [110]. In particular, the inboard blade sections are susceptible to dynamic stall because gust amplitudes may be comparable in magnitude to the local blade speed. Under static conditions, VGs generally increase $C_{l,\max}$, α_s and $C_{m,\min}$, but also increase base-drag C_{d0} [111]; and therefore similar observations are made under dynamic pitching [112,113]. The major design parameters for optimization of turbine power include profile shape, height-to-boundary layer ratio, chordwise location, number of arrays and layout [108]. The negative effects on drag have led to the concept of "on-demand" deployable VGs [114,115] or rotatable VGs using servo motors [116] that are deployed only when needed, i.e., for $\alpha \geq \alpha_s$, and have been demonstrated under conditions of scheduled or pre-determined control [117].

Leading-edge devices commonly employed on aircraft to increase the stall angle under nominally static conditions have also been applied to the control of dynamic stall. These include leading-edge slats (Handley-Page slots) [118,119] drooped (or deformable) leading-edges [120], and variable/adaptive geometry or camber. Downstream of the leading-edge, backflow (reduction) flaps [121,122]—that have a similar appearance to small spoiler elements—produce an increase in $C_{l,\max}$ by hindering movement of the separation location upstream. Extending this passive concept to deep dynamic stall conditions on an OA209 airfoil, produced a 19% increase in $C_{m,\min}$ that could be increased to 25% by actively deploying the flap [123]. Trailing-edge flaps and trailing-edge devices, such as Gurney flaps or micro-tabs, do not directly control dynamic stall. Rather, they modify aerodynamic performance at pre-stall angles-of-attack. For

example, upward flap deflections increase $C_{m,\min}$, but also reduce $C_{l,\max}$ and the formation and evolution of the LEV is not materially affected [124]. Under static conditions, Gurney flaps increase the lower surface pressure and suppress or eliminate upper surface trailing edge separation [125]. Hence, under dynamic conditions, lift is enhanced, but dynamic stall mechanism not significantly affected [126].

3.5 Active Flow Control

While passive devices are often reflexively chosen due to their simplicity, their control authority is limited and this has led to the evaluation of active flow control (AFC), which we define as devices or methods that are driven by an external energy source. (For purposes of this discussion, this does not include the energy required to deploy passive devices as described in section 3.4.) Typical examples include slot suction [127,128], slot blowing [129-132], combinations of the two [133], combustion-based actuators [134], microjet blowing [135], steady and pulsed VG jets [136,137], zero mass-flux blowing [100,138] and various types of plasma actuation [139,140]. Active methods are either nominally steady or unsteady. Unsteady methods are most commonly divided into those whose input timescales are much smaller than [141,100,140], and comparable to [27,21], those of dynamic stall. We will refer to these as high-frequency and low-frequency perturbations, respectively. Note that for scheduled or feedback control, perturbations at both timescales is common (see sections 3.7 and 3.9).

3.5.1 Nominally Steady Methods

The main nominally steady methods involve some form of mass extraction (suction) or momentum addition (blowing). As a general rule, methods involving suction (e.g. [127]) are at a disadvantage because the pressure difference is limited to one local atmosphere and suction holes and slots are prone to blockage [128]. On the other hand, the introduction of steady momentum flux is usually only limited by sonic conditions at the slot or orifice throat. Two methods that show promise are upper-surface discrete jet blowing, that mimics the effect of VGs [142], and slot blowing, which exploits the Coandă effect [129]. The latter is technologically the most successful, having been applied to several production aircraft (see references in [143]), and will be the focus of this section. The leading parameter for slot blowing is the momentum coefficient, namely:

$$C_\mu \equiv \frac{\rho_j U_j^2 A_j}{q_\infty A_{\text{ref}}} \tag{3}$$

where $A_j = h_j$ ($A_j = h_j$ and $A_{\text{ref}} = c$ for two-dimensional problems). Power consumed by the actuator can either be calculated directly using a power coefficient [144] or indirectly based on the selected configuration [145,146]. The first effective demonstrations of active retreating-blade stall, under incompressible conditions ($M < 0.2$), were the rotor-rig experiments performed by [129] in the range in the range $0.34 \le \mu \le 0.46$. The primary observations were that surface-tangential leading-edge slot ($x_s / c = 8.5\%$) blowing is effective in reducing moment stall, mid-chord ($x_s / c = 50\%$) blowing is ineffective, and cyclic (or scheduled) control can be implemented for energetic input savings. These observations have been confirmed and further understood in subsequent dynamic stall airfoil experiments [130,132]. Leading-edge blowing "traps" the separation bubble upstream of the slot [130-138]. If the slot is too far downstream (e.g. $x_s / c = 25\%$) [130,], then excessive momentum input ($C_\mu > 0.16$) is required for effective control. If the slot is even further downstream (e.g. $x_s / c = 50\%$) [129,132], then the LEV is unaffected, but trailing separation can be eliminated. Furthermore, similar leading-edge slots have greater control-authority on relatively thick airfoils (e.g., NACA 0018 [132] versus NACA 0012 [138]).

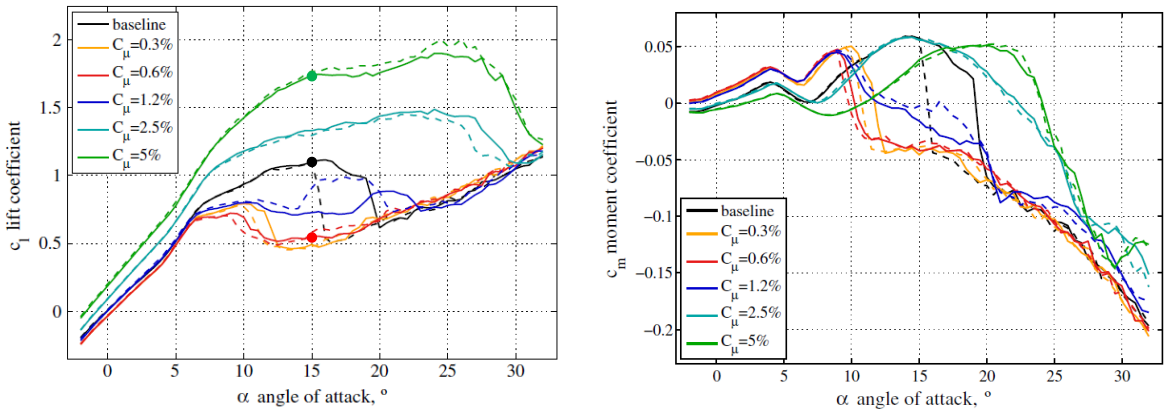

Figure 10. Quasi-steady NACA 0018 aerodynamic coefficients for the baseline and for leading-edge ($x_s / c = 5\%$) slot blowing at different momentum coefficients, at $Re = 3.0 \times 10^5$. Points indicated correspond to PIV data in Figure 11.

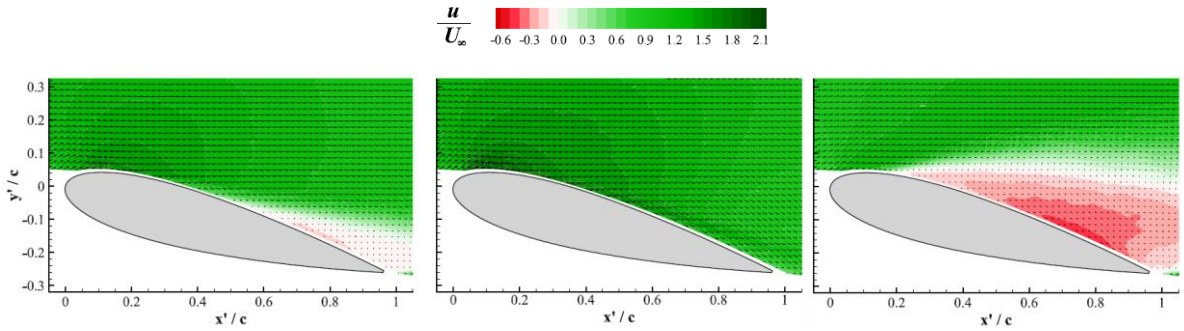

Figure 11. Leading-edge slot blowing flowfields for baseline (left), high-$C_\mu = 5\%$ (center) and low-$C_\mu = 0.6\%$ (right) momentum coefficients, at $\alpha = 15°$ (corresponding to points indicated in Figure 10).

Slot blowing has another underexploited feature, which is that low momentum coefficients corresponding to $U_j \lesssim U_e$ (U_e is the boundary layer edge velocity at the slot location), induce (or promote) separation [132,147,148,5]. In the absence of blowing, the baseline separation bubble is held in place by a balance of pressure and shear forces, and this balance is disturbed by the low momentum flux [132], leading to bursting of the bubble. Therefore, slot blowing can be used as a load control device by either inducing or suppressing dynamic stall. The breakeven point typically corresponds to $C_\mu(1-U_e/U_j) \approx 1$ [147].

Dynamic stall and its control are directly related to static stall and its control under the same control input conditions. This is shown by the dual effect—either stall suppression or promotion—for quasi-steady and unsteady pitching, shown in Figure 10 and Figure 11, and Figure 12 and Figure 13, respectively [132]. For the quasi-steady baseline case, trailing-edge stall commences at $\alpha \approx 7°$ (Figure 10, left), with leading-edge stall at $\alpha \approx 16°$ and significant bi-stable behavior (hysteresis). Trailing-edge stall reduces the overall circulation—and hence the leading-edge suction peak—resulting in an increase in C_m at $\alpha > 7°$, and the extent of trailing-edge separation can be seen in Figure 11 (left). Blowing with $C_\mu \geq 2.5\%$ increases circulation at $\alpha \leq 7°$, reduces or eliminates trailing-edge separation at $\alpha > 7°$ (see Figure 10, left; and Figure 11, center), and significantly increases the leading-edge stall angle (up to $\approx \alpha_s + 12°$). The pressure coefficient distributions (not shown, see [132]), indicates that leading-edge separation is prevented by trapping the bubble upstream of the slot. In addition, the aft constant pressure (separated flow) region propagates gradually towards the leading edge with

angle-of-attack, and virtually eliminates bi-stable lift behavior. With $C_\mu \le 0.6\%$, leading-edge stall is precipitated at $\alpha \approx 9°$ (Figure 11, right), and also reduces bi-stable behavior.

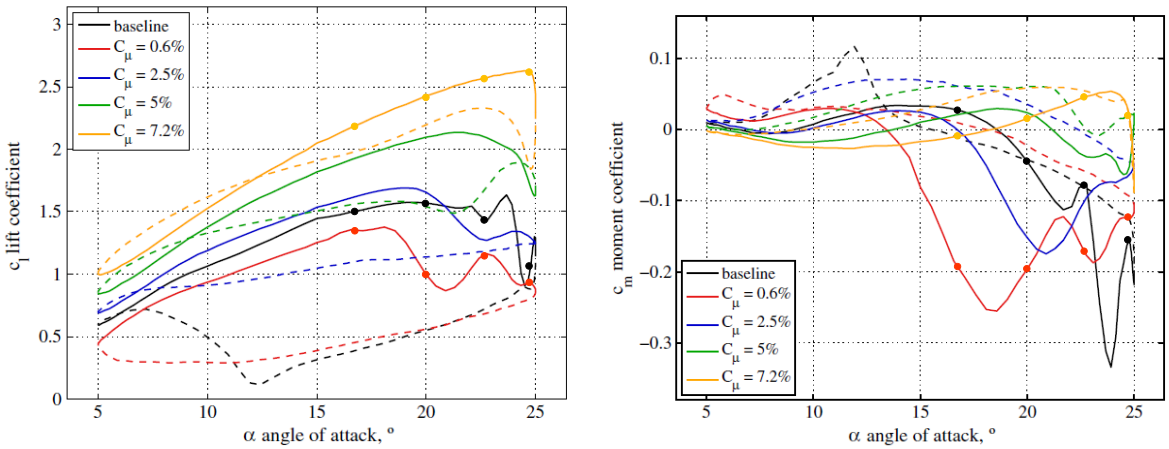

Figure 12. Baseline and slot blowing airfoil lift and moment coefficients under dynamic pitching for $\alpha = 15° + 10° \sin \omega t$ at $k = 0.074$ and $Re = 2.5 \times 10^5$. Indicated points identify data sets shown in Figure 13.

Corresponding unsteady phase-averaged aerodynamic coefficient data at different C_μ are shown in Figure 12 and selected representative combined pressure coefficient, vorticity and vector renderings are shown in Figure 13, during the pitch-up stroke (see indicators on Figure 12). For the baseline case, trailing-edge separation is clearly evident at $\alpha = 16.7°$ and an aft dynamic vortex (AV) forms at $\alpha = 20°$ to produce a mild lift peak, together with the onset of gentle moment stall. The formation and shedding of the LEV $(\alpha > 22.7°)$ produces a second peak, which sheds into the wake, and its resulting upwash produces a third peak. Low momentum blowing $(C_\mu = 0.6\%)$, precipitates leading-edge separation which reduces lift and triggers moment stall $(\alpha = 16.7°)$, with full leading-edge stall at $\alpha \approx 21°$. The small second lift peak at $\alpha \approx 22.7°$ is a result of upwash in the wake, as in the baseline case. For high momentum blowing $(C_\mu = 7.2\%)$, the bubble is trapped upstream of the slot and this effectively eliminates leading-edge dynamic stall for $\alpha < 24.5°$. Close to the peak angle-of-attack, the leading-edge suction peak drops but full leading-edge stall and hence moment stall are not fully eliminated. There is also no secondary peak here, because there is no shedding of an LEV. Irrespective of C_μ value, $C_{m,\min}$ always increases (or $C_{m,\text{exc}}$ reduces) and positive cycle-averaged damping Ξ_{cycle} always increases. The large control authority of leading-edge slot blowing is exploited

further for iterative learning and feedforward control, illustrated in sections 3.8 and 3.9.2, respectively.

The pressure, integrated load and PIV data, described above, can be found with full documentation at the data resource: https://www.flowcontrollab.com/data-resource. These data sets can be used for CFD validation, and are employed for iterative learning control described in section 3.8 and feedforward control described in section 3.9.2.

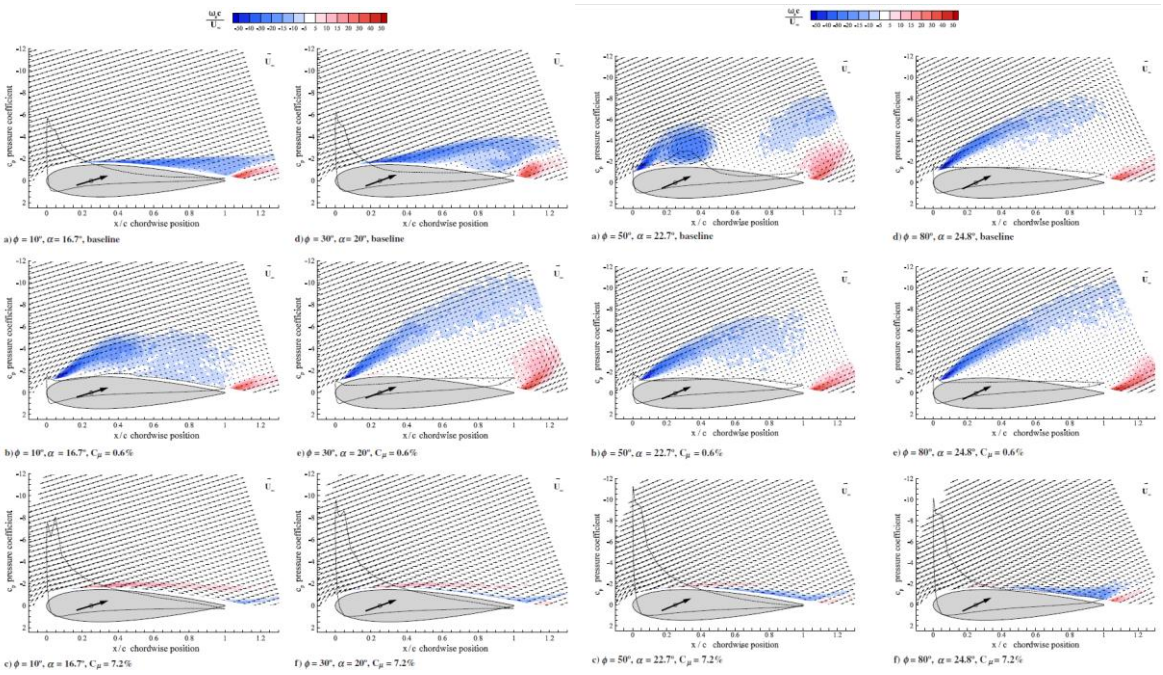

Figure 13. Superimposed phase-averaged pressure coefficients, vorticity and flow vectors for selected pitch-up angles corresponding to baseline, low momentum coefficient and high momentum coefficient cases, shown in Figure 12.

3.5.2 Periodic Excitation and Forcing

The introduction of high-frequency periodic perturbations—mechanical, fluidic, combustion-based, or plasma-based—to prevent nominally static stall or to reduce its negative effects, has been studied for many decades [149]. It therefore comes as no surprise that the same basic concept can be extended to the control of dynamic stall. The problem is characterized by at least two frequencies—pitching and perturbation—represented respectively by k and the reduced frequency:

$$F^{+} \equiv \frac{f_p X_p}{U_\infty} \tag{4}$$

where f_p is the perturbation frequency, and X_p is the distance from the perturbation location to the trailing-edge. Typical effective reduced perturbation frequencies are $F^+ = \mathcal{O}(10^0)$, but they can also be in the $\mathcal{O}(10^1)$ to $\mathcal{O}(10^2)$ range [149,87,150,151,152]. This large range is explained with respect to excitation of the leading-edge bubble, where its length is inversely proportional to the excitation frequency [87,150,151]. The perturbation amplitude is commonly quantified by the unsteady momentum coefficient:

$$\tilde{C}_\mu \equiv \frac{1}{q_\infty A_{\text{ref}}} \int_{\text{act}} \rho_{\text{act}} U_{\text{act}}^2 dA_{\text{act}} \tag{5}$$

which facilitates a comparison between disparate actuation methods; for example, mechanical versus fluidic, or steady [equation (3)] versus unsteady. Higher values of $\tilde{C}_\mu$ are generally required to attach an initially separated flow than to prevent separation of an initially attached flow [153]. Low and high values of C_μ generally indicate whether excitation or forcing is the flow control mechanism. The general rule is that if the perturbation amplitude increases temporally or spatially, then an excitation mechanism is present.

3.5.2.1 The Frequency Disparity

With the introduction of high-frequency periodic perturbations, a large disparity usually arises between the pitching and perturbation frequencies, i.e., $f_p \gg f$, or in non-dimensional form $\pi(F^+/k)(c/X_p) \gg 1$ [154]. This is most commonly achieved with fluidic and plasma-based actuation. The latter [155] almost always relies on an excitation mechanism. AC-DBD plasma actuators rely on a body force, expressed as the momentum coefficient $C_\mu = F_p / q_\infty c$, that is most commonly pulsed modulated at various duty cycles d.c. , hence $\hat{C}_\mu = (\text{d.c.})C_\mu$. Nanosecond pulsed-DC actuators produce localized temperature increase in the form of point thermal bursts, and the sudden point heating generates weak shock waves or acoustic waves.

Examples of light dynamic stall control by open-loop (continuously operating) zero mass-flux blowing $(X_p = c)$ on leading- and trailing-edge stallers, with $\pi F^+/k = 38$, is shown in Figure 14. For both airfoil examples, static effects of control—namely, increases in $C_{l,\max}$ or $C_{m,\min}$—are reflected in the dynamic results. This is an indication that the control mechanisms associated with nominally static (or quasi-steady) stall are also active during dynamic stall. In short, for incompressible dynamic stall control, if it works statically, it will work dynamically.

Note, furthermore, that leading-edge perturbations have significantly different effects on cycle-averaged aerodynamic damping. For the leading-edge staller (NACA 0012 airfoil), the post-stall negative damping (clockwise loop) is significantly diminished. In contrast, for the trailing-edge staller (NACA 0015 airfoil), positive damping associated with the baseline case switches and becomes negative when perturbations are introduced. This effect is not present for control under deep dynamic stall and its effects can be significantly reduced by controlling trailing-edge separation [100].

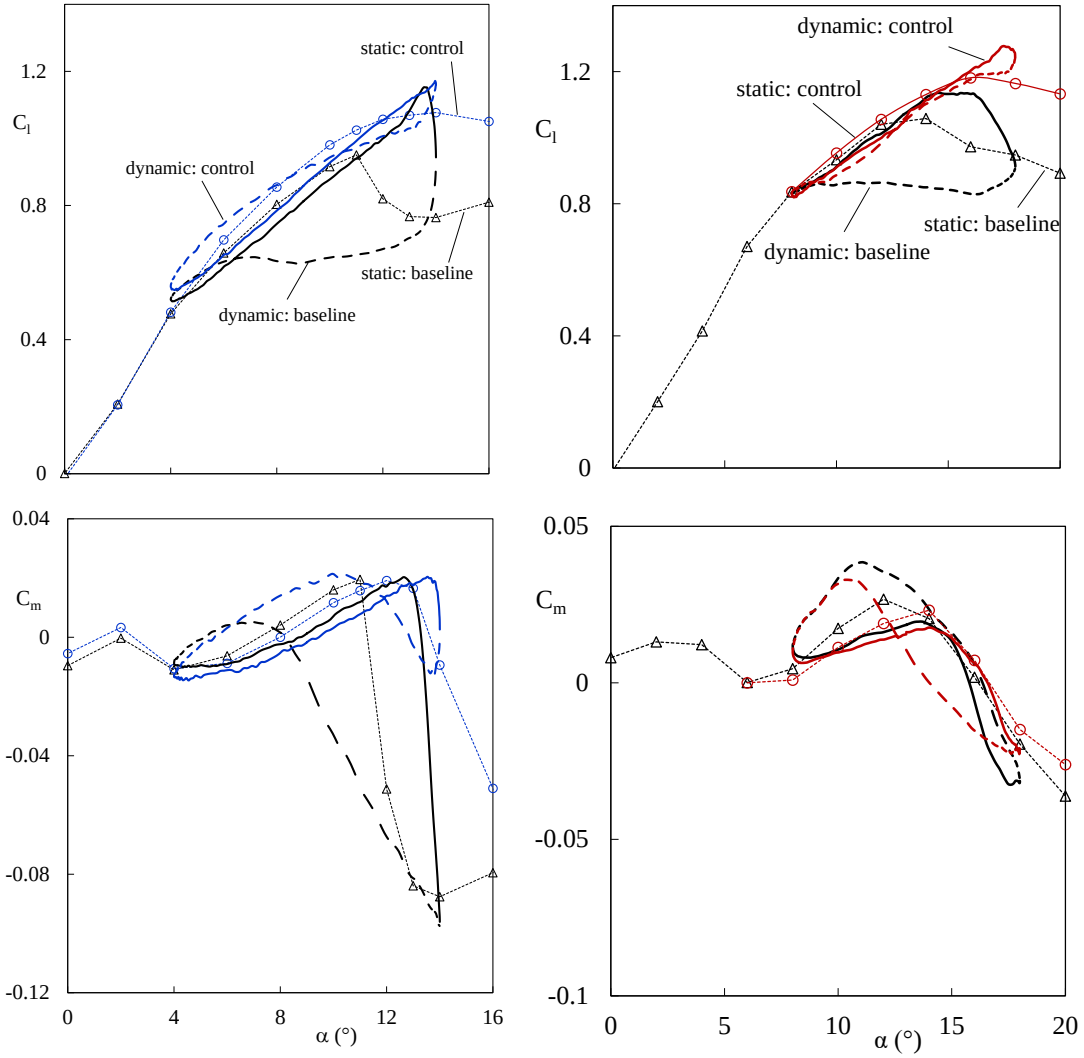

Figure 14. Examples of open-loop dynamic stall control and dynamic stall control ($k = 0.05$) using zero mass-flux blowing. Left: NACA 0012 airfoil, with a 45° slot at $x/c = 5\%$ ($F^+ = 1.5,$, $\hat{C}_\mu = 0.5\%$, $Re = 2.4\times10^5$). Right: NACA 0015 airfoil, with a tangential slot at $x/c = 0$ ($F^+ = 0.6,$, $\hat{C}_\mu = 0.21\%$, $Re_c = 3\times10^5$).

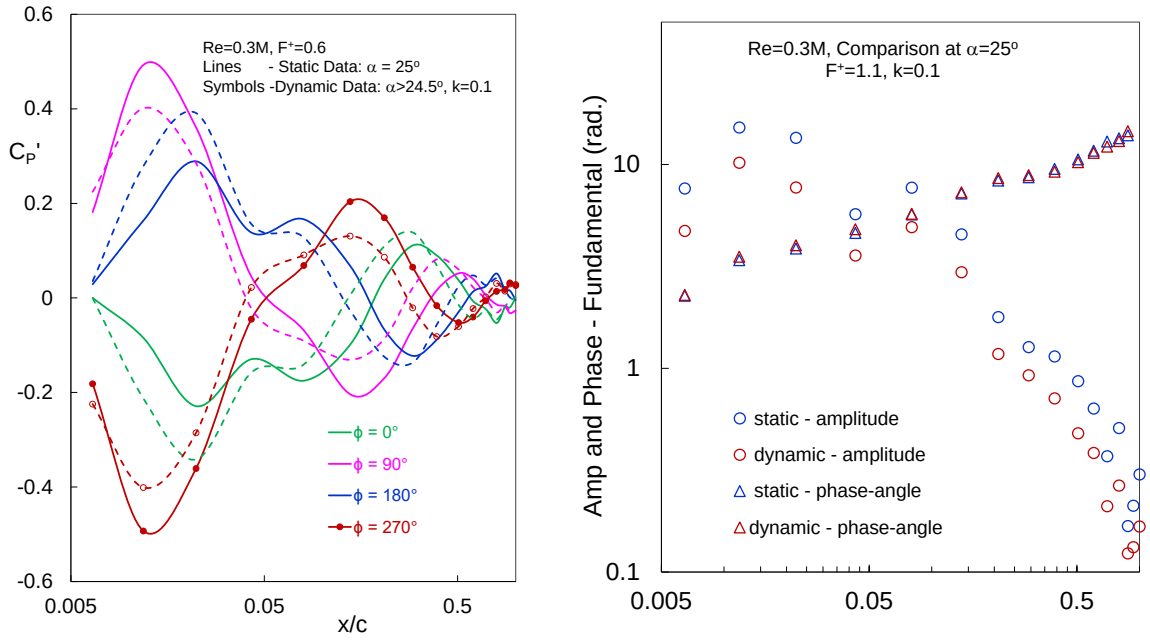

Figure 15. Left: NACA 0015 pressure coefficient amplitudes of the fundamental excitation frequency at four phases ($\pi F^+ / k = 18$) under static conditions at $\alpha = 25°$, and dynamic conditions $\alpha = 20° + 5°\sin(\omega t)$ at $24.5° \le \alpha \le 25°$. Right: Fundamental frequency pressure coefficient amplitude and phase ($\pi F^+ / k = 29$).

Further evidence that static and dynamic pitching control mechanisms are the same can be seen from the NACA 0015 pressure coefficient amplitude of the fundamental excitation frequency (with the average removed) in Figure 15 (left, $\pi F^+ / k = 18$) under static ($\alpha = 25°$) and dynamic (restricted to $24.5° \le \alpha \le 25°$) conditions [154]. The pressure peaks are the "footprints" of the generated vortices [100] as they amplify, and then decay, in the streamwise direction, and it is clear from the upstream amplifications that an excitation mechanism is operating. Importantly, the dynamic amplitudes are similar, and the minor differences are most likely due to dynamic effects, but the fundamental mechanism of vortex generation is not materially affected. Increasing the frequency disparity (Figure 15, right: $\pi F^+ / k = 29$) produces an improved correspondence with virtually identical phase speeds.

It is clear that both dynamic pitching and periodic excitation produce leading-edge vortices: LEVs and a train of vortices, respectively. The key difference, of course, is the governing time-scales. Therefore, excitation under typical helicopter and wind turbine pitching/plunging frequencies can be analyzed under quasi-steady conditions, and consequently no pitching-actuation phase-relation needs to be enforced. The above observations, therefore,

can be summarized in a rhyme inspired by [156]: big whirls have structure when created periodically; and structures have time-scales that determine functionality.

3.5.2.2 Dynamic Stall Functions Application

The dynamic stall functions described in section 3.2 are illustrated in Figure 16 with respect to zero mass-flux control on a NACA 0012 airfoil under dynamic pitching in the ranges $10^5 \le Re_c \le 2.4\times10^5$ and $0.05 \le k \le 0.01$ (cf. Figure 14, left) [138]. Baseline functions $C_{l,\max} = f(C_{m,\min})$ and $C_{l,\max} = f(C_{d,\max})$ (open symbols) are shown, together with high Reynolds number functions from [87]. The differences between the high and baseline-low Reynolds number functions are purely a Reynolds number effect, and apart from the very deep stall case ($\alpha_{\max} - \alpha_s = 14°$), the low Reynolds number baseline data can also be fairly well represented by similar functions. For both functions, the objective is clearly to maintain or increase $C_{l,\max}$ while increasing and decreasing $C_{m,\min}$ and $C_{d,\max}$, respectively. A summary of controlled data points for $F^+ = 1.5$ and increasing $\hat{C}_\mu$ (filled symbols) are shown to illustrate this. At small values of C_μ, relatively small changes to $C_{l,\max}$ are accompanied by significant reductions in $C_{m,\min}$, while increases in $\hat{C}_\mu$, increase $C_{l,\max}$ while maintain the $C_{m,\min}$ increases. It is notable that $C_{m,\min}$ can be maintained with a small negative bracket irrespective of the angle-of-attack range. These data points reflect the elimination of the LEV, by trapping the separation bubble upstream of the blowing slot [138]. Matching $C_{dp,\max}$ data points also show expected reductions with increasing C_μ, consistent with control of the LEV. However, it is not possible to reduce $C_{dp,\max}$ below some threshold that is independent of angle-of-attack, because the contribution of the normal force component to drag increases with angle-of-attack. We can conclude that the comparisons of dynamic stall control methods, based on dynamic stall functions, is a useful filter for initial evaluations and comparisons of different active or passive methods.

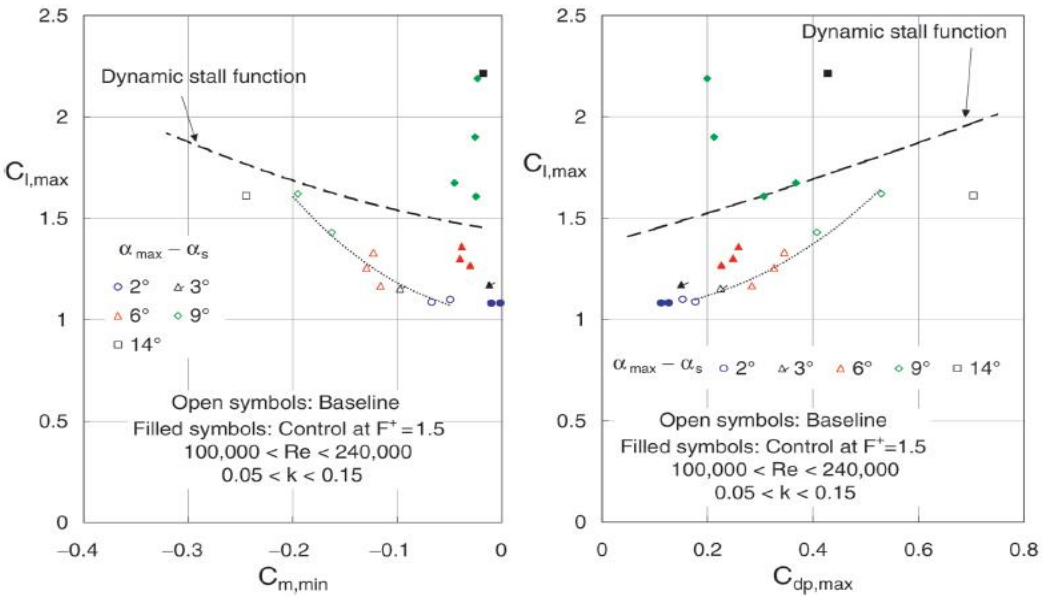

Figure 16. Dynamic stall functions for a NACA 0012 airfoil at high Reynolds number [99], shown with low Reynolds number baseline functions and control data points with zero mass-flux blowing [138].

3.5.2.3 Finite Wings

The similarity between static (or quasi-steady) and unsteady responses to high-frequency actuation, is also observed on low aspect ratio wings. For example, on an $AR = 1$, NACA 0015 wing, $C_{L,\max}$ under quasi-static with $F^+ = 10$ is higher than that with $F^+ = 1$, (corresponding to $\pi F^+ / k = 1050$ and 105, respectively), and the drag rise is delayed by approximately 5 degrees (see Figure 17) [87]. Under dynamic pitching, this is reflected by higher $C_{L,\max}$, smaller C_L hysteresis, and particularly, significantly lower $C_{D,\max}$. Similarly, for static swept and upswept finite wings [157] or static delta wing experiments [158,159], where high-frequency excitation is responsible for aerodynamic improvements, it can confidently be expected that similar results will be attained under dynamic pitching.

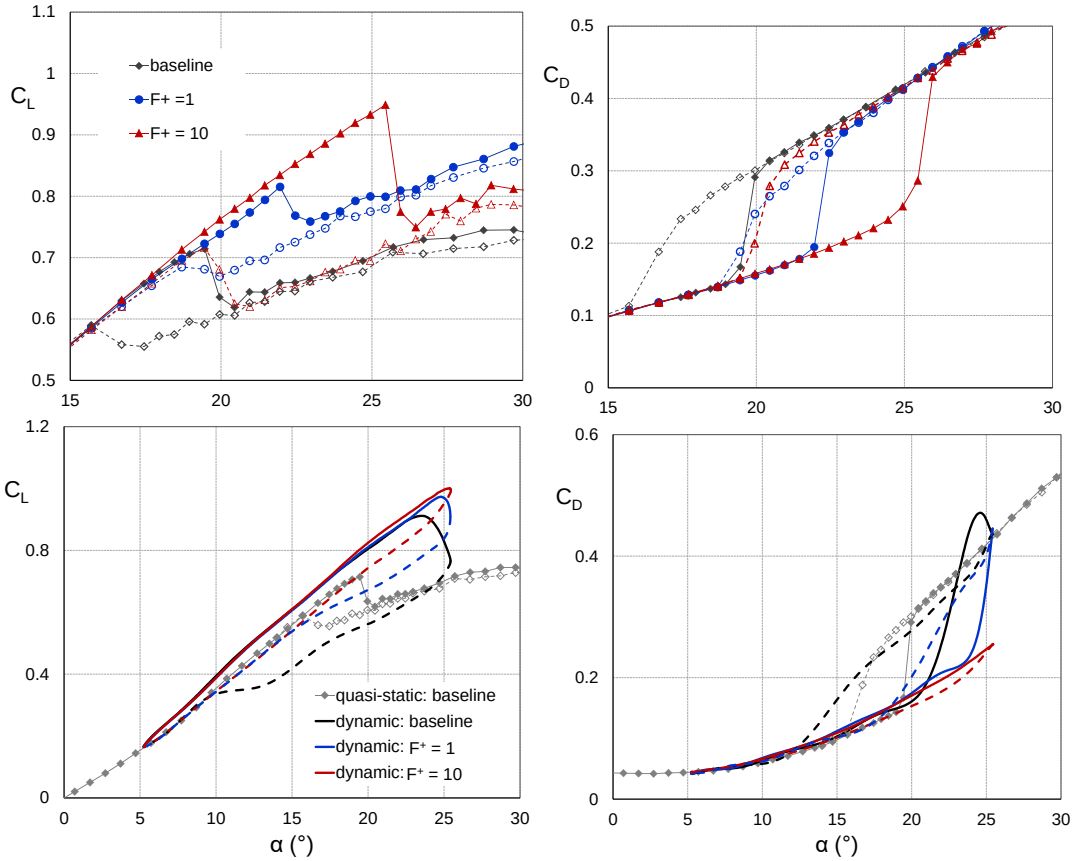

Figure 17. Quasi-static ($\kappa = 0.0001$) and dynamic $k = 0.03$ lift and drag coefficient variation (top and bottom, respectively) with angle-of-attack for baseline and controlled cases [87].

3.5.2.4 Sweep Effects

The study of dynamic stall control under swept conditions has not received direct attention, although we can reasonably assume that results obtained under static conditions are relevant when $\pi F^+ / k \gg 1$. In the case of infinite sweep at an angle Λ—practically where tip effects are negligible—it was shown that the freestream velocity component tangential to the leading-edge plays almost no role in terms of the effects of excitation or forcing, providing that the control parameter definitions are modified as $F^+ / \cos\Lambda$ and $\hat{C}_\mu / \cos^2\Lambda$ [160]. Near a swept back tip however ($\Lambda = 30°$), the effects of leading-edge perturbations degrade significantly, with virtually no meaningful lift enhancement close to the tip, irrespective of the tip shape [157]. This is because the trajectories of the vortices generated at the leading-edge are swept across the span, off the tip and into the wake, thereby having no effect on local circulation. The greater the sweep angle, the larger the outboard span of the tip region is affected. Degradation near swept tips is certainly a consideration for helicopter blades—apart from compressibility effects (see section 4)—that experience periodic inboard and outboard sweep within the rotor cycle, as can be seen from Figure 1 (left). Indeed, the dynamic stall control near swept-blade tips is

clearly critical, irrespective of the control method, but has not been sufficiently evaluated to date.

3.6 Reducing the Parameter Space

In general, aerodynamic bodies translate and rotate with six degrees-of-freedom and therefore can stall dynamically due to translation, rotation, or some combination thereof. When evaluating a dynamic stall control method or strategy—either experimentally or computationally—we would like it to have as general an application as possible, while minimizing the test matrix. For pure pitching this can be done by changing the pitching frequency alone—and not the angle-of-attack excursions—based on the principle of the matched pitch-rate. In addition, we can extend the concept of pitch-plunge equivalence to justify the adoption of pure pitching as being representative of plunging motion. These two concepts are described below.

3.6.1 Matched Pitchrate and Matched Inflow

Under harmonic pitching, where the phase-dependent angle-of-attack is described by equation (1), the matched pitch-rate concept was proposed by McCroskey et al [161]. It asserts that dynamic stall observed under two independent angle-of-attack profiles $\alpha(t)$ are almost identical for $\alpha > \alpha_s$ if the maximum dimensionless acceleration and maximum angle-of-attack are constant, namely:

$$\left|\frac{\ddot{\alpha}c^2}{4U_\infty^2}\right|_{\max} = \alpha_1\left(\frac{\omega c}{2U_\infty}\right)^2 = \alpha_1 k^2 = \text{const.} \tag{6}$$

and

$$\alpha_{\max} \equiv \alpha_0 + \alpha_1 = \text{const.} \tag{7}$$

irrespective of the individual parameter values. This concept can be extended to cases with active flow control, shown with respect to a NACA 0012 airfoil, with and without open-loop (continuous) zero-mass-flux flow control, where the dimensionless accelerations are comparable ($\alpha_1 k^2 = 0.1125°$ and $0.10°$) and $\alpha_{\max} = 17°$ (see Figure 18). It is evident that the close correspondence between the post-stall angle-of-attack profiles results in comparable aerodynamic coefficient time histories. The relatively small differences are likely due to either small differences in $\alpha_1 k^2$, pre-stall unsteady potential flow effects, or hysteresis effects when the airfoil pitches to negative angles-of-attack. Of importance in terms of dynamic stall control, is that the differences between the baseline cases and the control cases are comparable. Thus,

just like the matched pitchrate concept reduces the baseline dynamic stall parameter space, its utility can be extended to problems involving active flow control.

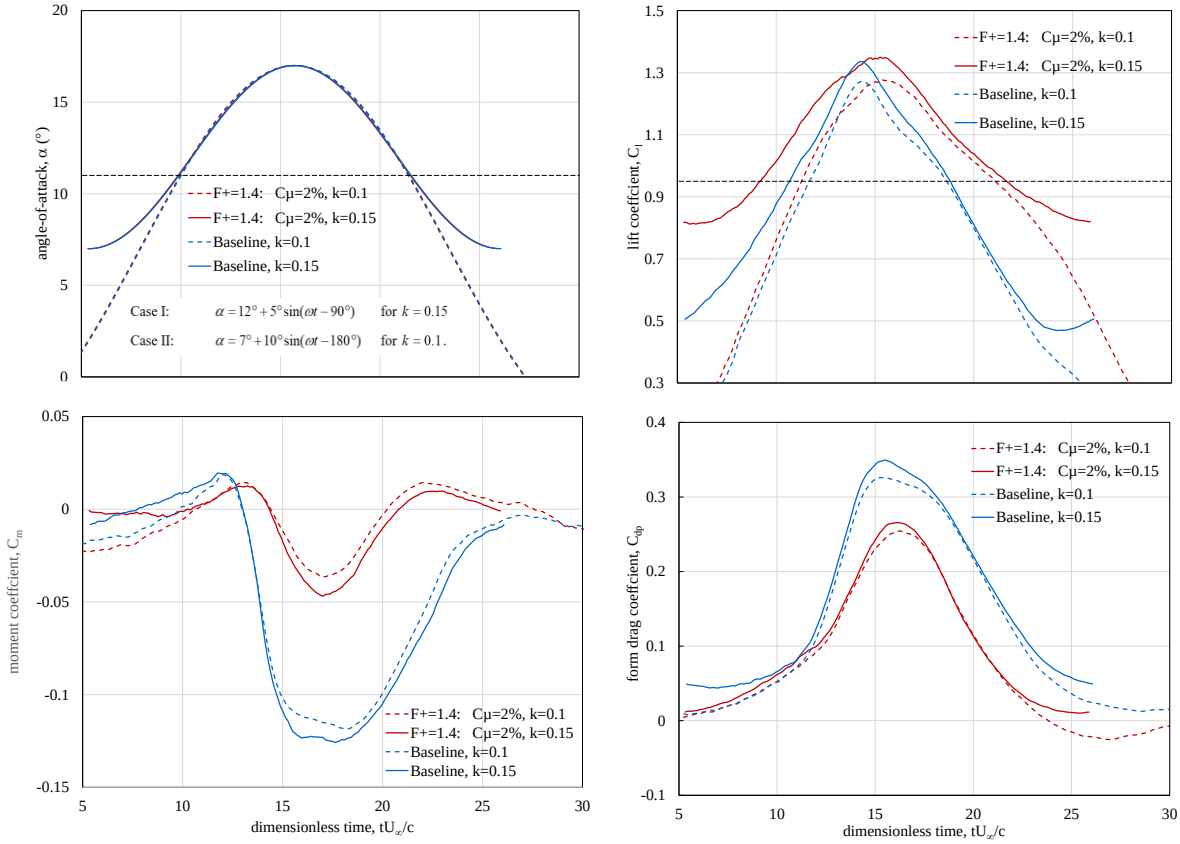

Figure 18. Illustration of the matched pitchrate hypothesis using a NACA 0012 airfoil pitching at $\alpha(t) = 12° + 5° \sin(\omega t - \pi/2)$ with $k = 0.15$ $(\alpha_1 k^2 = 0.1125°)$; and $\alpha(t) = 7° + 10° \sin(\omega t - \pi)$ with $k = 0.1$ $(\alpha_1 k^2 = 0.1°)$.

The matched pitchrate concept can be extended to include variation in the freestream velocity or inflow $U_\infty(t)$, often referred to as surging, by following similar reasoning. Here, we consider the special case where the angle-of-attack [equation (1)] and velocity oscillations occur at the same frequency, with an arbitrary phase difference $(\Delta\phi)$ between them, namely:

$$U_\infty(t) = \bar{U}_\infty + \Delta U_\infty \sin(\omega t + \Delta\phi) \tag{8}$$

which is a common scenario on rotorcraft and wind turbine blades. Then, in addition to the conditions of equations (6) and (7) above, matched inflow requires that the velocity corresponding to the angle-of-attack range between α_s and α_{max} is also matched. Note, however, that when the freestream is not constant, the conventional reduced frequency is not uniquely defined, and therefore we define the nominal reduced frequency based on the cycle-averaged freestream velocity:

$$k_n \equiv \frac{\omega c}{2\bar{U}_\infty} \tag{9}$$

and the instantaneous (or phase-dependent) reduced frequency:

$$k_i(\phi) \equiv \frac{\omega c}{2U_\infty(\phi)} \tag{10}$$

Owing to the fact that the freestream velocity is varying, we now modify equation (6) slightly as follows:

$$\left|\frac{\ddot{\alpha}c^2}{4U_\infty(\phi)^2}\right| = \alpha_1\left(\frac{\omega c}{2U_\infty(\phi)}\right)^2 = \alpha_1 k_i(\phi)^2 = \text{const.} \tag{11}$$

where the inflow velocity $U_\infty(\phi)$ corresponds to phase angle at $(\alpha_s + \alpha_{\max})/2$. Two examples of measured angle-of-attack and freestream velocity (see Table 1) are shown in Figure 19, where $\alpha_{\max}$ corresponds to either accelerating or decelerating flow [162]. The corresponding phase-averaged lift and moment coefficients for two airfoils, namely:

$$C_l(\phi) = \frac{l(\phi)}{\frac{1}{2}\rho U_\infty^2(\phi)c} \tag{12}$$

$$C_m(\phi) = \frac{m(\phi)}{\frac{1}{2}\rho U_\infty^2(\phi)c^2} \tag{13}$$

are plotted in Figure 20 as a function of time in the dynamic stall region. The lift and moment coefficient correspondence for both airfoils in the post-stall regime is excellent. Pressure coefficient distributions, shown in [162], reveal that the essential dynamic stall mechanisms are unaffected. For example, the relatively small S809 airfoil leading-edge radius produces a higher suction peak with earlier shedding of the dynamic stall vortex, while the NACA 0018 exhibits trailing-edge stall, followed by generation of a leading-edge vortex.

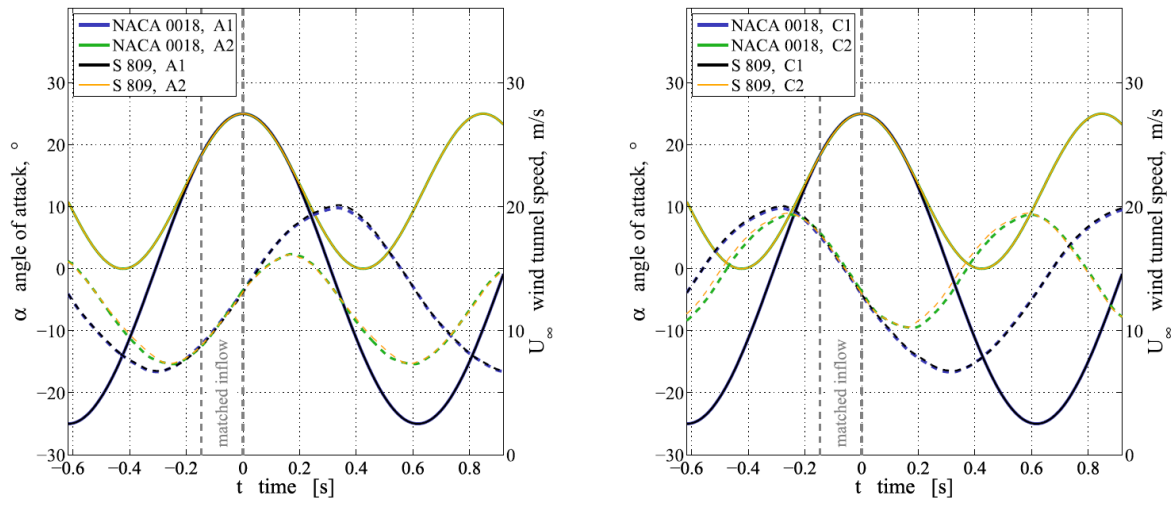

(a) $\alpha_{max} = 25°$, accelerating flow

(c) $\alpha_{max} = 25°$, decelerating flow

Figure 19. Illustrations of the extension of the matched pitchrate concept, to also account for matched inflow.

Under conditions of deep dynamic stall $(\alpha = \alpha_s + 15°)$, that results in large-scale separation, completely neglecting inflow variations of 50% amplitude results in only small differences to C_l and C_m [42]. However, under moderate stall $(\alpha = \alpha_s + 5°)$, neglecting inflow velocity results in material C_l and C_m differences, because boundary-layer transition history effects are not accounted for [42]. It is conceivable that at sufficiently high minimum Reynolds numbers $Re_{min} > 10^6$, surging effects may be significantly reduced.

Table 1. Combined matched pitchrate and matched inflow velocity cases for $18° \le \alpha \le \alpha_{max}$ corresponding to the conditions in Figure 19.

test case	pitching motion	Reynolds number	f (Hz)	k_n
A1	$\alpha = 0° + 25°\sin(\phi)$	$Re = 3\times10^5[1+0.5\sin(\phi-90°)]$	0.81	0.066
A2	$\alpha = 12.5° + 12.5°\sin(\phi)$	$Re = 2.65\times10^5[1+0.38\sin(\phi-70°)]$	1.17	0.11
C1	$\alpha = 0° + 25°\sin(\phi)$	$Re = 3\times10^5[1+0.5\sin(\phi-270°)]$	0.81	0.066
C2	$\alpha = 12.5° + 12.5°\sin(\phi)$	$Re = 3.35\times10^5[1+0.3\sin(\phi-250°)]$	1.17	0.086

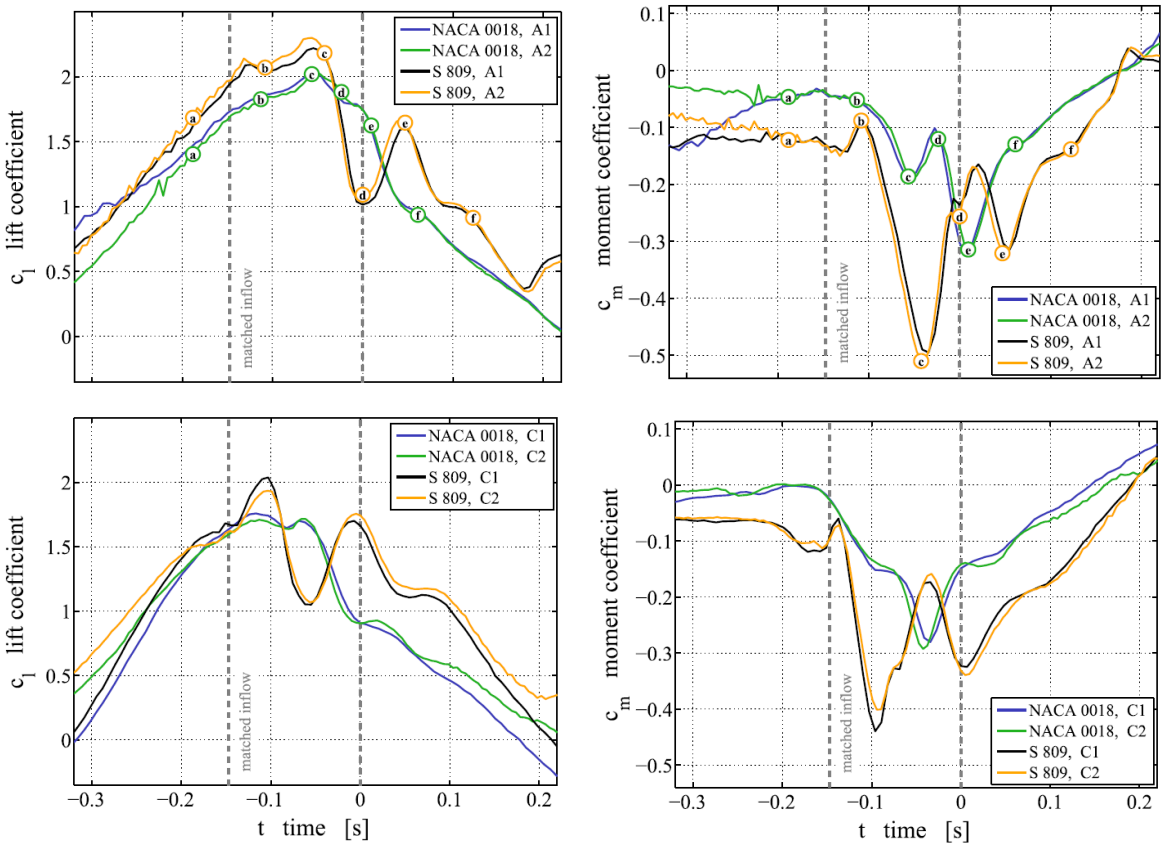

Figure 20. Sample results for lift and moment coefficients, illustrating the validity of the combined matched pitchrate and matched inflow concepts.

3.6.2 The Pitch-Plunge Equivalence

Experimental evaluation of dynamic stall due to pitching motion is practically easier to realize than that due to plunging motion, due to the resultant large mechanical loads that result from translating, rather than rotating, an airfoil or wing. We would like to confidently assume that a control strategy that is successful under pitching will also be successful under plunging. In the study of high Reynolds number problems, with nominally attached boundary layers, [163] used unsteady potential flow theory to develop the well-known pitch-plunge equivalence. This means that the loads experienced by pitching and plunging airfoils can be rendered equivalent under the same angle-of-attack excursions by judicious selection of the pitch-axis x_p. Visbal and Garmann [164] adapted and simplified this equivalence for dynamic stall problems, based on the determination that for a given pitch amplitude, an equivalent plunge amplitude can be determined such that the angles-of-attack match geometrically. The advantage of this simplification is that the concepts can easily be extended to commonly encountered swept wings and blades [165]. Using time-implicit high-fidelity large-eddy simulation (LES, see section

3.11), they demonstrated this equivalence on a finite wing with a NACA 0012 profile and an aspect ratio of 4, undergoing pure pitching motion according to:

$$\alpha(t) = \alpha_0' + \alpha_1'[1 - \cos(\omega t)] \tag{14}$$

[Note the slightly different definitions, when compared to equation (1)]. Independently, the same wing is subjected to pure plunging motion such that its angle-of-attack is equal to the geometric angle-of-attack $\alpha(t)$ of the pitching motion. Hence, for plunging motion prescribed by:

$$h(t) = h_0 \sin(\omega t) \tag{15}$$

the angles-of-attack are matched when $h_0 = (c/2)\tan(\alpha_1')/2k$. With direct matching of the geometric angles, the correspondence of the aerodynamic coefficients is reasonable as shown in Figure 21. Next, [164] employed quasi-steady thin airfoil theory to account for motion-induced variations in angle-of-attack along the chord associated with pitching. This manifests as apparent positive or negative camber, which is a function of $\dot{\alpha}$, during pitch-up and pitch-down motions, respectively. Using thin airfoil theory for a cambered airfoil, it was shown that the apparent camber effects are accounted for by the correction terms:

$$\Delta C_{L,\text{cam}} = -\left(\frac{dC_L}{d\alpha}\right)_s \left(x_p - \frac{3}{4}\right)\dot{\alpha}\cos\alpha \tag{16}$$

and

$$\Delta C_{M,\text{cam}} = -\frac{\pi}{8}\dot{\alpha}\cos\alpha \tag{17}$$

which are subtracted from the original pitching results and shown in Figure 21. This simple correction significantly increases the correspondence with the plunging results.

Notably, the dynamic stall mechanism was not materially affected along the entire span of the wing. Similar results were observed on swept finite-wings [165], where steady thin-airfoil theory was extended to again produce excellent C_L and C_M correspondence between pitching and plunging. Of significance from a control viewpoint, is that we can assume that control techniques that are effective under pitching motions, will also be effective under equivalent plunging motions. These results can be leveraged to assess the effects of active flow control techniques discussed above to flapping wing aircraft like ornithopters, where the onset of dynamic stall is associated with reduction of lift and propulsive efficacy [13] (see section 3.10.1).

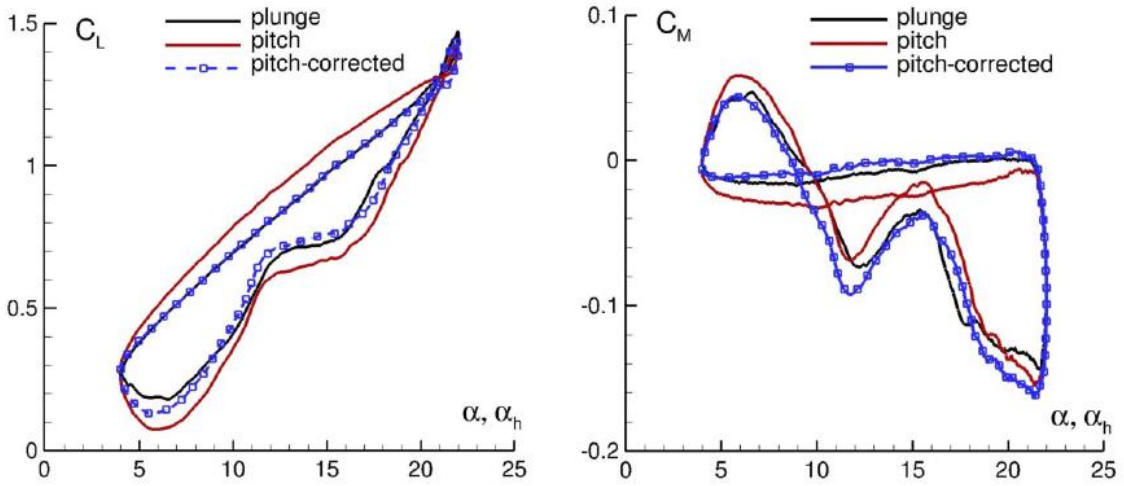

Figure 21. NACA 0012 wind of aspect ratio 4 undergoing independent pitching and plunging motions at matched angles-of-attack ($h_0 = (c/2)\tan(\alpha_1)/2k$) showing the effect of rotation-induced apparent camber on lift and ¼-chord pitching moments [164]. Results reproduced with permission.

3.7 Scheduled Control

In simple scheduled control, actuator input is varied according to some external variable or operating condition, such as angle-of-attack, wind speed or an externally-imposed frequency. In this section we merely use it as a vehicle to describe various applications of externally imposed periodic separation and attachment. This is most easily demonstrated on a pitching airfoil, where leading-edge perturbations are initiated and terminated at predetermined pitch-up stall and pitch-down reattachment angles, respectively [149]. It can also be applied on the aft part of an airfoil or at the shoulder of a deflected flap, with the objective of increasing lift excursions [166]. In this application, the flow is forced to dynamically separate and attach from the surface at predetermined angles-of-attack as shown in Figure 22. In contrast to airfoil leading-edge perturbations, the times-scales governing separation and reattachment scale with the flap-length and this increases the pitching/excitation frequency disparity, namely $(\pi F^+/k)(c/L_f) = 138$, as discussed in section 3.5.2.

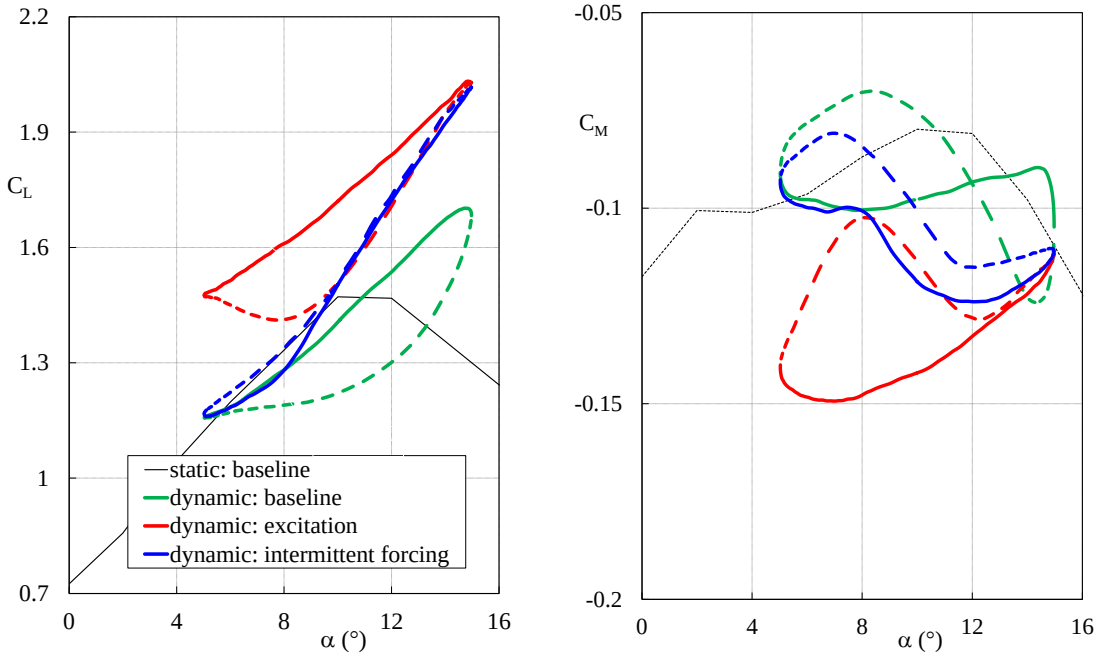

Figure 22. NACA 0015 airfoil dynamic pitching at $\alpha(t) = 10° + 5° \sin(\omega t)$, $k = 0.1$ and $Re = 3.0 \times 10^5$ with $\delta_f = 20°$ and flap-shoulder forcing. Scheduled initiation and termination of forcing (intermittent forcing) at $F^+ = f_p L_f / U = 1.1$ and $\tilde{C}_\mu = 2\%$ $(\pi F^+ / k)(c / L_f) = 138$.

The attachment time is usually expressed in terms of the convection time, namely $\tilde{\tau}_{\text{att}} \equiv T_{\text{att}} U_\infty / X_p$ and varies widely $(2 \geq \tilde{\tau}_{\text{att}} \leq 10)$ depending upon the perturbation amplitude and frequency [27,26]. The time-scales governing boundary layer separation following cessation of perturbations T_{sep} are $\tilde{\tau}_{\text{sep}} = T_{\text{sep}} U_\infty / X = \mathcal{O}(10^1)$ [27,3]. The timescales T_{sep} and T_{att} are important for estimating the actuation bandwidth $f_c \approx 1/(T_{\text{sep}} + T_{\text{att}})$, which inform the plant models for feedforward and feedback control, discussed in section 3.9.2. In the sections below, selected examples of scheduled control are shown, with potential application to rotorcraft wind wind energy, and the control of streamwise vortices and turbulent mixing.

3.7.1 Unsteady Coandă Effect

Ghee and Leishmann [167] demonstrated the potential of periodic separation and attachment on a circular cylinder using the Coandă effect. By harmonically varying the momentum coefficient, peak lift coefficients significantly exceeded corresponding steady values and average drag was reduced substantially. For example, lift coefficient excursions increased by a factor of 2.6 at $k = 0.542$, and average drag was approximately halved at $k = 0.069$. While this research was aimed at rotorcraft applications, it can be extended to substantially increase the net power output of energy harvesters that otherwise rely on vortex-induced vibrations

(VIV) [168-170]. Conventional VIV energy harvesters are self-regulating and lock-in occurs over a relatively narrow frequency range close to the natural frequency of the system [171-173]. In contrast, periodic separation and attachment can be imposed at frequencies unrelated to vortex shedding, but that are close to the system's natural frequency [141,174]. By introducing alternate period slot blowing on opposite sides of a cylinder [175-178], at $C_\mu \geq 0.04$, almost four times greater net power output, and more than seven times greater bandwidth, can potentially be obtained, relative to conventional VIV energy harvesters.

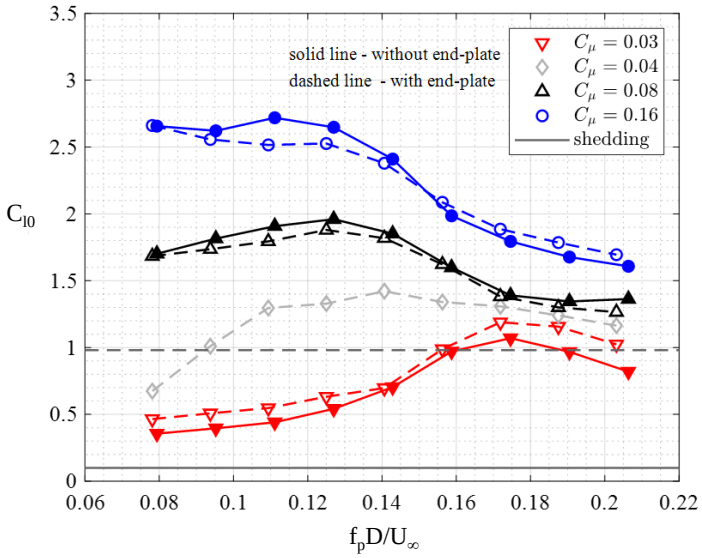

Figure 23. Lift coefficient amplitude as a function of jet blowing frequency, expressed as a Strouhal number : dashed line and open symbols – cylinder with endplate; solid line and filled symbols – free end cylinder: $Re = 5\times10^4$.

3.7.2 Vertical Axis Wind Turbines

It was shown in section 3.2, that the management of dynamic stall is a critical factor in the performance of high-solidity vertical axis wind turbines. It therefore comes as no surprise that control of dynamic stall increases turbine performance [106,179]. The performance of a model VAWT with and without (baseline) continuously-operated DBD plasma actuators mounted on the blade leading-edges is shown in Figure 24, together with example flowfield measurements at $\theta = 120°$. At $\lambda = 1.74$, when the baseline turbine is unloaded, perturbations suppress the growth of the LEV, but the AV is larger and stronger. A similar conclusion can be drawn when the turbine is under an intermediate load at $\lambda = 1.56$, where the changes to the power coefficient resulting from actuations are comparable. Under the maximum load (peak power coefficient) at $\lambda = 1.37$, surprisingly, neither vortex is eliminated; rather, both are smaller with higher levels of vorticity, as confirmed by consideration of the Okubo-Weiss parameter [106]. The increases

in turbine power shown in Figure 24 are relatively small, because (i) actuation was introduced, (ii) the turbine speed increased under constant load, and (iii) the load was increased to return the turbine to its baseline speed (but with higher torque). When separate gradual loading experiments were for baseline and controlled experiments individually [179], far larger power output gains were observed—more than 30% increase—indicating a strong sensitivity to initial conditions.

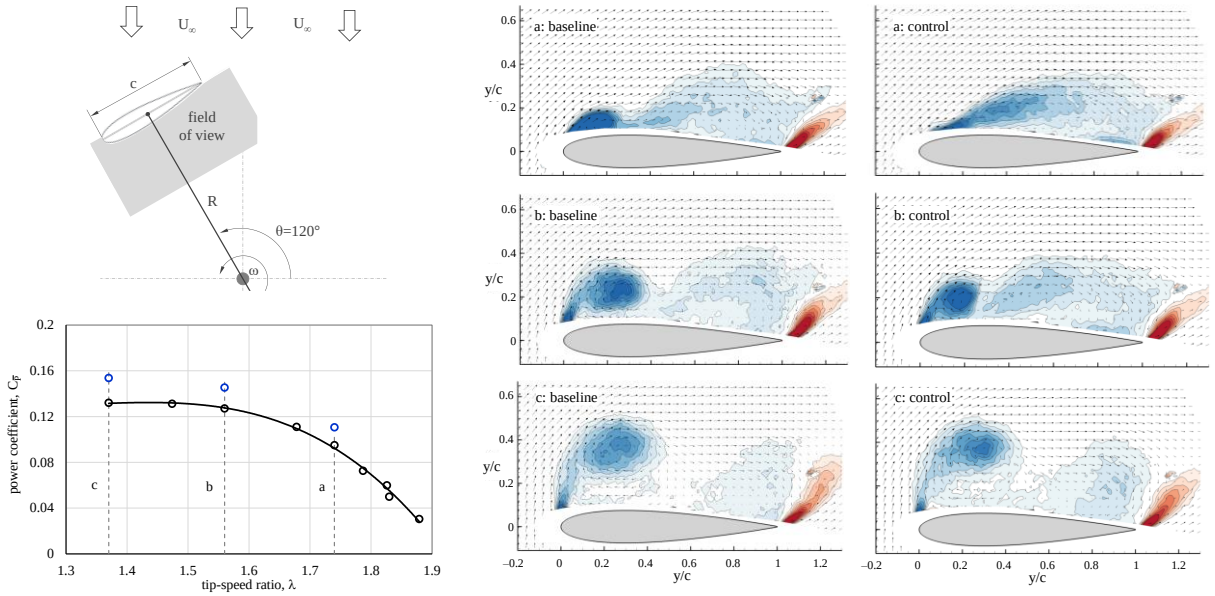

Figure 24. VAWT performance chart and corresponding flowfield based on PIV measurements for baseline and AC-DBD plasma actuation [106,179].

Although the gross turbine power output increased by more than 30% due to actuation, the power input to drive the continuously-operated actuators exceeded the power gained by the turbine. To address this, systematic scheduled control was implemented by initiating and terminating perturbations at predetermined angles, θ_i and θ_t, relative to the flow direction shown in Figure 25 (left) [180]. Turbine rational speed was measured under constant load for the ranges $0° \le \theta_i \le 80°$ and $20° \le \theta_t \le 180°$; hence changes in turbine power $\Delta\bar{P} \propto \Delta\omega$. When perturbations were introduced at $40° \le \theta_i \le 70°$, there was always a positive result, with saturation at $\theta_t \approx 110°$, termination at $\theta_t > 110°$ merely increased input power without an increase in turbine power. Furthermore, for actuation at $\theta_i > 70°$, the control authority decreased, and therefore no additional turbine power was produced outside of the range $70° \le \theta \le 110°$. When actuation was limited to this range, a net power output $(\Delta\bar{P} - \bar{P}_{in})/\bar{P}$ of

10% was realized. This azimuthal range corresponds to the approximate angle-of-attack range $27° \le \alpha \le 40°$ and it is interesting that positive effects are observed when perturbations are applied at angles significantly larger than the static stall angle $\alpha_s = 12°$. It is likely that the rapid pitch up delays separation, and actuation is only required during the formation of the LEV.

Scheduled control was merely employed here for proof-of-concept purposes. Closed-loop control, based on adaptation of stall warning sensing, as described in section 3.9.1, can easily be incorporated into the present application.

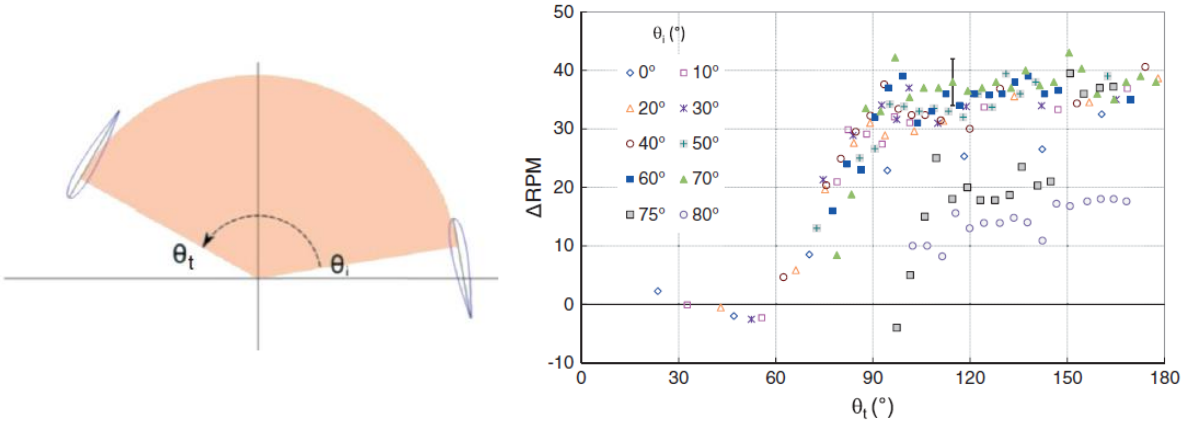

Figure 25. Effect of azimuthal initiation and termination angles on turbine rotation speed under constant load. Plasma burst modulation $f_p = 500$ Hz $(F^+ > 4.2)$, duty cycle d.c. = 20%, and $U = 7.0$ m/s. Sample standard deviation bar shown for 95% confidence interval [180].

3.7.3 Trailing Vortex Control

It was shown at the beginning of this section, that separation from, and attachment to, a flap brings about periodic (or cyclic) changes to its bound circulation Γ. When applied on finite flaps, local cyclic changes in bound circulation affect the shed vorticity (or vortex sheet strength) $\gamma(y,t) \equiv \partial\Gamma / \partial y$ and hence the trailing vortices, based on modifications to Betz's vortex rollup relations [181]. The periodic separation from, and attachment to, a flap can be exploited to dynamically perturb trailing vortices, discussed in this section, or enhancement turbulent mixing described in 3.7.4, below.

The desire to control trailing vortices has wide application on fixed and rotary wing aircraft. For example, on fixed wing aircraft, the vortices generated by large airliners can pose a serious safety risk to smaller aircraft that follow in close proximity [182,183]. This has motivated many attempts to destroy or dissipate the vortices—for example by "turbulence injection" into the vortex core—or directly excite vortex instabilities by periodically displacing

them (see references in [181]). On helicopters, a major source of noise is due to blade-vortex interaction (BVI), where the blade tip vortices interact with the following blades—producing large unsteady pressure fluctuations—during descent, slow flight, and maneuvering [184]. Methods for reducing BVI noise reduction focus on influencing the vortex structures and their trajectories, and include variations in tip design, higher-harmonic pitch control (HHC) and individual blade control (IBC) and active flaps [184,185].

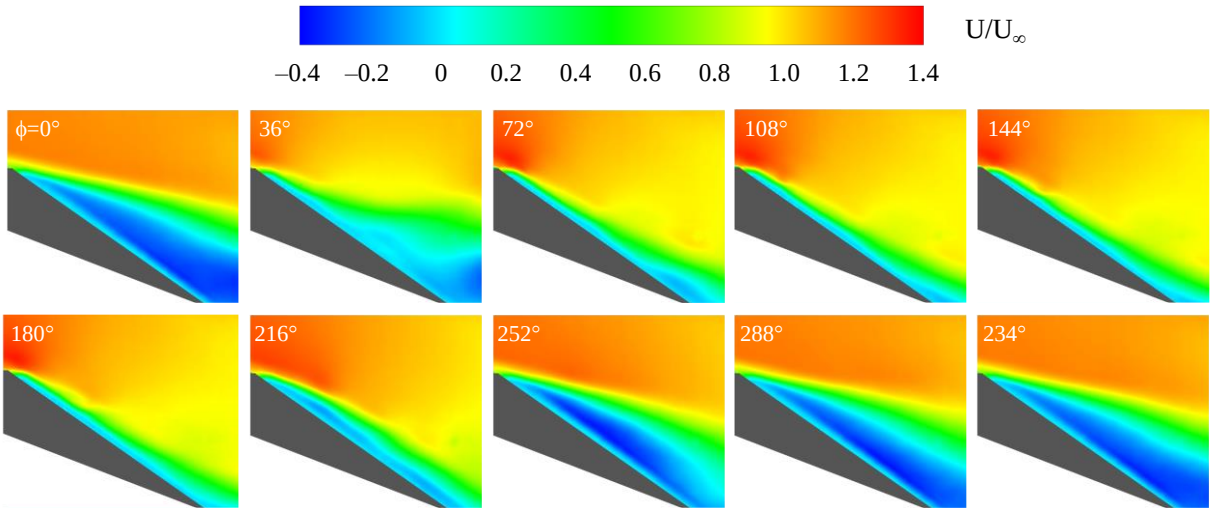

Figure 26 Non-dimensional streamwise velocity U/U_∞ above a deflected tip flap ($\delta_F = 20°$) center-span at $F^+ = 0.78$ and $C_\mu = 0.011\%$, based on 2D PIV measurements, with pulse-modulation corresponding to $F^+/24$ ($\lambda/c = 8$). Pulse-modulation initiation at $\phi = 0°$, termination at $\phi = 180°$.

In contrast to the above techniques, dynamic separation and attachment can exert large control authority over the structure and trajectories of the vortices, either by amplitude (C_μ) or frequency (F^+) modulation. Figure 26 shows PIV measurements of the cyclic separation and attachment of flow over the midspan of tip-flap deflected at $\delta_f = 20°$, where the high-frequency control input $F^+ \equiv f_p L_f / U_\infty = 0.78$ is pulse-modulated at $F^+/24$, corresponding to a wavelength $\lambda/c = 8$. Pulse-modulation is applied with a 50% duty cycle, initiated at $\phi = 0°$ and terminated at $\phi = 180°$. At $\phi = 36°$ the upstream part of the flap is partially attached and clockwise dynamic stall vortex is shed downstream of the trailing-edge, and at $\phi = 72°$ the flap flow is mainly attached, i.e., $T_{att} U_\infty / L_f \approx 5$. The separation process, as expected, is much slower with full shear layer separation not fully realized by the end of the cycle, i.e.,

$T_{sep}U_\infty / L_f \approx 12$. On inboard flaps, lateral displacement of vortices can be estimated using Betz's rollup relations as modified by Donaldson [181].

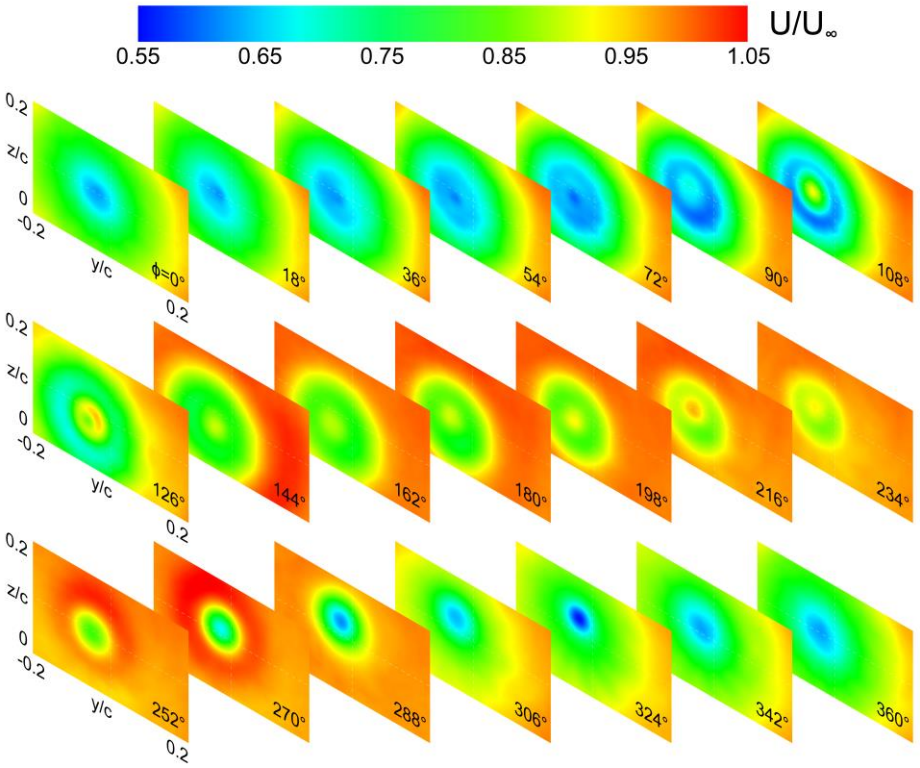

Figure 27. Axial flow U_x / U_∞ in wake aft of the wingtip, from stereoscopic PIV measurements, corresponding to the cyclic flap separation and attachment shown in Figure 26.

The axial vorticity distribution in the trailing vortex in cylindrical coordinates (x, r, θ) shown in Figure 27, depends on the nature of the shear layer—between fully attached and fully separated—that is entrained into the vortex. In particular, the axial flow can jet-like $(U_x / U_\infty > 1)$ or wake-like $(U_x / U_\infty < 1)$, because it depends on both the time-dependent azimuthal velocity distribution $V_\theta(r,t)$ and frictional (head) losses $\Delta H(t)$ [186]. Under quasi-steady conditions, this can be expressed as:

$$\frac{U_x^2}{U_\infty^2} = 1 + \underbrace{\frac{1}{U_\infty^2}\int_0^\infty \frac{1}{r^2}\frac{\partial V_\theta^2}{\partial r}\,dr}_{\substack{\text{pressure drop} \\ \text{in the vortex}}} - \underbrace{\frac{2\Delta H}{U_\infty^2}}_{\substack{\text{frictional losses} \\ \text{in the vortex}}} \qquad (18)$$

and we can identify two mechanisms that drive the axial flow magnitude and sign [187]. The right-hand side of equation (18), shows that a separated flap flow results in a diffuse vortex and

hence a small pressure drop from first term, with large viscous/turbulent losses in the second term, thereby producing a wake-like axial flow. In contrast, for attached flow, the azimuthal velocity gradients are large, resulting in a large first term and a small second term, thereby producing a jet-like flow. In the cyclic dynamic case, initiation of perturbations produces a spanwise starting vortex that is entrained into the tailing vortex, and this produces large vertical deflections of the vortex centroid—namely 5.2% of chord, versus 0.9% for the quasi-steady case—and indicates apparent "buckling" of the vortex (not show, see [28]).

When applied to a problem of aerodynamic relevance, the existence of a separated or partially separated shear layer will generally result in aerodynamic performance losses. For purposes of practical implementation, a central consideration will relate to the toleration of a temporary aerodynamic performance loss for the purpose of achieving a secondary objective, for example, wake excitation or noise reduction.

3.7.4 Turbulent Mixing Enhancement

In turbulent flows, large-scale coherent vortical structures are primarily responsible for transporting momentum, energy, and scalar quantities (like temperature or concentration) across large regions of the flow [188-190]. While molecular-level mixing ultimately occurs at the smallest (dissipative) scales, it is the large-scale structures that initiate and sustain mixing, by stretching and folding fluid parcels to create sharp gradients that the smaller-scale turbulence can then act upon.

We noted in section 3.7.3, that both spanwise and streamwise vortices can be generated by cyclic separation and attachment on finite-span flaps. Here, we illustrate an example of mixing enhancement within a circular jet-flow of velocity U_0, whose perimeter is equipped with deflected flaplets as shown in Figure 28 (top left) [191], where the slot-jet velocity varies according to $U_j = U_{j,\max} \sin 2\pi f_p t$. This is characterized as low-frequency forcing, because the perturbation time-scale corresponds to the dynamic separation-and-attachment time-scale. Following the analyses of [190], mixing rate augmentation due to streamwise vortices is expressed as:

$$\left(\frac{\partial M}{\partial (x/\lambda_f)} \right) \propto \frac{\Gamma^{2/3} D_t^{1/3}}{U_0 \lambda_f} \tag{19}$$

where Γ is the shed circulation in the plane perpendicular to the jet axis, D_t is the turbulent diffusion coefficient, and λ_f is the distance between the flaplets. When we introduce cyclic

disturbances at the flap slots, the shed circulation is dependent on the control parameters, as follows:

$$\Gamma = \int_A |\, \omega_x(\delta_f, F^+, C_\mu) \,| \, dA \tag{20}$$

where $\delta_f = 30°$ is the flap deflection angle. On the basis of stereoscopic PIV measurements, the relative change in mixing augmentation was quantified as:

$$\Delta M(x) = \frac{M(x, F^+, C_\mu) - M_b(x)}{M_b(x)} \tag{21}$$

where M_b is the baseline flow, i.e., without flow control.

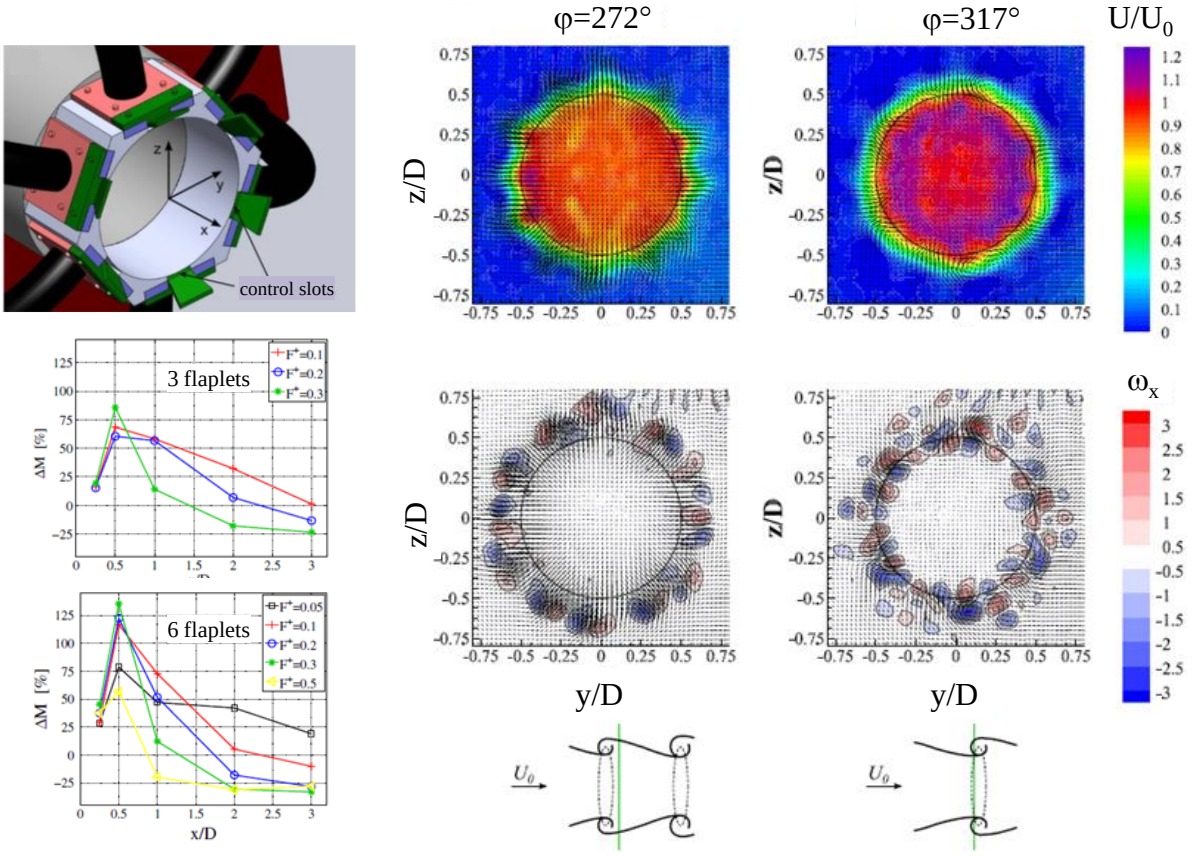

Figure 28. Left-top: Turbulent mixing enhancement experimental setup. Top-right: Phase-averaged normalized streamwise velocity and streamwise vorticity at illustrative phases for $x/D = 1$ with 6 flaplet slots active ($\lambda_f = \pi D/6$). Bottom-right: Corresponding passage of spanwise coherent structures. Bottom-Left: Mixing augmentation as a function of downstream direction relative to the baseline, see equation (21), for 3-flaplet and 6-flaplet configurations ($\lambda_f = \pi D/3$ and $\lambda_f = \pi D/6$, respectively).

Figure 28 (bottom-left) shows the effect of reduced frequency on mixing augmentation at two selected phases in the cycle. The greatest overall effects are observed at the lower reduced frequencies $F^+ = 0.05$ and 0.1, and these frequencies correspond to cyclical separation and attachment of the jet flow to the flaplets. Selected representative phases of 272° and 317° are shown in Figure 28. At 272°, the flow is attached to the flap as can be seen by the strong radial outflow from the perimeter of the jet and this results in slight reductions in the jet core velocity. At 317°, local spanwise vortices are entrained into the jet increasing the core velocity by approximately 20%. In terms of axial vorticity, one would expect a vortex pair associated with each flaplet, but it is in fact twice this number.

3.8 Iterative Learning Control

The cyclic—and therefore repetitive—nature of dynamic stall on helicopter and wind turbines, as well as flapping wing flyers, makes it an ideal candidate for iterative learning control (ILC). Indeed, various forms of ILC are routinely used for helicopter wind turbine applications [192,193]. Two advantages are that disturbance and plant models (see section 3.9.2) are not required and that non-linear responses to the control inputs can be relatively easily accounted for. For blades, the objective is typically to minimize oscillatory loads throughout the cycle—for example $C_{n,\mathrm{exc}}$ or $C_{m,\min}$ (see section 3.2), or to attain a predetermined load phase-dependence. Here, each rotation of the blades is considered to be an iteration, where loads are measured or estimated by a sensor or several sensors. After each iteration, the difference (error) between the desired and measured phase-dependent loads are calculated and the dynamic stall control phase-dependent input is based on the error from previous iterations.

By way of example, we will focus our attention on idealized HAWT dynamic stall control using leading-edge slot blowing over some fraction of the blade span described by [21]. This approach falls under the general heading of "smart rotor control," which aims to dynamically minimize unsteady loads [194]. As discussed in section 3.5.1, slot blowing has a large control authority that can both suppress (or eliminate) and induce separation—and therefore dynamic stall—with no moving mechanical parts. In the examples presented here, the objective is to use low-frequency (on the order of the pitching cycle) slot blowing to maintain static lift-force set points under synchronous variations in angle-of-attack and freestream velocity. The motivation is clearly minimization of flapping-mode loads [98].

A quasi-static lookup table of the form $C_{l,\mathrm{qs}} = C_{l,\mathrm{qs}}(\alpha, C_\mu)$ was generated for the range $-5° \le \alpha \le 35°$, and 16 jet velocities corresponding to $0.5\% \le C_\mu \le 6.5\%$, and the derivatives

$\partial C_{l,\mathrm{qs}} / \partial C_\mu$ were calculated (see section 3.5.1). For the initial iteration $(k=1)$, $C_{\mu,1}(\phi) = f(L_{\mathrm{sp}})$ was obtained from the lookup table using linear interpolation. The lift per unit meter $L_1(\phi)$ was measured by integrating the surface pressures and the first iteration error was calculated, namely $\Delta L_1(\phi) = L_1(\phi) - L_{\mathrm{sp}}$. The momentum coefficient correction term was then calculated from the lookup table and hence the correction terms $\Delta C_{\mu,1}(\phi) = -\lambda_G \Delta L_1(\phi)$ were calculated, where $\lambda_G = [\partial C_{l,\mathrm{qs}}(\phi) / \partial C_\mu(\phi)]^{-1}$ is the learning gain. Subsequent iterations were performed according to:

$$C_{\mu,k+1}(\phi) = C_{\mu,k}(\phi) + \lambda_G [\Delta L_k(\phi)] \tag{22}$$

Specifically, the objective is to maintain constant lift per unit span, i.e., a constant setpoint L_{sp}, under synchronous angle-of-attack:

$$\alpha(\phi) = \alpha_0 + \alpha_1 \sin(\phi + \tau) \tag{23}$$

and freestream:

$$U_\infty(\phi) = \bar{U}_\infty [1 + 0.2 \sin\phi] \tag{24}$$

variations, for antiphase $(\tau = 180°)$ and in-phase $(\tau = 0°)$ cases. The former $(\tau = 180°)$ represents a HAWT in yawed flow [52-54]; and the latter $(\tau = 0°)$ is representative of a strong periodic gust, or the pitching of a FHAWT normal to the disk plane [55-57] (see Figure 3 in section 2.2).

Phase-averaged results for $L_{\mathrm{sp}} = 30$ N/m and 60 N/m with $\tau = 180°$ are shown in Figure 29, together with the baseline L and the effect of steady (constant) blowing. It is clear from the baseline lift loops that the dynamic pressure q_∞, which varies by a factor of 2.25, has a greater effect than the angle-of-attack oscillation, with the maximum lift occurring at $\alpha_{\min}$. This can also be seen when steady blowing suppresses dynamic stall, resulting in a negative lift slope $\partial L / \partial \alpha$. Another factor, generally not appreciated, is that baseline lift change due to attachment near $\alpha_{\min}$ is approximately twice that associated with the shedding of the LEV. Relatively few studies focus on the attachment phenomenon [76-79], even though from the point of view of unsteady loading, it can be at least as important as dynamic separation.

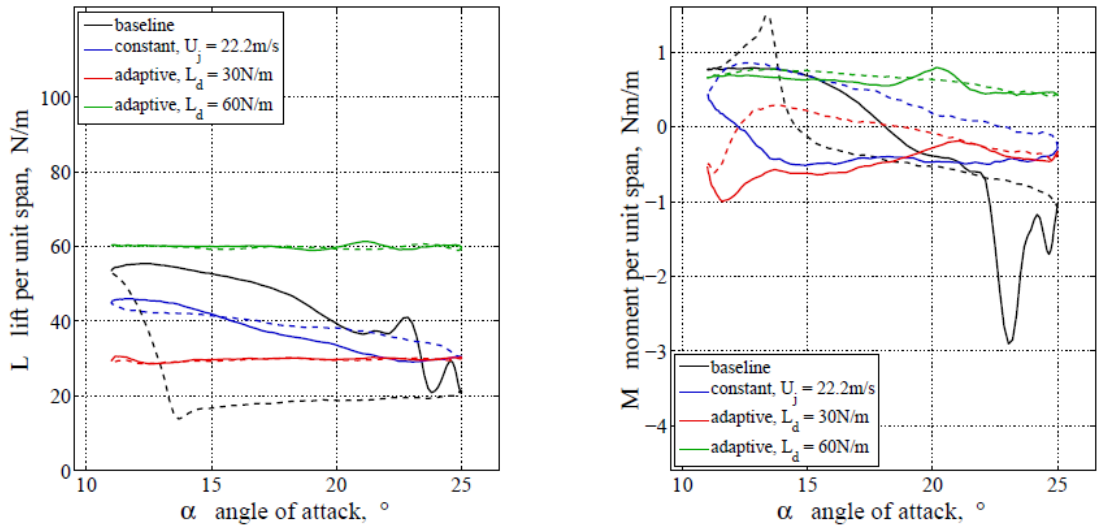

Figure 29. Phase-averaged dimensional aerodynamic loads under anti-phase harmonic pitching and surging: $\alpha(\phi) = 18° + 7°\sin(\phi + \pi)$ and $Re_c(\phi) = 3\times10^5[1 + 0.2\sin\phi]$ at $k_n = 0.06$, illustrating the results of ILC for lift control.

The counteracting effects of α and q_∞ facilitate a large control authority as shown by the attainment of the two setpoints in Figure 29. At the higher setpoint, which lies entirely above the baseline excursions, dynamic stall is always suppressed to some degree. Moreover, disproportionally higher slot momentum is demanded near $\alpha_{\max}$, due to the reduction in $\partial C_l / \partial C_\mu$ at high values of C_μ (see Figure 10 in section 3.5.1). At the lower setpoint, which lies both above and below the baseline lift, both the promotion and suppression of dynamic stall are required depending upon the phase angle of the cycle. The reduction in lift excursions brings about significant reduction in moment excursions as well. For $L_{sp} = 60$ N/m the excursions are virtually eliminated, and for $L_{sp} = 30$ N/m the excursions are reduced by more than a factor of 3. The difference is likely due to the fact that separation is eliminated or suppressed throughout the cycle at the higher set point. Moreover, negative damping associated with the baseline case (see section 3.2) is eliminated under both constant blowing and ILC cases. In principle, it is possible to eliminate moment excursions, by simply replacing the setpoint L_{sp} with M_{sp}, but this may come at the cost of larger lift excursions. For both setpoints, no minimum error or convergence criterion was enforced, although after approximately 10 iterations the average error, defined as:

$$L_{\text{err}} = \left(\frac{1}{N} \sum_{j=1}^{N} (L_k(\phi) - L_{\text{sp}})^2 \right)^{1/2} \tag{25}$$

saturated.

Phase-averaged results for $L_{\text{sp}} = 40$ N/m with $\tau = 0°$ are shown in Figure 29, together with the baseline L and two constant jet velocities. The baseline results show that the in-phase variation of α and q_∞ produced excessively large lift excursions, between 6 and 71 N/m, although instantaneous values were even larger, between ~0 to ~100 N/m. Steady blowing at $U_j = 40$ m/s and 17 m/s are also shown, because they furnish an indication of the minimum and maximum achievable values of *L*. At $\alpha_{\min} < \alpha_s$, blowing with $U_j = 40$ m/s relies on a combination of aft separation and circulation control ($C_\mu = 9.5\%,\ C_l \approx 1.7$) to attain 40 N/m. Conversely, at $\alpha_{\max}$, $U_j = 17$ m/s , is required to induce separation and produce the lowest possible lift ($C_\mu = 0.8\%,\ C_l \approx 0.8$) . These steady results define the control authority and bracket the attainable setpoint attainable by ILC. In contrast to $\tau = 180°$ shown in Figure 29, the pitching moment excursions are only reduced by about one-half, although damping is always positive. Attaining constant M_{sp} would therefore likely pose a greater challenge, and because C_m is less sensitive to changes in C_μ than C_l , a substantial reduction in moment excursions may come at the price of large lift excursions.

Further evaluations of ILC were performed for the reduced pitchrate range $0.01 \le k \le 0.09$ and the dynamic setpoint $C_{l,\text{sp}}(\phi) = 2\pi(\bar{\alpha} + \Delta\alpha \sin\phi)$ (lift coefficient along the symmetric thin airfoil theoretical slope), and details on these cases, and additional information on the method and results, can be found in [21] and [81].

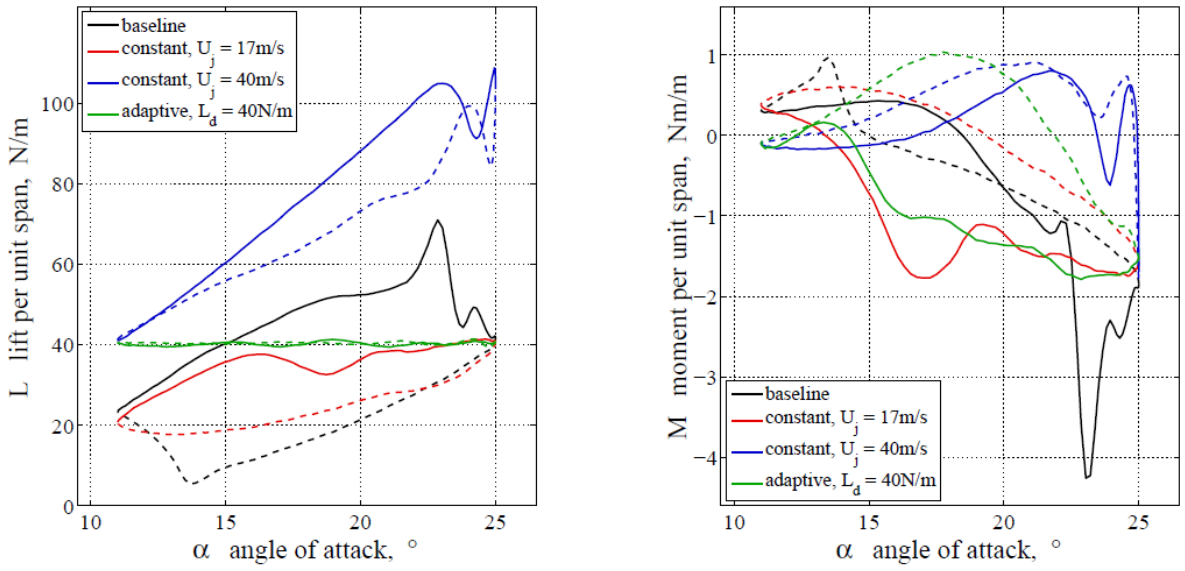

Figure 30. Phase-averaged dimensional aerodynamic loads under in-phase harmonic pitching and surging $\alpha(\phi) = 18° + 7° \sin\phi$ and $Re_c(\phi) = 3\times10^5[1 + 0.2\sin\phi]$ at $k_n = 0.06$, illustrating the results of ILC for lift control.

It is the opinion of this author that load control via leading-edge slot blowing is preferable to other mechanical, fluidic and plasma-based methods [195,196]. Mechanical methods, such as flaps, Gurney flaps (or micro-tabs), or trailing-edge morphing, may suffer from reliability problems, particularly under the harsh conditions experienced by HAWT blades. Moreover, the compensation for overloads typically occurs when angles-of-attack are high, where flaps are ineffective due to trailing edge separation (cf. the barn-door syndrome). A similar conclusion can be drawn with regard to trailing-edge blowing, based on the Coandă effect. Regarding high-frequency zero mass-flux blowing or DBD plasma actuation, as a general rule, these methods only increase loads by suppressing or eliminating dynamic stall, and cannot induce it. Hence, the absence of a load reduction mechanism renders them impractical. For field or ocean applications, load estimation by integrating surface pressures is not practical, although sensing based on current health-management systems, together with modeling the blade aeroelasticity, could by employed [197].

3.9 Closed-Loop Control

Closed-loop control approaches of dynamic stall depend to a large degree on the specific objectives and usually involve some form of lift or moment control. A limitation of leading-edge actuators that aim to control reduce or eliminate stall—but not induce dynamic stall as

described in [21]—is that they are only capable of increasing post-stall lift and minimum pitching moments. Thus the greatest lift-based control authority can only be achieved when the reference value is greater than the largest uncontrolled value [198], and this may suffice for many applications. For small air vehicles exposed to gusts, the main challenges involve the selection of a control architecture, the development of disturbance and plant models, the implementation of effective sensing, and the development of surrogate load measurements [199-203]. Below we describe simple on-off control, merely aimed at eliminating or reducing the negative effects of dynamic stall (section 3.9.1) and popular feedforward/feedback approaches for load control aimed at small air vehicles (3.9.2).

3.9.1 On-Off Control

The bandwidth of dynamic stall control depends on the aerodynamic response to disturbances and the response to actuation (see section 3.9.2). It is useful, therefore, to anticipate dynamic stall based on surrogate sensors, and then initiate actuation at, or just prior to, the onset of stall. This was achieved by [204] using discrete pulsed-jets, with sensing based on the large negative suction peak pressure peak near the leading-edge, together with an ad-hoc second-order model. A different approach is based on sensing upper surface pressure oscillation amplitudes near the leading-edge ($x/c = 8\%$) resulting from low-amplitude AC-DBD plasma leading-edge perturbations [206]. The perturbations are amplified at incipient stall, and when some bandpass filtered threshold is exceeded, the actuators switched to high-amplitude separation control mode. This method relies on the fact that DBD plasma actuators rely on an excitation mechanism—as opposed to direct forcing (see section 3.5.2)—and must exceed some threshold to effect control, while further increases in actuator amplitude have very little effect. An alternative method employed flush-mounted microphones close to the trailing edge on the upper surface of an airfoil [116]. Based on analysis of the acoustic signals using bandwidth-limited power spectral densities (PSDs) from multiple datasets and angles-of-attack, the increase in the total PSDs were correlated with flow separation.

It has long been known that pressure just below the leading-edge is very sensitive to changes in angle-of-attack, and measurement of the pressure is used as the basis of many stall-warning systems [207]. Most commonly, the low-pressure region draws air through a reed, producing an audible warning to the pilot. This stall warning sensor was adapted for dynamic stall control, by using zero pressure crossings to either initiate or terminate leading-edge pulsed-AC-DBD plasma perturbations, under both harmonic pitching and pitch-and-hold motions [22]. To evaluate efficacy, open-loop (continuously activated) and closed-loop control results were

compared; an example is shown for harmonic pitching at $\alpha = 15° + 5° \sin \omega t$, a $k = 0.01$ and 0.1, in Figure 31. Generally, the correspondence was excellent, and the small difference near the static stall angle during the pitch-up motion at $k = 0.01$ was related to the sensor (pressure port) location. At $k = 0.1$ (and $k = 0.05$, not shown), this difference disappeared due to the delayed response of the boundary layer separation. Although closed-loop pulsations are terminated at angles-of-attack that are larger than the static stall angle, (e.g., for $k = 0.1$), the lift and drag coefficients are virtually identical to those obtained with open-loop control. This is because separation occurs over approximately 10 convective time units $T_{sep} U_\infty / \bar{c} \approx 10$ [27], which is comparable to the downstroke ½-cycle i.e., $T_{1/2} U_\infty / \bar{c} = \pi / 2k = 16$, but the dimensionless time between termination and pressure zero-crossing is much smaller than that, namely 2.7. This time-scale disparity increases with increasing pitching frequency and therefore acts as a welcome built-in compensation as k increases.

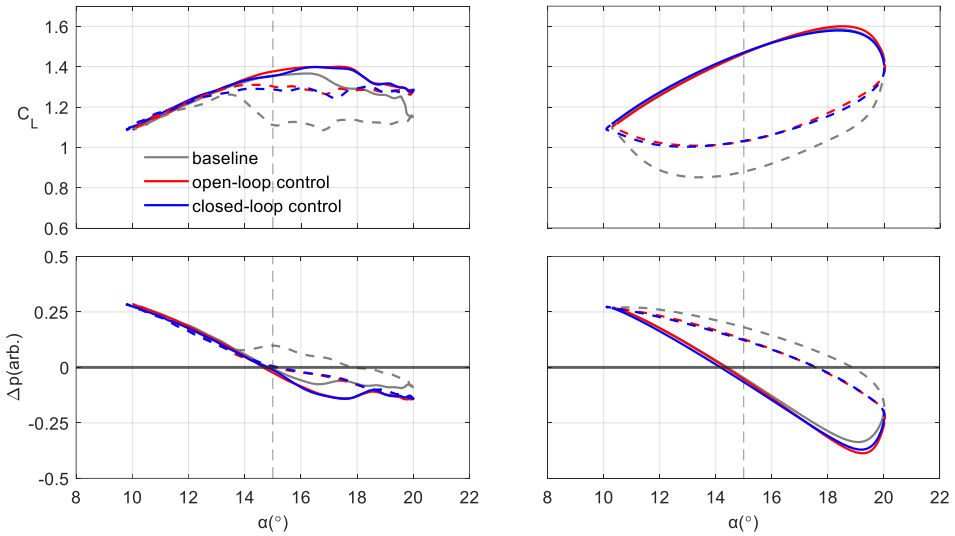

Figure 31. Phase-averaged baseline, open-loop and closed-loop aerodynamic coefficients and leading-edge pressure with $\bar{\alpha} = 15°$ at $k = 0.01$ (left) and $k = 0.1$ (right) [22].

3.9.2 Feed-Forward and Feedback Control

Simple on-off control described in section 3.9.1 tells us very little about the state of the flow or the loads on the vehicle, and thus feedforward models can be used to anticipate and counteract dynamic stall effects. Dynamic stall, however, produces large load amplitudes and phase-shifts that are often significantly different to classical theory [44,45], even at low angles-of-attack [51,65]. Owing to the fact that Navier-Stokes-based solutions are impractical for control schemes, empirical, semi-theoretical, data-driven, and ad-hoc models have been developed.

Many of these are described in [27,202,203,205], where their relative advantages and disadvantages are discussed.

A popular and widely-used model, that is easily integrated into closed-loop control schemes, is the Goman-Khrabrov (G-K) model [65], which is well-suited to finite wings and trailing-edge staller airfoils. It is a state-space model that employs the internal dynamic variable $X(t)$ to describe the vortex breakdown position, or separation point, while the output equation updates the desired aerodynamic coefficients, for example $C_L = C_L[\alpha, X(t)]$. The function X_0 nominally represents the static vortex breakdown or separation point location: no breakdown or fully attached flow, and apex breakdown or leading-edge separation are represented by $X_0 = 1$ and $X_0 = 0$, respectively. The model distinguishes between delayed effects that are proportional to $\dot{\alpha}$ and expressed by the argument shift $X_0(\alpha - \tau_2\dot{\alpha})$, and load variations not dependent on α that are described by a relaxation process, characterized by the time constant τ_1. Thus, the separation point (airfoil) or vortex breakdown position (delta wing) during dynamic pitching is described by:

$$\tau_1 \frac{dX}{dt} + X = X_0(\alpha - \tau_2\dot{\alpha}) \tag{26}$$

where the internal variable $X_0(\alpha)$ is determined from static $C_L = C_L(\alpha)$ data (or computation results) and the time-constants, τ_1 and τ_2 are commonly determined by least squares techniques from dynamic data. Equation (26) is sometimes referred to as a time-delay and decay (TDD) model and serves as a disturbance model in the context of feedback and feedforward control [27].

On pitching airfoils or small air vehicles subjected to gusts, a method is required to detect the gust, together with a controller to drive the actuators or actuation method. Although there are many schemes for achieving this [27], we will focus on the practical and popular feedforward/feedback control architecture (see Figure 32), whose objective is to maintain a constant (reference) lift force under large-scale disturbance inputs [198]. This architecture requires a disturbance model G_d for the unsteady aerodynamic gust response, and a plant model G_p that describes the system response to actuation. This approach implicitly assumes that the two models G_d and G_p are independent of one another and are linearly superposable to obtain a net output response, i.e., $y = y_p + y_d$. With G_d and G_p identified, both the feedforward and feedback controllers K_d and K can be designed.

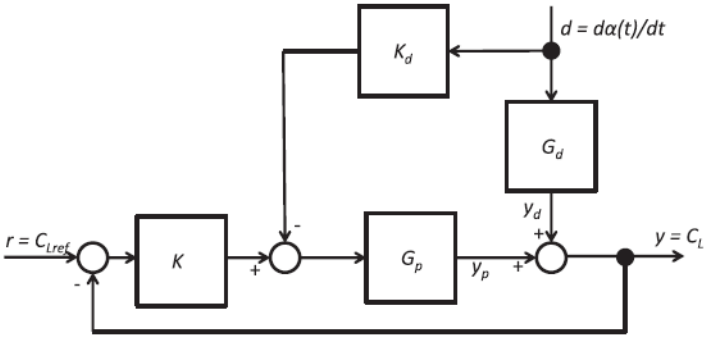

Figure 32. Block diagram of a commonly-used feedforward/feedback control architecture for gust alleviation [198,27].

Pure feedforward control was demonstrated using leading-edge slot blowing, described in sections 3.5.1 and 3.8, by neglecting the lower feedback loop in Figure 32 [208]. The original TDD mode shown in equation (26), was modified to include the effect of steady blowing, to either suppress or promote dynamic stall, in the form:

$$\tau_1 \frac{dX}{dt} + X = X_0(\alpha - \tau_2 \dot{\alpha}, C_\mu) \tag{27}$$

where the lift coefficient was expressed as:

$$C_l = f(\alpha, C_\mu) X(t) + g(\alpha, C_\mu)[1 - X(t)] \tag{28}$$

and the unknown functions were determined from data associated with pre-stall and post-stall regions, namely:

$$f = \left.\frac{\partial C_l}{\partial \alpha}\right|_{\text{pre}} \alpha + \frac{\partial C_l}{\partial C_\mu} C_\mu + \frac{\partial^2 C_l}{\partial \alpha \, \partial C_\mu} \alpha C_\mu \tag{29}$$

and

$$g = \left.\frac{\partial C_l}{\partial \alpha}\right|_{\text{post}} (\alpha - \alpha_s) \tag{30}$$

respectively. Similarly, a TDD (plant) model was developed for the effect of low-frequency periodic blowing—based on the high-frequency form of [209]—on the lift coefficient, namely:

$$\tau_3 \frac{dY}{dt} + Y = Y_0[C_\mu(t - \tau_4)] \tag{31}$$

where

$$Y_0 = \frac{\Delta C_l}{\Delta C_{l,\max}} \tag{32}$$

The controller used a linearized version of this model for the inverted plant model, and simulations showed large (factor of 10) reductions in lift oscillations, consistent with the ILC results described in section 3.8.

Of the many feedback techniques developed [27], we present two examples based on the architecture shown in Figure 32, namely: a semicircular wing with pulsed-blowing actuators subjected to random wind gusts [198]; and a NACA 0009 airfoil at $Re_c = 57,000$ with synthetic jet actuation at $x/c = 7.3\%$ undergoing rapid pitching maneuvers [210]. For the semicircular wing, the lift response to longitudinal velocity perturbations, at anticipated frequencies, was measured, and the cross spectrum was used to identify the disturbance model. System identification was used to measure and correlate the system's lift response to pseudorandom binary signal steps for the plant model [198]. For the airfoil a linearized version of the G-K (TDD) model was used for the disturbance model. The feedforward controllers K_d were constructed from the disturbance models, inverted delay-free plant models $\tilde{G}_p^{-1}$ and a low-pass filters, expressed as $K_d = G_d \tilde{G}_p^{-1} G_f$.

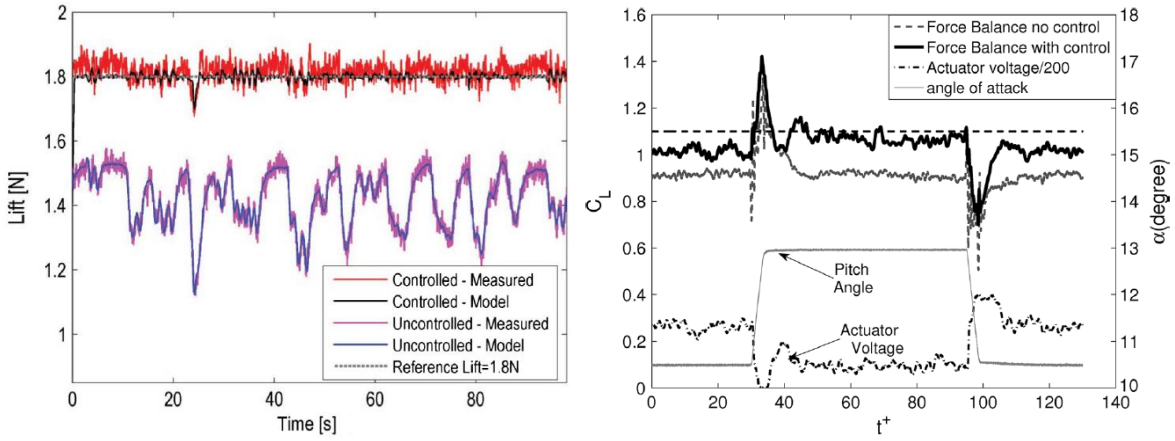

Figure 33. Closed-loop gust-alleviation control for: (right) a semi-circular wing subjected to longitudinal velocity oscillations [198]; and (left) a NACA 0009 airfoil subjected to pitch-up and pitch-down motion [210]. Images republished with permission.

The wing was subjected to wind gusts in the form of pseudorandom velocity variations, and the controller is commanded to maintain a constant reference lift, above the maximum uncontrolled value (Figure 33, left). Phase averaged uncontrolled and controlled experimental data are shown together with simulation results, that used the measured velocity variations as input to the disturbance model. The controlled lift approximates the reference, and the peak-to-

peak oscillations reduce by a factor of more than two. The close correspondence between simulation and data indicates that the nonlinear unsteady aerodynamics associated with longitudinal wind gusts are adequately represented by the linear models, and that linear superposition of the response to predicted plan and disturbance lift is suitable for practical controllers.

For the airfoil, the controller is commanded to maintain $C_l = 1.05$ for a rapid pitch-up and pitch-down at $\kappa \equiv \dot{\alpha} c / U_\infty = 0.0143$ between $\alpha = 10°$ and 13° (Figure 33, right). The steady-state lift coefficient without control is nearly independent of α, but exhibits an overshoot and an undershoot during pitch-up and pitch-down motions respectively. The overshoot most likely results from a DSV and the undershoot is produced by a LEV that forms during the downstroke and then produces a high-pressure non-circulatory on the upper surface [22,26]. Actuation terminates during the pitch-up and this may be a limitation of the controller amplitude because generally high-frequency perturbations can eliminate the DSV [138]. During pitch-down, the controller attempts to compensate for the undershoot but the relative change in C_l does not vary considerably. Similar observations were made on a larger aspect ratio wing [22]. The physical mechanisms associated with attachment under rapid pitch-down motion must be better understood in order to develop effective controllers.

3.10 Flapping Wing Flyers

The design of flapping-wing flyers is based heavily on the analysis of biological flyers, i.e., insects, birds and bats, that has been elucidated by biologists during the last few decades [68,211-217]. The study of biological flyers is complicated by the large variations in wing morphology, e.g., planform shape, thickness, aspect ratio, wing loading; wing kinematics, as well as flapping amplitudes and frequencies; and—for birds—feather arrangement [213]. Insect wings commonly have low aspect ratios and thin-plate-type sections; bird wings can be characterized to some degree by airfoil sections characteristics, like mean camber and thickness distribution; while bat wings are membranous, with multi-joint bone structures [72]. Propulsive flight [13]—typically of birds and insects—and hovering flight [72]—typically of insects and hummingbirds—are two fundamentally different problems, and the objectives of dynamic stall control differ accordingly.

Comprehensive and detailed treatises of flapping wing flight are presented in the references above. In the discussions below, we only consider leading factors affecting dynamic stall and its control. Moreover, we ignore aeroelasticity [68] and wing morphing effects [213],

for the sake of simplicity. We will also divide our discussions below into propulsive ornithopters flight, that traverse the NAV-MAV range, and hovering flight generally associated with NAVs.

3.10.1 Propulsive Flight

In propulsive flight, the flapping motion produces an effective angle-of-attack that results in both propulsive and lift force components [13], as shown in Figure 34 (left). When some critical frequency is exceeded, the drag forces are overcome and a propulsive thrust $\bar{T}$ is produced, which is associated with reverse Kármán vortex street. A characteristic Strouhal number is defined as:

$$St_{\text{pf}} \equiv \frac{f_f A_w}{\bar{V}} \tag{33}$$

where f_f is the flapping frequency, and A_w is wake width. We introduce the subscript "pf—propulsive flight" to distinguish it from hovering flight and from the conventional Strouhal number St based on the body's streamwise projected height, e.g. diameter d in the case of a circular cylinder, or $\bar{c}\sin\alpha$ for an airfoil or finite wing. A reduced flapping frequency, similar to that for pitching airfoils, is also introduced, namely $k_f \equiv \pi f_f c / U_\infty$. The utility of the characteristic Strouhal number, shown in (33), was illustrated by [218], who determined that propulsive efficiency $\eta_{\text{pf}} \equiv \bar{V}\bar{T} / \bar{P}$ is maximized when $0.2 \le St_{\text{pf}} \le 0.4$.

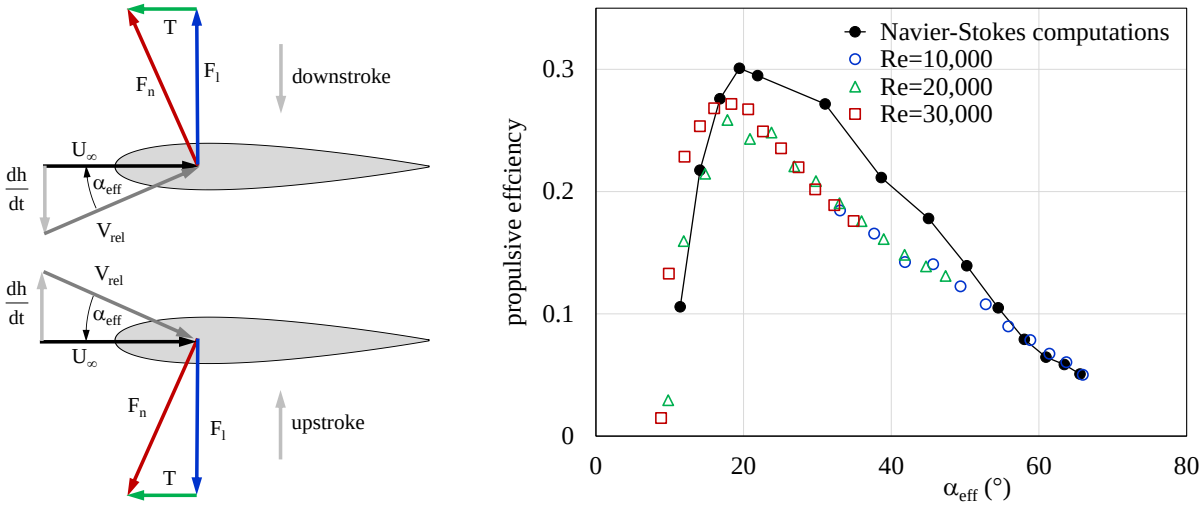

Figure 34. Left: Schematics illustrating the generation of lift and thrust developed by a flapping wing (adapted from [13]). Right: Propulsive efficiency as a function of the peak effective angle-of-attack $\alpha_{\text{eff}} = \tan^{-1}(2k_f h_0 / c)$, adapted from [13,219].

The wake width is not easily measurable, and it is convenient to use surrogates, like the peak-to-peak flapping amplitude A_f, which can be approximated as $b\sin(\hat{\theta}/2)$, or the plunge amplitude h_0 ($\hat{\theta}$ is the dorsoventral stroke angle, see section 3.10.2). Propulsive flight studies consider either plunging motion [(equation (15)], or pitching-and-plunging motion [combinations of equation (1) and equation (15) with a suitable phase-difference] of airfoils and finite wings as shown in Figure 34. From the above definitions, we can therefore distil the parameter [13]:

$$k_f \frac{h_0}{c} \equiv 2\pi \frac{h_0}{A_f} St_{\text{pf}} \tag{34}$$

where $h_0 / A_f = 1/2$ for pure two-dimensional plunging motion, $h_f / A_f \approx 1/4$ for pivoted flapping motion, and the maximum effective angle-of-attack $\alpha_{\text{eff}} = \tan^{-1}(k_f h_0 / c)$ [13]. During propulsive flight, effective angles-of-attack are typically below or close to the static stall angle. Of greatest importance from a dynamic stall control viewpoint, is that the maximum thrust and peak propulsive efficiency occur at Strouhal numbers close to the dynamic stall boundary, that is characterized by the formation of LEVs (see Figure 34). It can be seen that peak efficiency occurs at $k_f h_0 / c \approx 0.35$, corresponding to $\alpha_{\text{eff}} \approx 19°$, which is clearly greater than the static stall angle α_s. This should be contrasted with cruising flight that attains maximum propulsive efficiency (range) at maximum aerodynamic efficiency $(C_L / C_D)_{\max}$. Without an external passive or active flow control agent, peak flapping propulsive efficiency can be achieved by a judicious combination of angle, amplitude, and frequency. For example, for a given Strouhal number, the LEVs associated with dynamic stall are minimized by a combination of high k_f and low h_{f0} / c, as opposed to low k_f and high h_{f0} / c [220]. This represents a natural form of dynamic stall control by design.

Bird feathers don't only constitute the aerodynamic surface that is responsible for lift and thrust generation. They also act as flow control devices by deforming (or morphing) and are used to delay dynamic stall. For example, the alula—which is small group of moveable feathers attached to the bird's "thumb"—functions as a high lift device; either like a slat, a streamwise vortex generator, or a spanwise vortex generator that suppresses dynamic stall at high angles-of-attack during landing and maneuvering [213]. Also, during landing and flight in high levels of turbulence, the covering feathers on the upper side aft part of the wing tend to "pop up," thereby reducing dynamic stall effects [121]. The wings of ornithopters, generally

speaking, are not constructed from feather type material, and surrogates can be used. Leading-edge active flow control—for example, using DBD plasma actuators, or actively deployed VGs—can act as surrogates for the alula, while passively operated upper surface "pop-up" flaps can easily be added to existing wings. DBD plasma actuators can also be configured to operate on both, or alternating, sides by switching the actuation direction [221]. The dynamic stall pitch-plunge equivalence discussed in section 3.6.2, suggests that positive results obtained from leading-edge DBD plasma actuators on pitching airfoils, can increase propulsive efficiency. This approach is particularly advantageous at lower flight Reynolds numbers $(Re < 10^5)$, where only very small power requirements (i.e., several mW/cm) are required for significant aerodynamic benefits [222].

3.10.2 Hovering Flight

Hovering flight kinematics is defined with respect to a stroke-plane β by three primary rotation (or oscillation) angles, namely: (i) that within the stroke-plane, denoted $\hat{\phi}$; (ii) that relative to the stroke plane, i.e., the angle-of-attack α; and (iii) that normal to the stroke-plane, also called the dorsoventral angle $\hat{\theta}$. The angle-of-attack switches sign twice within a pitching cycle, to ensure positive lift generation during the upstroke and downstroke (forward-and-aft) phases. A vast body of literature exists, based on the research of biologists, scientists and engineers, that addresses aerodynamic modeling and computation, flight dynamics, stability, and control [69,72,73,211-213-220,223-230]. Various types of wing kinematics have been identified, including "clap and fling," "rapid pitch rotation," and "wake capture," to explain the mechanisms of lift generation [68]. Irrespective, the dominant unsteady aerodynamic mechanism of lift generation is the leading-edge vortex (LEV), and its interaction with the wingtip vortex (TV) [72]. Regardless of wing morphology, wing kinematics produce unsteady vortex-dominated flows and the problem can therefore be simplified and viewed as an optimization exercise in unsteady separated flow—or dynamic stall—control. In this respect, the wings themselves are the "mechanical actuators" that generate and manipulate the vortical structures. In the arguments below, we will show that a unique relationship exists between Strouhal numbers associated with insect flight, leading-edge forcing on flat-plate plate airfoils and low aspect-ratio flat wings, and vortex shedding.

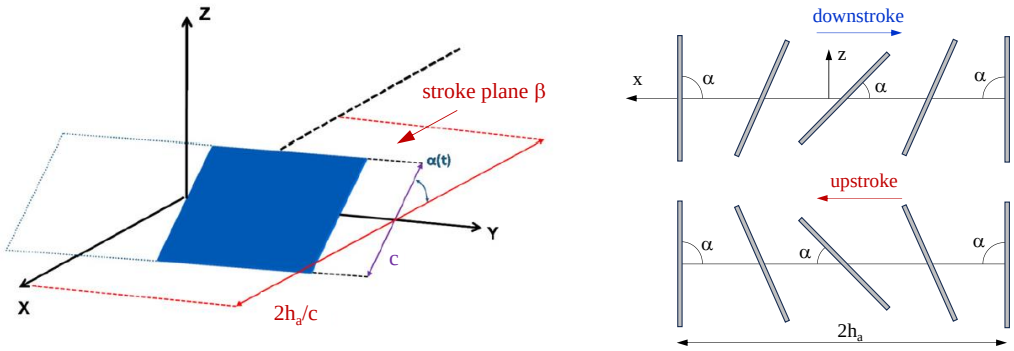

Figure 35. Left. Schematic of the simplified coordinate system for wing kinematics, identifying the stroke-plane β, and angle-of-attack α based on a rectangular wing planform. The linear non-dimensional stroke-plane amplitude $2h_a/c$ is taken as a surrogate for the rotational tip displacement $R\Phi$ [68]. Right. Idealized depiction of wing kinematics in the normal hovering mode [69].

For optimization studies it is useful to again consider scaling laws, in the form of dimensionless parameters, together with the simplified geometry [68] and wing kinematics [69] shown in Figure 35. Here, we will neglect parameters associated with fluid-structure interaction, described in [68] for the purposes of a simplified analysis. For hovering flight, we define the Strouhal number:

$$St_{\text{hf}} \equiv \frac{f_f(2h_a)}{\bar{V}_{\text{tip}}} \tag{35}$$

based on the stroke amplitude h_a, which generally follows a surging-type motion, and must be distinguished from pure plunging amplitude. It is common practice to adopt an average tip speed based on assumed harmonic motion, namely $\bar{V}_{\text{tip}} = 2f_f\Phi R$, where Φ is the full-stroke (peak-to-peak) flapping amplitude, and R is the wing semi-span. Thus, the Strouhal number based on the average wing-tip velocity is simply:

$$St_{\text{hf}} \equiv \frac{h_a}{\Phi R} \approx \frac{1}{2} \tag{36}$$

The relationship between the insect-Strouhal number in hover and the traditional vortex-shedding shedding Strouhal number, therefore, is:

$$St \equiv \frac{f_f \bar{c}\sin\alpha}{\bar{V}_{\text{tip}}} = St_{\text{hf}}\frac{\bar{c}\sin\alpha}{2h_a} \tag{37}$$

under the assumption that the shedding and flapping frequencies are one-and-the-same. Using $\bar{c}/2h_a$ data for small (e.g. gnats, mosquitos and fruit flies [224-226]), intermediate (e.g.,

honeybee [227,228]) and large (e.g. Hawkmoths and Cicadas [228,229]) flying insects, as well as for hummingbirds [230], this Strouhal number falls in the range $0.07 \le St \le 0.16$. It is of more than passing interest that the midpoint of these limits is approximately equal to one half of the conventional vortex shedding Strouhal number of ~0.21. The relatively small bracket observed here shows that the Reynolds number, which spans the range $O(10^2)$ to $O(10^4)$, is not a leading parameter. This is likely due to the fact that the separation line is fixed at the leading-edges, due to the thin wing, and the resulting unsteady, massively separated, turbulent, vortical flow is not subject to Reynolds number effects commonly associated with attached boundary layers.

It is also useful to compare this Strouhal number range with that introduced by leading-edge forcing—in this case, using DBD plasma actuators—where the forcing Strouhal number is rendered as:

$$St^+ \equiv F^+ \sin\alpha = \frac{f_p c}{U_\infty} \sin\alpha \tag{38}$$

for comparison. Figure 36 shows the dependence of lift coefficient on F^+ and St^+ for both flat-plate two-dimensional airfoils and a rectangular flat plate wing of $AR_R \equiv R/c = 1.27$, where the grey shaded region is the flapping wing range estimated above [231-233]. This figure reveals, surprisingly, that the optimum Strouhal number range for forcing is not dependent on aspect ratio, at least in the range $AR_R = 1.27$ to ∞. Equally important, the Strouhal number range that produces the maximum increases in lift coefficient using active flow control, corresponds well with the optimum Strouhal number range for hovering flight.

The above observations serve as a strong basis for linking the hovering flight of flapping wing flyers, conventional vortex shedding, and active flow control, to a universal Strouhal number.

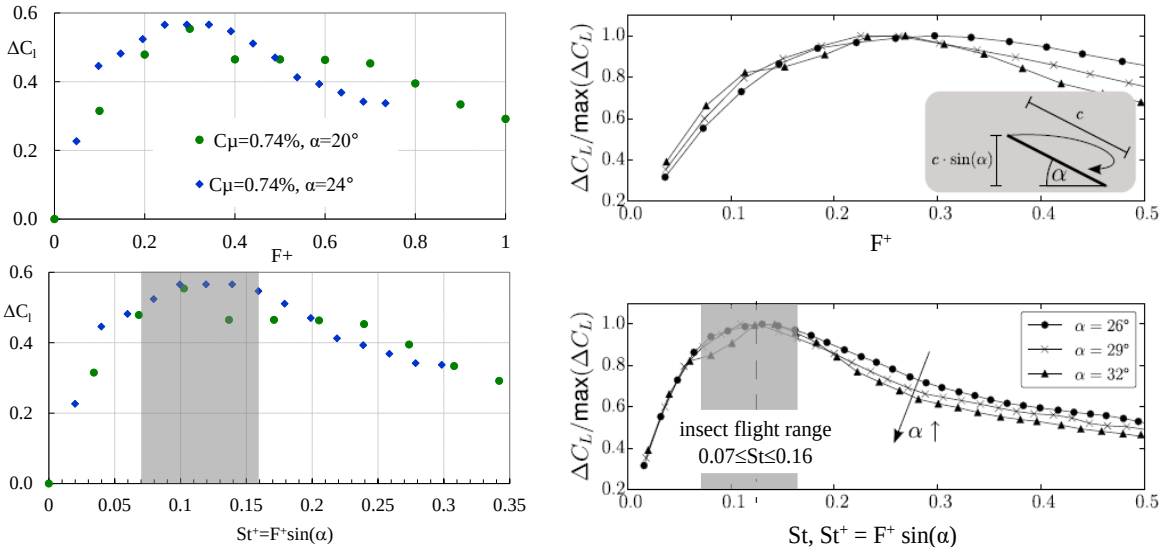

Figure 36. Normalized change in lift on a flat-plate airfoil (left) and a flat semi-span wing (right) ($AR_R = 1.27$) with pulse-modulated leading-edge AC-DBD plasma actuation on the basis of reduced frequency (top) and Strouhal number (bottom) for $3{,}000 \le Re \le 20{,}000$. Strouhal number range corresponding to hovering insect flight show as the shaded region.

3.11 Computational Predictions

This section is not intended as review on different numerical schemes; rather it is an attempt to identify where the current state-of-the-art stands in terms of validated predictive capability, i.e., based on comparison to experiments. Computational approaches depend to a large extent on the particular problem as well as on the corresponding Reynolds number range. For example, at small MAV or NAV scales typical of insect flight ($10^2 \le Re \le 10^4$), where the wings themselves are the vortex-generating actuators (see section 2.4), direct numerical simulations are performed [234], that can account for morphology, i.e., the external form and structure of the body and wings, as well as realistic wing-body kinematics. Mean lift computations based on the average loads generated over a complete beat (or flapping) cycle, correspond well with the weights of hawkmoths, honeybees, and fruitflies. For ornithopters and conventional MAVs, at $Re = O(10^5)$, it is likely that direct numerical simulations are still not feasible for routine computations [235].

At higher Reynolds number associated with wind turbines, helicopters and fixed wing applications ($10^5 \le Re \le 10^7$), computational methods for dynamic stall control face the dual challenge of accurately modelling both the unsteady dynamic stall process as well as the actuator's effect on the flowfield and loads. (In the context of closed-loop control, these are often referred to as the plant and disturbance models, respectively, see section 3.9.2). In

principle, numerical methods used for dynamic stall predictions on airfoils, fixed-wings and rotors can be adapted, or modified, for dynamic stall control.

The three most common approaches are Unsteady Reynolds-Averaged Navier-Stokes (URANS) model equations [18,236], Large Eddy Simulations (LES) [237,238] or some hybrid combination of the two [236,239,240]—for example, Detached Eddy Simulation (DES) proposed by [241], and its variants. The selection is usually based on desired degree of fidelity and available computational resources. LES and DES are both scale-resolving approaches whereas URANS only predicts mean flow patterns. Nevertheless, URANS is still a common choice, mainly because computation time is reduced by several orders of magnitude compared to LES, but its imposed phase-averaging filters out essential flow details, natural and LSB transition are not accurately modelled [242], and model constants are generally tuned for steady attached flows [243]. Despite these limitations, some predictions are reasonable [18,236], and can perhaps be used for initial design approximations. In the absence of a control input, hybrid RANS-LES approaches, like Delayed Detached Eddy Simulations (DDES) [202], generally capture separated dynamic stall phenomena more accurately than URANS

3.11.1 Passive Devices

As was pointed out in section 3.3, VGs are the most popular passive flow control devices. URANS models the effects in a mean sense (i.e., a RANS sense) or it can capture the streamwise vortex structures to some degree [244,245]. LES, on the other hand, attempts to resolve the instantaneous formation and development of streamwise vortices, as well as their downstream interaction, but at significantly increased computational cost compared to RANS [246,247]. Under dynamic stall conditions, variable-droop leading-edge computations [248] and combined VG-variable-droop computations [248,249] using URANS shows that the LEV can be eliminated, potentially making the use of URANS more viable. To date, however, computational validations against experimental data for VGs or drooped leading-edges do not appear to have been performed. Recently, it was shown computationally, that periodic disturbances can be generated, and exploited to excite the the LSB, by means of a two-dimensional cavity just below the leading-edge, that produces Rossiter Modes [250]. Vortices shed from the upstream edge impinge on the downstream edge producing acoustic waves, that travel upstream and excite the shear layer. The desired frequency of these self-sustained oscillations is determined by the cavity dimensions.

3.11.2 Steady and Unsteady Momentum Addition

The most common active methods are steady and unsteady momentum flux (e.g., steady slot blowing and zero or non-zero mass-flux methods) and DBD plasma actuators (e.g., AC-DBD and pulsed-DC). Active flow control methods involving steady momentum flux are reasonably straightforward to implement computationally by suitable modifications of the geometry and/or boundary conditions [251,252]. URANS is capable of qualitatively predicting the effects of both low- and high-momentum steady slot blowing under static conditions [242,253]; LES, on the other hand, provides both details of the instantaneous large-scale flow dynamics and improved correspondence with experimental data [253]. Even though several steady momentum addition URANS and LES dynamic stall control computational studies have been performed [254], none appears to consider validation against experimental data. URANS predictions of unsteady momentum flux addition, i.e., zero mass flux (synthetic jet) actuation forcing, under static conditions, produces qualitative correspondence with data [251,255,256]. However, even with fully turbulent upstream boundary conditions [257], URANS predictions of synthetic-jet separation control reflect only qualitative trends [258]. For both steady and unsteady leading-edge momentum addition, there is clearly a need for detailed validation against experimental data.

3.11.3 DBD Plasma Actuators

Modelling of DBD plasma actuators is typically performed by off-line simplified physical models and subsequently introduced into computations as a volumetric body force. AC-DBD are modelled by solving the Laplace equation for the electric field resulting from the applied AC electrode voltages and the Poisson equation for the charge density of the ionized air [259]. Alternatively, electro-static and lumped-element circuit models can be used to provide the time-dependent charge distribution [260,261]. For nanosecond pulsed-DC actuation, semi-theoretical modes are generally employed. The model of [262] is based on a power density distribution, which is proportional to the gas heating energy divided by the characteristic heating time. The gas heating energy is modeled as a product of energy input and energy efficiency, while the spatial distribution is obtained by through curve fitting of the emission intensity. The model of [263] describes near-wall electric field strengths relative to the actuator, together with electron and ion densities, and plasma layer thickness parameters.

The implementation of the model described by [261] in URANS schemes produced reasonable agreement with static separation control, both at the leading-edge of an airfoil as well as that with a fully turbulent inflow [260]. However, validation of DBD plasma actuators

under dynamic stall does not appear to have been attempted. Small-amplitude perturbations have been used as an AC-DBD plasma surrogate. This was done using high-fidelity wall-resolved LES with high-frequency perturbations [$F^+ = \mathcal{O}(10^2)$] at the leading-edge NACA 0012 airfoil under dynamic pitching [151]. A follow-up study was performed using the same profile and perturbation method on a finite wing of $AR = 4$ [86]. In both instances, the small perturbations introduced at the leading-edge were amplified by the LSB, and this inhibited bubble bursting, i.e., the development and shedding of the LEV. The excitation mechanism can be considered to act in a quasi-steady manner on the time-varying flowfield due to the large disparity between the excitation and pitching time-scales, namely $\pi F^+ / k = 800 \gg 1$ (see section 3.4.2). The finite wing computational results at $F^+ = 50$ were consistent with similar dynamic stall control experimental data [87], but with a different airfoil shape (NACA 0015) and $AR = 1$.

A common theme running through passive and active dynamic stall control, is that direct validation against experimental data is sorely lacking, even for idealized nominally two-dimensional harmonic pitching problems. This obviously neglects additional parameters relevant to helicopter blades, like unsteady sweep and compressibility, discussed in section 6. Much like cases without control [202], Hybrid RANS-LES turbulence models are likely the best option for dynamic stall control computations.

4 Compressible Flows

The main driver of compressible dynamic stall research is retreating blade stall (RBS) on conventional helicopters rotors, and comprehensive reviews are presented in [1,8,16,19,20]. Although high subsonic Mach numbers ($M < 1$) [264,265] are experienced on the advancing blades, RBS typically occurs in the range $0.3 \le M \le 0.6$ [19]. While maximum lift coefficients increase almost linearly with pitchrate, the lift overshoot decreases with Mach number, becoming negligible at $M \approx 0.6$ [19,266]. This transonic regime is different to the conventional "cruise problem" on fixed wing aircraft, where relatively large chordwise regions of supercritical flow are present on both surfaces at low angles-of-attack [16]. During dynamic pitch-up into the post-stall regime, a relatively small supercritical region forms downstream of the leading-edge, and with increasing Mach number a shock wave initiates dynamic stall; this is the meaning of shock-induced dynamic stall [19]. It is fundamentally different from incompressible leading-edge stall bubble bursting and is not characterized by shedding of an LEV, although pitch-down divergence occurs at a lower angle-of-attack [19]. Supercritical flow and shock-strength depend upon a combination of Mach number, pitchrate and maximum angle-of-attack. For example, the combination $k = 0.1$ and $\alpha = 15° + 10° \sin \omega t$, can produce supercritical flow on airfoils at $M \approx 0.2$.

The focus of all effective passive or active control techniques is the elimination or weakening of shock-induced separation. Techniques investigated experimentally are summarized in Table 2, and include deformable and drooping leading-edges [267,268], slats [269], combined leading-edge extension and VGs [29], steady and pulsed micro-jet blowing [135,270-142] and combustion-based actuation [134].

4.1 Leading-Edge Geometry and Vortex Generators

Variation of the leading-edge geometry, via leading-edge droop, lowers the local peak Mach number and therefore the shock strength, thereby eliminating or weakening shock-induced separation [267,267]. This motivated for the study of a "variable droop leading edge" [268] which observed a weaker LEV, consistent with a 50% smaller negative peak pitching-moment coefficient and a 75% drag reduction. An effect similar to droop was investigated using a leading-edge extension (or "glove"), combined with VGs at 10% or 30% of chord [29]. The VGs generally tended to increase $C_{m,\min}$ for all reduced frequencies, except $k = 0.1$, and when combined with the glove, effective light dynamic stall control was achieved up to $M \approx 0.4$. However, the extension reduced $(C_l / C_d)_{\max}$ and the zero-lift drag divergence occurred at lower

Mach numbers, prompting [29] to recommend the glove for $r/R < 0.8$. Aerodynamically, a compelling case can be made for periodic leading-edge modification (or morphing [272]), combined with actively deployed VGs [114,115] (see section 3.4), within the azimuth cycle, although technologically this may not be viable at present.

Table 2. Dynamic stall control on airfoils under nominally compressible conditions ($M \geq 0.3$), and harmonic pitching: $\alpha = \alpha_0 + \alpha_1 \sin \omega t$.

reference	method	airfoil	α_0 / α_1 (°)	k	M	$\Delta C_{l,\max}$	$\Delta C_{m,\min}$	main observations
[267]	dynamically deformable LE	NACA 0012	10/10	0.05	0.3	—	—	elimination of the LEV
[267,269]	leading-edge slat	RC(6)-08	10/10	0.05	0.4	—	—	effective in suppressing DS; not suitable to advancing blade
[268]	dynamically drooping LE	VR-12	10/10	0.1	0.3 0.4	~ –0.3 ~ –0.25	~ 0.12 ~ 0.16	LEV strength significantly reduced
[29]	leading-edge modification + VGs	VR-7	10/10	0.025-0.1	0.3	0.3 to 0.15	0.08 to –0.4	positive effect weakens with k increases
		VR-7	10/5	0.05-0.1	0.4	—	~0.1	Combined leading edge modification and VGs alleviated pitching moments, but not independently
		VR-7	8/10	0.1	0.4	–0.1	~0	
[142])	pulsed blowing from orifices at 10% chord	OA209	13/4	0.1	0.3	~0	0.19	Suppression of light stall with constant blowing. Amelioration of deep stall steady and pulsed blowing effects comparable
			13/7	0.1	0.3	~0	0.10	
			11/7	0.06	0.5	~0	0.07	
[135]	leading-edge micro-jet blowing	NACA 0015	10/10	0.05-0.1	0.3,0.4	—	—	LEV eliminated by "release of vorticity," elimination of the shock
[134]	combustion powered actuation	VR-12	10/10	0.07 0.07	0.3 0.4	0.2 ~0	0.05 —	cycle-averaged lift coefficient increases by 11% at Mach 0.4.

4.2 Steady and Unsteady Momentum Flux

Zero and non-zero mass flux techniques, observed to be effective under incompressible conditions, also show potential in compressible flows. To date, zero mass-flux has not been successful in eliminating moment stall, due to the installation of the slot too far downstream [271].

Of all of the active momentum flux methods, surface jet or surface micro-jet blowing, either steady or pulsed, downstream of the leading-edge has shown potential for alleviating dynamic stall under compressible conditions [135,142]. Microjets, either normal to the surface or angled, are known to alleviate shock boundary layer interaction, where mass flowrate is a leading control authority parameter [266]. The jets act like small or micro VGs, forming horseshoe vortices and downstream counter-rotating vortex pairs between the jet and the external stream [273-275]. Sample data for $M = 0.3$ and 0.5 are shown in Figure 37, for light stall under steady blowing, high-frequency blowing ($F^+ = 0.99$) and scheduled control, i.e., blowing initiated and terminated within the pitching cycle (1/rev) [142]. At $M = 0.3$, both steady and high-frequency blowing effectively eliminate moment stall; the latter produces

slightly smaller lift hysteresis but a slightly greater pitch-down moment, and under deep stall (not shown) negative pitch-down moments are also significantly reduced. The likely reason that high-frequency forcing does not significantly affect results, but degrades at lower F^+ (not shown), is because it does not rely on an excitation mechanism to control dynamic stall (see section 3.5.2). Notably, at $M = 0.5$, steady blowing also significantly reduces pitch-down movements under moderate and deep stall. Scheduled control further increases $C_{l,\max}$ but with a smaller increase in $C_{l,\min}$, where these differences were most likely due to fluctuations in the supply line pressure when operated in an unsteady manner. Blowing delays the shock formation, moving it closer to the leading-edge and the stall mechanism changes from shock-induced to trailing-edge (not shown). These data are consistent with point diffraction interferometry measurements [135] that show the elimination of flow separation, accompanied by a thicker boundary layer due to the generation of multiple streamwise vortex pairs. At $M = 0.4$, interferometry measurements indicate that the unsteady periodic λ-shock structures appear downstream of the leading-edge. Blowing eliminates these shock structures and produces a boundary layer significantly thicker than that observed at $M = 0.3$ cases. These observations are again consistent with load measurements made by [142], that show relatively large increases in $C_{m,\min}$ at $M = 0.5$.

To summarize, microjet blowing is effective for dynamic stall control and has two main advantages: the orifices do not materially modify the blade geometry; and blowing can be initiated on-demand, within the rotor cycle, using on-off control (see section 3.9.1), for example. It can therefore potentially be employed in a close-loop control scheme, that initiates blowing at incipient stall. Two technological challenges to be considered are the physical supply of compressed air into the rotating blades, and estimation of the net gains when using engine bleed or an auxiliary air pressure source.

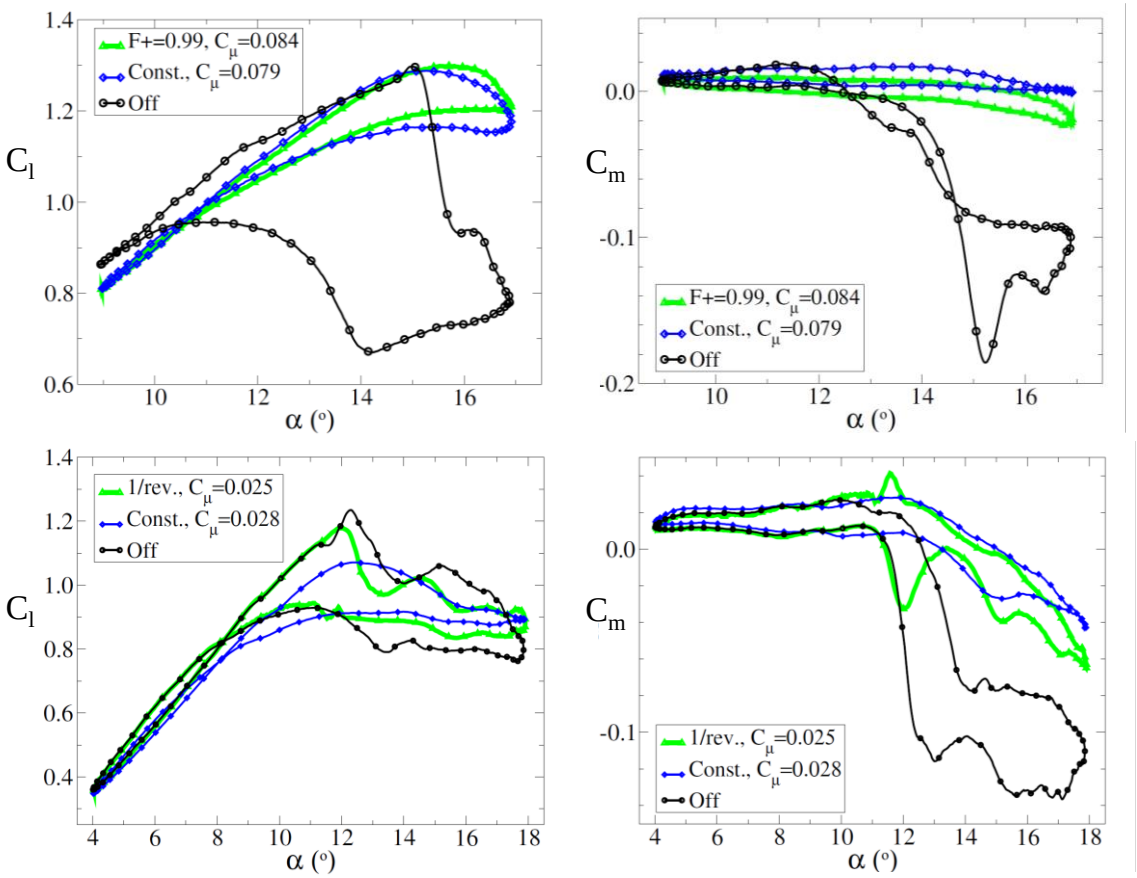

Figure 37. Representative results of compressible dynamic stall control by means of upper surface discrete jet blowing. Top row: $M = 0.3$, $\alpha = 13° + 4° \sin \omega t$, and $Re = 0.53 \times 10^6$, and at $k = 0.1$. Bottom row: $M = 0.5$, $\alpha = 11° + 7° \sin \omega t$, and $Re = 0.53 \times 10^6$, and at $k = 0.06$ [142]. Republished with permission.

4.3 Excitation-Based Actuation

To date, no convincing experimental demonstrations of excitation-based dynamic stall control have been performed for $M \geq 0.3$. However, static experiments performed with DBD plasma actuators [276,277]—both AC and nanosecond pulsed-DC—and hover results with nanosecond pulsed-DC at $M_{tip} = 0.3$ [278] suggest that beneficial performance results can be obtained. Technically, the actuators must be designed to produce sufficient perturbation amplitudes and frequency bandwidths, because increases in the relative velocity means that the excitation perturbation amplitude and frequency must increase accordingly. Sufficient amplitudes can be provided by nanosecond pulsed-DC actuators or high-voltage AC-DBD actuators. For example, using nanosecond pulsed-DC actuation at $F^+ \approx 5$, [276] observed a small pressure rise aft of the shock on a Lockheed-Georgia C-141 airfoil at $M = 0.74$. Kelley et al [277] studied the

effects of both AC-DBD and nanosecond pulsed-DC leading-edge actuation on the aerodynamic coefficients of a NASA Advanced EET airfoil in the Mach and Reynolds number ranges $0.1 \le M \le 0.4$ and $0.58\times10^6 \le Re_c \le 2.3\times10^6$ (see Figure 37). The baseline $C_{l,\max}$ under incompressible conditions increases with Re, but compressibility effects neutralize the gains for $M \ge 0.3$. Note that data is presented for both pulse-modulated and non-modulated actuation—sometimes referred to as "steady"—and because the freestream velocity changes, the non-modulated reduced frequency falls in the range $20 \ge F^+ \ge 5$ (2.3 kHz) with increasing Mach number. Overall, the effect of excitation on $C_{l,\max}$ and post-stall C_l weakens in non-dimensional terms, but not as significantly in percentage terms. The all-important C_m divergence does not show monotonic behavior but is delayed by approximately 3 degrees for both $M = 0.3$ and 0.4.

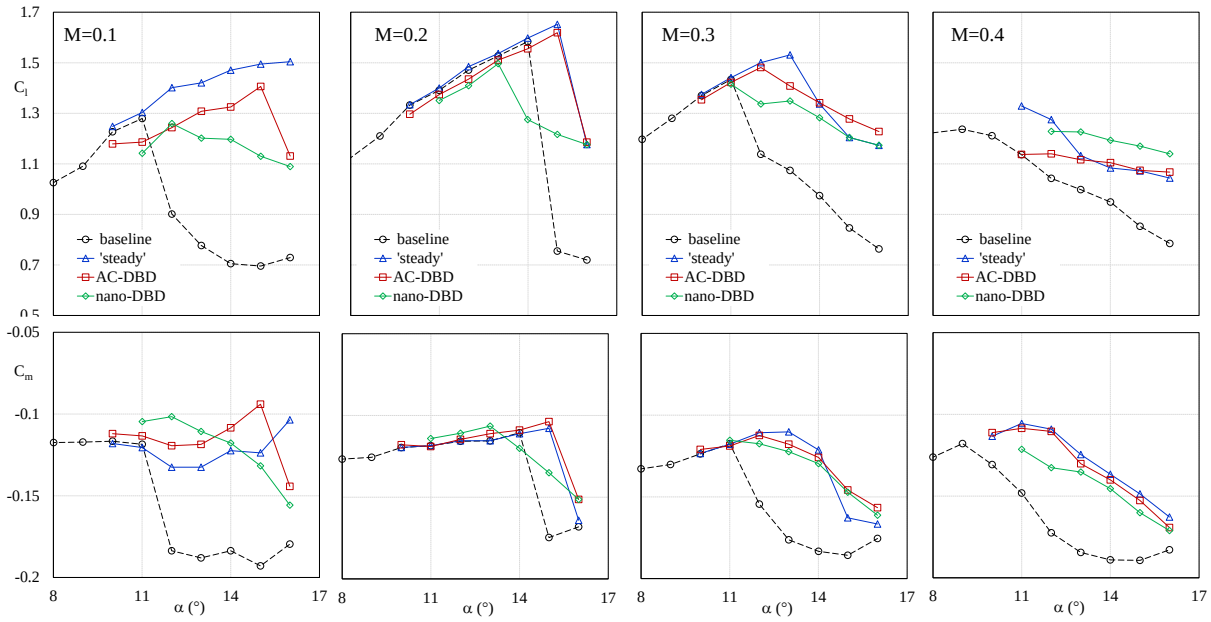

Figure 38. Effect of AC-DBD plasma actuation at $F^+ = 1$ (3.175 mm thick ceramic dielectric, $V_{pp} = 30$ kV, modulation at d.c. = 50%) and pulsed-DC-DBD actuation at $F^+ = 1$ (0.127-mm-thick Kapton film dielectric, $V_{pp} = 11.9$ kV, pulse width ~100 ns) on static aerodynamic coefficients of a NASA Advanced EET airfoil. Data republished with permission.

A welcome result is that reduced frequencies effective under incompressible conditions are also effective under compressible conditions—particularly in light of the fact that incompressible separation control relies on excitation of the LSB. Recent wall-resolved LES of an LSB on a stationary NACA 0012 airfoil for $M \ge 0.4$, revealed that the flow structure in the

locally supersonic region exhibits self-sustained oscillations at frequencies an order of magnitude lower than the shear-layer instability [279]. The source of the oscillations is attributed to coupling between the displaced shear layer and the train of compression/expansion systems, while high-frequency perturbations significantly reduced the oscillations. This provides some indication that the excitation mechanism remains effective at compressible flow Mach numbers. The static results presented above serve as a strong motivation for applying DBD-based actuation to helicopter dynamic stall control, in particular because they are effective in both compressible and incompressible regimes and their effectiveness does not diminish with Reynolds number.

Extending airfoil results to the helicopter rotor problem requires considerations that the control parameters vary along the blade span. For a model helicopter with a constant chord-length blades in hover, at $M_{\text{tip}} = 0.3$, nanosecond pulsed-DC actuation at a nominal tip reduced frequency $F_t^+ \equiv f_p c / V_{\text{tip}} = 1.2$ produced maximum and post-stall lift forces increases of 17% and 50% respectively [100]. This encouraging result, which is consistent with incompressible rotor results [280,281], shows that excitation remains effective despite the fact that the local reduced frequency $F^+(r) = f_p c / V_{\text{rel}}(r)$ and Mach number $M(r) = V_{\text{rel}}(r)/a$ increase asymptotically and decrease linearly, respectively, with decreasing $\hat{r}$. It appears that the mild dependence of lift coefficients on F^+ for airfoils can be extended to understand how excitation operates in a quasi-two-dimensional manner along the span. Namely, because the variations in $F^+(r)$ are gradual on the outboard part of the span, at each section the excitation can be assumed to operate in a two-dimensional manner [280].

In forward flight, excitation-based dynamic stall control presents a greater challenge than in hover, because (i) the problem is dynamic, and (ii) $F^+(r)$ varies more aggressively from the tip towards the hub, and across the compressible-incompressible flow boundary. For the example shown in Figure 1 (see section 2.1), where $\mu = 0.237,$ a constant actuator frequency along the span to produces $F_t^+ = 1$ at $\Psi = 270°$ (where $M_{\text{tip}} = 0.4$), while $F^+(\hat{r} = 0.8) = 1.4$ and $F^+(\hat{r} = 0.6) = 2.1.$ At higher advance ratios, e.g., $\mu = 0.4$, $F^+(\hat{r} = 0.8) = 1.5$ and $F^+(\hat{r} = 0.6) = 3$. While dynamic stall is generally associated with the retreating blade stall, [30,31] showed that it can occur in all quadrants across virtually the entire blade span under extreme maneuvering, such as pull-up and high-speed diving turn maneuvers. By way of example, a dynamic stall map for a pitch-up maneuver at $\mu = 0.341$ produced by [30,31], is

shown together with Mach number and F^+ maps in Figure 39. By comparing the two maps on the left, it is clear that compressible dynamic stall can occur in the first quadrant and that incompressible dynamic stall can commence in the second quadrant. For a constant perturbation frequency f_p, selected to produce $F_t^+ = 1$ at $\Psi = 270°$, the relevant variations in $F^+(\hat{r})$ fall mainly within the effective range, i.e., between 0.5 and 4. Note, however, that a constant physical perturbation entire azimuth is not a limitation. Indeed, a major advantage of DBD plasma actuators is that the physical pulsation frequency can be varied at time-scales that are very much smaller than the rotor period. Hence, in principle, appropriate physical perturbation frequencies can be selected depending upon the occurrence and severity of dynamic stall.

Despite many challenges, it is the opinion of this author that DBD plasma actuators should be evaluated for dynamic stall control in the compressible regime. Major advantages are that they are lightweight with no mechanical elements and as a result they can easily resist large g-forces. They also have a large and variable frequency bandwidth and consume relatively low power in comparison to their aerodynamic benefit. Furthermore, more than one configuration can be integrated into the blade geometry, to handle different dynamic stall scenarios.

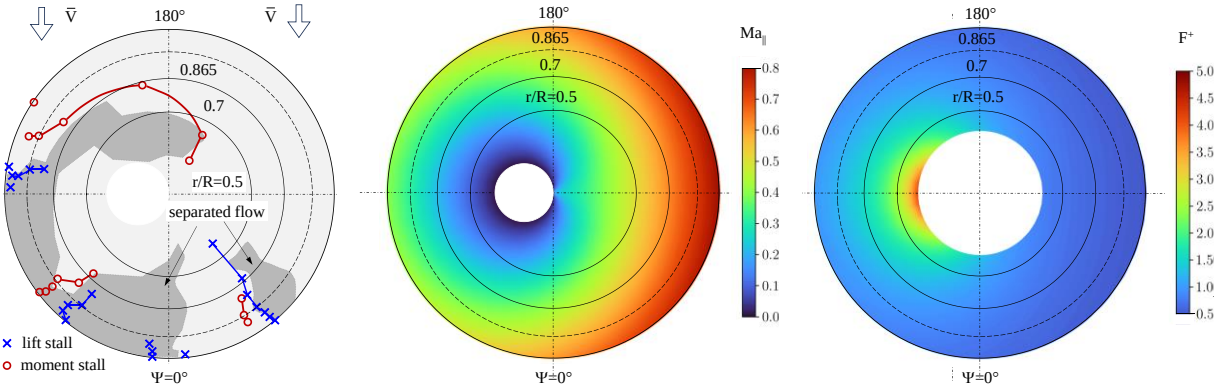

Figure 39. Left: Dynamic stall map corresponding to a pitch-up maneuver from [30,31] for $\mu = 0.341$ (blade loading = 2.09). Center and right: Corresponding Mach number and F^+ maps (reverse flow masked).

5 Conclusions, Recommendations and Outlook

This review considered the most common, technologically relevant, occurrences of dynamic stall and defined the control objectives associated with each. These included dynamic stall on helicopter and wind turbine blades, fixed-wing aircraft wings, flapping wings, as well the alternating separation and attachment produced by cyclical control inputs.

After describing the different types of incompressible airfoil and finite wing dynamic stall, common control metrics were defined. This was followed by descriptions of dynamic stall management, as well as popular passive devices and active control techniques. Leading-edge slot blowing, that can either suppress or induce dynamic stall, was identified as being well-suited to the problem of load control on horizontal axis wind turbines. This method has far greater control authority than active trailing-edge flaps, or other devices and methods, with the added advantage of no external mechanical moving parts. The large control authority was demonstrated experimentally by employing iterative learning control under synchronous changes in angle-of-attack and freestream velocity, and by feedforward control simulations. The author recommends this method for future development.

The use of periodic excitation or periodic forcing perturbations, long known to be effective under static conditions, was reviewed in the context of dynamic stall control. When a large disparity exists between the airfoil or wing pitching frequency and the perturbation frequency, then effective control under incompressible static conditions translates to effective control under dynamic conditions. This was observed both with regard to the averaged static versus pitching-cycle phase-averaged dynamic data as well as the perturbation-cycle averaged pressure fluctuations under static and dynamic conditions. The effectiveness of perturbations degrades significantly, however, near the tips of swept wings. The apparent conundrum that both pitching airfoils or wings that stall dynamically and periodic perturbations that eliminate dynamic stall both produce leading-edge vortices, was explained by the large time-scale disparity between the two.

Dynamic pitching of an airfoil or wing serves and an excellent vehicle for more general dynamic stall control studies. This was shown using matched pitchrate, and matched inflow concepts, where the variation of pitching frequency can serve as a surrogate for angle-of-attack amplitude changes, and matched inflow can be used to reduce the surging-flow parameter space. Furthermore, use of the pitch-plunge equivalence for dynamically stalling airfoils, as well as swept and unswept wings, allows a significant reduction in the scope of experimental or computational test matrices.

The method of scheduled control, at predetermined modulated input at the dynamic stall and attachment timescales, was used as a vehicle to demonstrate load excursion increases on airfoils and bluff-bodies, optimization of vertical axis wind turbine net power output, control of trailing vortices, and control of turbulent mixing. In particular, forced periodic separation and attachment of flap flows shows potential for trailing vortex perturbation or blade-vortex-interaction noise reduction.

The control of dynamic stall on flapping wing flyers differs depending upon whether propulsive flight or hovering are considered. In propulsive flight, maximum thrust and peak propulsive efficiency occur close to the dynamic stall boundary, and the objective is to suppress or eliminate the LEV. Presently, this is achieved by design, namely, by a judicious combination angles, flapping amplitude, and frequency. Active methods should be considered as surrogates for naturally occurring high-lift devices, such as the use of DBD plasma actuators as a surrogate for alula on bird wings. In contrast to propulsive flight, hovering relies on dynamic stall for lift. Regardless of wing morphology, wing kinematics produce unsteady vortex-dominated flows, where the wings themselves are the actuators. It was shown in this review, that similar Strouhal numbers are associated with insect flight, leading-edge forcing on flat-plate airfoils and wings, and possibly bluff-body vortex shedding.

Closed-loop control most commonly involves some form of lift or moment control—by suppressing or eliminating dynamic stall—and the strategy and implementation depend upon the specific objectives. The two examples reviewed are adaptations of various stall-warning sensors that are used to drive simple on-off control, and a popular feedforward/feedback control architecture that requires disturbance and plant models to design the feedforward and feedback controllers. The utility of this architecture was illustrated by examples of feedforward and feedback control of airfoils and wings subjected to dynamic pitching and pseudorandom longitudinal velocity variations.

Accurate predictions of dynamic stall control, in terms of validated predictive capability against experimental data, appear to be lacking for both passive devices and active control methods. The least computationally expensive methods, e.g., URANS, appear capable of predicting correct trends of control schemes, while high-fidelity implicit LES produces improved correspondence with data under static conditions. It appears that Hybrid RANS-LES turbulence models are likely the best option for near-term practical dynamic stall control computations. The author recommends use of the extensive surface pressure and PIV data sets that employ leading-edge blowing: https://www.flowcontrollab.com/data-resource for numerical validation of incompressible dynamic stall control.

Compressible dynamic stall control research, associated with relative Mach numbers greater than 3, is mainly driven by conditions experienced by helicopter blades during high-speed forward flight and while performing aggressive maneuvers. Unlike incompressible flows, a relatively small supercritical region forms downstream of the leading-edge which leads to shock-induced dynamic stall. Three main approaches were identified that show potential. The first is nominally passive and involves a leading-edge extension (or "glove"), together with vortex generators. The second is discrete wall-normal jet or micro-jet blowing, where the jets mimic the effect of small or micro vortex generators, that produce counter-rotating vortex pairs between the jet and the external stream. Finally, dielectric barrier discharge plasma actuators should be considered for helicopter blade dynamic stall control due to their demonstrated utility at Mach numbers greater than 3 on airfoils, the positive effects on hover, low power requirements, light weight, and large and variable frequency bandwidth.

Acknowledgements

Many of the results presented in this review were based on research supported by the Israel Science Foundation (Grants No. 840/11 and 2778/20).

References

1. Gardner, A.D., Jones, A.R., Mulleners, K., Naughton, J.W. and Smith, M.J., 2023. Review of rotating wing dynamic stall: Experiments and flow control. Progress in Aerospace Sciences, 137, p. 100887.
2. Jones A.R., Cetiner O. 2021. Overview of unsteady aerodynamic response of rigid wings in gust encounters. AIAA J. 59(2):731–36.
3. Darabi, A. and Wygnanski, I., 2004. Active management of naturally separated flow over a solid surface. Part 2. The separation process. Journal of Fluid Mechanics, 510, pp. 131-144.
4. Zaman, K.B.M.Q., McKinzie, D.J. and Rumsey, C.L., 1989. A natural low-frequency oscillation of the flow over an airfoil near stalling conditions. Journal of Fluid Mechanics, 202, pp. 403-442.
5. Greenblatt, D. and Wygnanski, I., 2003. Effect of leading-edge curvature on airfoil separation control. Journal of Aircraft, 40(3), pp. 473-481.
6. Crimi, P. and Reeves, B.L., 1972. A method for analyzing dynamic stall of helicopter rotor blades (No. NASA-CR-2009). NASA.
7. Prouty, R.W., 1995. Helicopter performance, stability, and control. Krieger Publishing Company.
8. Conlisk, A.T., 1997. Modern helicopter aerodynamics. Annual review of fluid mechanics, 29(1), pp. 515-567.
9. Jahani, K., Langlois, R.G. and Afagh, F.F., 2022. Structural dynamics of offshore Wind Turbines: A review. Ocean Engineering, 251, p.111136.
10. Paraschivoiu I., "Double-multiple streamtube model for studying vertical-axis wind turbines," AIAA Journal of Propulsion, Vol. 4, No. 4, 1987, pp. 370-377. https://doi.org/10.2514/3.23076.
11. Gallaway, C. and Osborn, R., 1985. Aerodynamics perspective of super-maneuverability. In 3rd Applied Aerodynamics Conference (p. 4068).
12. Keisar, D., Hasin, D. and Greenblatt, D., 2019. Plasma actuator application on a full-scale aircraft tail. AIAA Journal, 57(2), pp. 616-627.
13. Platzer, M.F., Jones, K.D., Young, J. and Lai, J.C., 2008. Flapping wing aerodynamics: progress and challenges. AIAA Journal, 46(9), pp. 2136-2149.

14. Ho, S., Nassef, H., Pornsinsirirak, N., Tai, Y.C. and Ho, C.M., 2003. Unsteady aerodynamics and flow control for flapping wing flyers. Progress in aerospace sciences, 39(8), pp. 635-681.
15. Shyy, W., Kang, C.K., Chirarattananon, P., Ravi, S. and Liu, H., 2016. Aerodynamics, sensing and control of insect-scale flapping-wing flight. Proceedings of the Royal Society A: Mathematical, Physical and Engineering Sciences, 472(2186), p.20150712.
16. McCroskey, W.J., 1981. The phenomenon of dynamic stall (No. A-8464).
17. Carr, L.W., 1988. Progress in analysis and prediction of dynamic stall. Journal of aircraft, 25(1), pp. 6-17.
18. Ekaterinaris, J.A. and Platzer, M.F., 1998. Computational prediction of airfoil dynamic stall. Progress in Aerospace Sciences, 33(11-12), pp. 759-846.
19. Carr, L.W. and Chandrasekhara, M.S., 1996. Compressibility effects on dynamic stall. Progress in Aerospace Sciences, 32(6), pp. 5 23-573.
20. Corke, T.C. and Thomas, F.O., 2015. Dynamic stall in pitching airfoils: aerodynamic damping and compressibility effects. Annual Review of Fluid Mechanics, 47(1), pp. 479-505.
21. Müller-Vahl, H.F., Nayeri, C.N., Paschereit, C.O. and Greenblatt, D., 2016. Dynamic stall control via adaptive blowing. Renewable Energy, 97, pp. 47-64.
22. Garcia, M., Mongin, M. and Greenblatt, D. 2025. Closed-Loop Dynamic Stall Control Using a Stall-Warning Sensor. EngrXiv. https://doi.org/10.31224/4423.
23. Ol, M.V., Bernal, L., Kang, C.K. and Shyy, W., 2010. Shallow and deep dynamic stall for flapping low Reynolds number airfoils. Animal locomotion, pp. 321-339.
24. Keisar, D., Arava, I. and Greenblatt, D., 2024. Dynamic-stall-driven vertical axis wind turbine: An experimental parametric study. Applied Energy, 365, p.123199.
25. Cattafesta III, L.N. and Sheplak, M., 2011. Actuators for active flow control. Annual Review of Fluid Mechanics, 43(1), pp. 247-272.
26. Darabi, A. and Wygnanski, I., 2004. Active management of naturally separated flow over a solid surface. Part 1. The forced reattachment process. Journal of Fluid Mechanics, 510, pp. 105-129.
27. Williams, D.R. and King, R., 2018. Alleviating unsteady aerodynamic loads with closed-loop flow control. AIAA Journal, 56(6), pp. 2194-2207.
28. Greenblatt, D., Melton, L., Yao, C.S. and Harris, J., 2005. Active Control of a Wing Tip Vortex. In 23rd AIAA Applied Aerodynamics Conference (p. 4851).

29. Martin, P., Wilson, J., Berry, J., Wong, T.C., Moulton, M. and McVeigh, M., 2008, August. Passive control of compressible dynamic stall. In 26th AIAA Applied Aerodynamics Conference (p. 7506).
30. Bousman, W.G., 1998. A qualitative examination of dynamic stall from flight test data. Journal of the American Helicopter Society, 43(4), pp. 279-295.
31. Bousman, W.G. and Kufeld, R.M., 2005. UH-60A Airloads Catalog (No. NASA/TM-2005-212827). National Aeronautics and Space Administration.
32. Harris, F.D. and Pruyn, R.R., "Blade Stall-Half Fact, Half Fiction," Journal of the American Helicopter Society, Vol. 13, No. 2, April 1968, pp. 27-48.
33. Chen, R., Yuan, Y. and Thomson, D., 2021. A review of mathematical modelling techniques for advanced rotorcraft configurations. Progress in Aerospace Sciences, 120, p. 100681.
34. Yeo, H., 2019. Design and aeromechanics investigation of compound helicopters. Aerospace Science and Technology, 88, pp. 158-173.
35. Bastian, N.D., Fulton, L.V., Mitchell, R., Pollard, W., Wierschem, D. and Wilson, R., 2012. The future of vertical lift: initial insights for aircraft capability and medical planning. Military Medicine, 177(7), pp. 863-869.
36. Barbely, N.L. and Komerath, N.M., 2016, September. Coaxial rotor flow phenomena in forward flight. In 2016 International Powered Lift Conference (IPLC)/SAE Aerospace Systems and Technology Conference (No. ARC-E-DAA-TN31139).
37. Feil, R., Hajek, M. and Rauleder, J., 2020. Vibratory load predictions of a high-advance-ratio coaxial rotor system validated by wind tunnel tests. Journal of Fluids and Structures, 92, p. 102764.
38. Singh, P. and Friedmann, P.P., 2021. Aeromechanics and aeroelastic stability of coaxial rotors. Journal of Aircraft, 58(6), pp. 1386-1405.
39. Lind, A.H., Smith, L.R., Milluzzo, J.I. and Jones, A.R., 2016. Reynolds number effects on rotor blade sections in reverse flow. Journal of Aircraft, 53(5), pp. 1248-1260.
40. Turhan, B., Wang, Z. and Gursul, I., 2022. Coherence of unsteady wake of periodically plunging airfoil. Journal of Fluid Mechanics, 938, p. A14.
41. Dunne R. and McKeon, B. J., 2015. Dynamic stall on a pitching and surging airfoil. Exp. Fluids 56, 157.
42. Müller-Vahl, H.F., Strangfeld, C., Nayeri, C.N., Paschereit, C.O. and Greenblatt, D., "Dynamic stall under combined pitching and surging," AIAA Journal, Vol. 58, No. 12, 2020, pp. 5134-5145. https://doi.org/10.2514/1.J059153.

43. Simms, D., Schreck, S., Hand, M. and Fingersh, L. J. NREL unsteady aerodynamics experiment in the NASA-Ames wind tunnel: A comparison of predictions to measurements, Technical Report No. NREL/TP-500-29494, National Renewable Energy Laboratory, Golden, Colorado, 2001.
44. Granlund, K., Monnier, B., Ol, M., and Williams, D., "Airfoil Longitudinal Gust Response in Separated vs Attached Flows," Physics of Fluids, Vol. 26, No. 2, 2014, doi:10.1063/1.4864338.
45. Choi, J., Colonius, and Williams, D., "Surging and Plunging Oscillations of an Airfoil at Low Reynolds Number," Journal Fluid Mechanics, Vol. 763, Jan. 2015, pp. 237–253. doi:10.1017/jfm.2014.674.
46. Medina, A. Ol, M.V., Greenblatt, D., Müller-Vahl, H. and Strangfeld, C., 2018. High-amplitude surge of a pitching airfoil: Complementary wind- and water-tunnel measurements, AIAA J. 56, 1703.
47. Granlund, K.O., Ol, M.V. and Jones, A.R., 2016. Streamwise oscillation of airfoils into reverse flow. AIAA Journal, 54(5), pp. 1628-1636.
48. Kirk, P.B. and Jones, A.R., 2019. Vortex formation on surging aerofoils with application to reverse flow modelling. Journal of fluid mechanics, 859, pp. 59-88.
49. Toppings, C. and Yarusevych, S., 2023. Transient dynamics of laminar separation bubble formation and bursting. Experiments in Fluids, 64(3), p. 57.
50. Greenblatt, D., Müller-Vahl, H.F., Strangfeld, C., 2023. Laminar Separation Bubble Bursting in a Surging Stream. Physical Review Fluids, 8, No. 1, L012102.
51. Strangfeld, C., Müller-Vahl, H., Nayeri, C.N., Paschereit, C.O. and Greenblatt, D., 2016. Airfoil in a high amplitude oscillating stream, J. Fluid Mech. 793, 79.
52. Butterfield, C. P., Simms, D., Scott, G., and Hansen, A. C., "Dynamic stall on wind turbine blades," Proceedings of Wind Power 91, Palm Springs, CA, USA, 24-27 September 1991.
53. Shipley D.E., Miller M.S. and Robinson M.C., "Dynamic Stall Occurrence on a Horizontal Axis Wind Turbine Blade", SED-Vol 16, Wind Energy - 1995, ASME 1995.
54. Munduate, X. and Coton, F., 2000. Identification of dynamic stall regions on horizontal axis wind turbines. In 2000 ASME Wind Energy Symposium (p. 39).
55. He, Z., Li, G., Duan, L. and Sun, Q., 2023. Dynamic process and dynamic-stall phenomenon on blade sections of a floating horizontal-axis wind turbine caused by the platform's pitch motion. Ocean Engineering, 286, p.115556.

56. Hong, S., McMorland, J., Zhang, H., Collu, M. and Halse, K.H., 2024. Floating offshore wind farm installation, challenges and opportunities: A comprehensive survey. Ocean Engineering, 304, p.117793.
57. Micallef, D. and Rezaeiha, A., 2021. Floating offshore wind turbine aerodynamics: Trends and future challenges. Renewable and Sustainable Energy Reviews, 152, p.111696.
58. Paraschivoiu, I., 2002. Wind turbine design: with emphasis on Darrieus concept. Presses inter Polytechnique.
59. Möllerström, E., Gipe, P., Beurskens, J. and Ottermo, F., 2019. A historical review of vertical axis wind turbines rated 100 kW and above. Renewable and Sustainable Energy Reviews, 105, pp. 1-13.
60. Klimas, P. C., "Vertical-Axis Wind Turbine Aerodynamic Performance Prediction Methods," Proceedings of the Vertical-Axis Wind Turbine (VAWT), Albuquerque, NM, April 1980, pp. 215-232.
61. Paraschivoiu, I., "Double-Multiple Streamtube Model for Darrieus Wind Turbines," Second DOE/NASA Wind Turbines Dynamics Workshop, NASA CP-2186, Cleveland, OH, USA, 1981, pp. 19-25.
62. Arava, I., Keisar, D. and Greenblatt, D., 2024. Conformally Decambered Natural Laminar Flow Blades for Vertical-Axis Wind Turbines. AIAA Journal, 62(8), pp. 3027-3038.
63. Keisar, D., De Troyer, T. and Greenblatt, D., "Concept and operation of a wind turbine driven by dynamic stall," AIAA Journal, Vol. 58, No. 6, 2020, pp. 2370-2376. https://doi.org/10.2514/1.J059487.
64. Le Fouest, S. and Mulleners, K., 2022. The dynamic stall dilemma for vertical-axis wind turbines. Renewable Energy, 198, pp. 505-520.
65. Goman, M. and Khrabrov, A., "State-space representation of aerodynamic characteristics of an aircraft at high angles-of-attack," *Journal of Aircraft*, Vol. 31, No. 5, 1994, pp. 1109-1115. https://doi.org/10.2514/3.46618.
66. Brandon, J.M., 1991. Dynamic stall effects and applications to high performance aircraft. *Aircraft Dynamics at High Angles-of-attack: Experiments and Modelling*.
67. Jones, A.R., Cetiner, O. and Smith, M.J., 2022. Physics and modeling of large flow disturbances: discrete gust encounters for modern air vehicles. Annual Review of Fluid Mechanics, 54(1), pp. 469-493.

68. Shyy, W., Aono, H., Chimakurthi, S.K., Trizila, P., Kang, C.K., Cesnik, C.E. and Liu, H., 2010. Recent progress in flapping wing aerodynamics and aeroelasticity. Progress in Aerospace Sciences, 46(7), pp. 284-327.
69. Orlowski, C.T. and Girard, A.R., 2012. Dynamics, stability, and control analyses of flapping wing micro-air vehicles. Progress in Aerospace Sciences, 51, pp. 18-30.
70. Keennon, M., Klingebiel, K. and Won, H., 2012, January. Development of the nano hummingbird: A tailless flapping wing micro air vehicle. In 50th AIAA aerospace sciences meeting including the new horizons forum and aerospace exposition (p. 588).
71. Ellington, C.P., Van Den Berg, C., Willmott, A.P. and Thomas, A.L., 1996. Leading-edge vortices in insect flight. Nature, 384(6610), pp. 626-630.
72. Liu, H., Wang, S. and Liu, T., 2024. Vortices and forces in biological flight: Insects, birds, and bats. Annual Review of Fluid Mechanics, 56(1), pp. 147-170.
73. Liu, H., Kolomenskiy, D., Nakata, T. and Li, G., 2017. Unsteady bio-fluid dynamics in flying and swimming. Acta Mechanica Sinica, 33, pp. 663-684.
74. McAlister, K.W., Carr, L.W. and McCroskey, W.J., 1978. Dynamic stall experiments on the NACA 0012 airfoil (No. NASA-TP-1100).
75. Currier, J.M. and Fung, K.Y., 1992. Analysis of the onset of dynamic stall. AIAA journal, 30(10), pp. 2469-2477.
76. A.J. Niven, R.A.M. Galbraith, D.G.F. Herring, Analysis of reattachment during ramp down tests, Vertica 13 (2) (1989) 187 196.
77. Ahmed, S. and Chandrasekhara, M.S., 1994. Reattachment studies of an oscillating airfoil dynamic stall flowfield. AIAA Journal, 32(5), pp. 1006-1012.
78. Green, R.B. and Galbraith, R.M., 1995. Dynamic recovery to fully attached aerofoil flow from deep stall. AIAA Journal, 33(8), pp. 1433-1440.
79. Rezapour, S. and Mulleners, K., 2025. Dynamic stall reattachment revisited. arXiv preprint arXiv:2505.12798.
80. Müller-Vahl, H., Strangfeld, C., Nayeri, C.N., Paschereit, C.O. and Greenblatt, D., "Thick airfoil dynamic stall," in "Wind Energy – Impact of Turbulence," Eds. M. Hölling, J. Peinke and S. Ivanell, Springer, pp. 35-40, 2013. https://doi.org/10.1007/978-3-642-54696-9_6.
81. Müller-Vahl, H.F. "Wind Turbine Blade Dynamic Stall and its Control," PhD, Technion – Israel Institute of Technology, 2015.

82. Williams, D.R., Reißner, F., Greenblatt, D., Müller-Vahl, H. and Strangfeld, C., 2017. Modeling lift hysteresis on pitching airfoils with a modified Goman–Khrabrov model. AIAA Journal, 55(2), pp. 403-409.
83. Granlund, K.O., Ol, M.V. and Bernal, L.P., 2013. Unsteady pitching flat plates. Journal of Fluid Mechanics, 733, p.R5.
84. Yu, Y., Amandolese, X., Fan, C. and Liu, Y., 2018. Experimental study and modelling of unsteady aerodynamic forces and moment on flat plate in high amplitude pitch ramp motion. Journal of Fluid Mechanics, 846, pp. 82-120.
85. Liu, L.G., Du, G. and Sun, M., 2020. Aerodynamic-force production mechanisms in hovering mosquitoes. Journal of Fluid Mechanics, 898, p. A19.
86. Visbal, M.R. and Garmann, D.J., 2020. Mitigation of dynamic stall over a pitching finite wing using high-frequency actuation. AIAA Journal, 58(1), pp. 6-15.
87. De Troyer, T., Hasin, D., Keisar, D., Santra, S. and Greenblatt, D., 2022. Plasma-based dynamic stall control and modeling on an aspect-ratio-one wing. AIAA Journal, 60(5), pp. 2905-2915.
88. Visbal, M.R. and Garmann, D.J., "Effect of Sweep on Dynamic Stall of a Pitching Finite-Aspect-Ratio Wing," *AIAA Journal*, Vol. 57, No. 8, 2019, pp. 3274-3289. https://doi.org/10.2514/1.J058206.
89. Spentzos, A., Barakos, G. N., Badcock, K. J., Richards, B. E., Coton, F. N., Galbraith, R. A. McD., Berton, E., and Favier, D., "Computational Fluid Dynamics Study of Three-Dimensional Dynamic Stall of Various Planform Shapes," Journal of Aircraft, Vol. 44, No. 4, 2007, pp. 1118–1128.
90. Mitchell, A.M. and Délery, J., "Research into vortex breakdown control," *Progress in Aerospace Sciences*, Vol. 37, 2001, pp. 385-418. https://doi.org/10.1016/S0376-0421(01)00010-0.
91. Nelson, R. C., and Pelletier, A. (2003). The unsteady aerodynamics of slender wings and aircraft undergoing large amplitude maneuvers. Progress in Aerospace Sciences, 39(2-3), 185-248.
92. Gad-el-Hak, M. and Ho, C-M., "The Pitching Delta Wing," *AIAA Journal*, Vol. 23, No. 11, 2005, 1985, pp. 1660-1665. http://dx.doi.org/10.2514/3.9147.
93. Gursul, I., "Review of Unsteady Vortex Flows Over Slender Delta Wings," *Journal of Aircraft*, Vol. 42, No. 2, 2005, pp. 299-319. https://doi.org/10.2514/1.5269.
94. LeMay, S.P., Batill, S.M., Nelson, R.C., "Vortex dynamics on a pitching delta wing," *Journal of Aircraft*, Vol. 27, No. 2, 1990, pp. 131-138. https://doi.org/10.2514/3.45908.

95. Atta, R. and Rockwell, D., "Leading-edge vortices due to low Reynolds number flow past a pitching delta wing," *AIAA Journal*, Vol. 28, No. 6, 1990, pp. 995-1004. https://doi.org/10.2514/3.25156.
96. Rediniotis, O.K., Klute, S.M., Hoang, N.T. and Telionis D.P., "Dynamic Pitch-Up of a Delta Wing," *AIAA Journal*, Vol. 32, No. 4, 1994, pp. 716-725. https://doi.org/10.2514/3.12044.
97. Gursul, I. and Yang, H., "Vortex Breakdown over a Pitching Delta Wing," *Journal of Fluids and Structures*, Vol. 9, 1995, pp. 571-583. https://doi.org/10.1006/jfls.1995.1032.
98. Cooperman, A. and Martinez, M., 2015. Load monitoring for active control of wind turbines. Renewable and Sustainable Energy Reviews, 41, pp. 189-201.
99. Bousman, W. G., "Evaluation of airfoil dynamic stall characteristics for maneuverability", 26th European Rotorcraft Forum, The Hague, Netherlands, 26-29 September, 2000, pp. 38.1-38.21.
100. Greenblatt, D. and Wygnanski, I., 2001. Dynamic stall control by periodic excitation, Part 1: NACA 0015 parametric study. Journal of Aircraft, 38(3), pp. 430-438.
101. Bowles P. 2012. Wind tunnel experiments on the effect of compressibility on the attributes of dynamic stall. PhD Thesis, University of Notre Dame.
102. Tummala, A., Velamati, R.K., Sinha, D.K., Indraja, V. and Hari Krishna,V., "A review on small scale wind turbine," Renewable and Sustainable Energy Reviews, Vol. 56, 2016, pp, 1351-1371. http://dx.doi.org/10.1016/j.rser.2015.12.027.
103. Keisar, D., Eilan, B. and Greenblatt, D., "High pressure vertical axis wind pump," Journal of Fluids Engineering, Vol. 143, Issue 5, 2021, 051204 (9 pages). https://doi.org/10.1115/1.4049692.
104. Keisar, D., Freger, V. and Greenblatt, D., "Direct wind-powered vertical axis brackish water desalination system," Desalination, Vol. 570, 2024, pp. 117060. https://doi.org/10.1016/j.desal.2023.117060.
105. Miller, M.A., Duvvuri, S. and Hultmark, M., "Solidity effects on the performance of vertical- axis wind turbines," Flow, Vol. 1, E9, 2021. https://doi.org/10.1017/flo.2021.9.
106. Greenblatt, D., Ben-Harav, A. and Mueller-Vahl, H., "Dynamic stall control on a vertical-axis wind turbine using plasma actuators," AIAA Journal, Vol. 52, No. 2, 2014, pp. 456-462. http://dx.doi.org/10.2514/1.J052776.
107. Lin, J.C., 2002. Review of research on low-profile vortex generators to control boundary-layer separation. Progress in aerospace sciences, 38(4-5), pp. 389-420.

108. Zhao, Z., Jiang, R., Feng, J., Liu, H., Wang, T., Shen, W., Chen, M., Wang, D. and Liu, Y., 2022. Researches on vortex generators applied to wind turbines: A review. Ocean Engineering, 253, p. 111266.
109. Jayanarasimhan, K. and Balasubramanian, N.K., 2025. An overview of flow control in aerodynamic surfaces using vortex generators. Physics of Fluids, 37(3).
110. Skrzypiński, W., Gaunaa, M., Bak, C., Junker, B., Brønnum, N.B. and Kruse, E.K., 2020. Increase in the annual energy production due to a retrofit of vortex generators on blades. Wind Energy, 23(3), pp. 617-626.
111. Mueller-Vahl, H., Pechlivanoglou, G., Nayeri, C.N. and Paschereit, C.O., 2012, June. Vortex generators for wind turbine blades: A combined wind tunnel and wind turbine parametric study. In Turbo Expo: Power for Land, Sea, and Air (Vol. 44724, pp. 899-914). American Society of Mechanical Engineers.
112. De Tavernier, D., Ferreira, C., Viré, A., LeBlanc, B. and Bernardy, S., 2021. Controlling dynamic stall using vortex generators on a wind turbine airfoil. Renewable Energy, 172, pp. 1194-1211.
113. Heine, B., Mulleners, K., Joubert, G. and Raffel, M., 2013. Dynamic stall control by passive disturbance generators. AIAA Journal, 51(9), pp. 2086-2097.
114. Quackenbush, T., McKillip, R. and Whitehouse, G., "Development and testing of deployable vortex generators using SMA actuation," 28th AIAA Applied Aerodynamics Conference, p. 4686, 2010.
115. Nissle, S., Kaiser, M., Hübler, M., Gurka, M. and Breuer, U., "Adaptive vortex generators based on active hybrid composites: from idea to flight test," CEAS Aeronautical Journal, Vol. 9, 2018, pp. 661-670.
116. Morice, S.D., Ginnell, K., Geary, S., Baughn, J. and Robinson, S.K., "Detection of boundary layer separation and implementation of autonomous vortex generators," AIAA Scitech 2020 Forum, 2020, p. 0788.
117. Le Pape, A., Costes, M., Richez, F., Joubert, G., David, F. and Deluc, J.M., 2012. Dynamic stall control using deployable leading-edge vortex generators. AIAA journal, 50(10), pp. 2135-2145.
118. Zhang, Y., Cattafesta, L., Pascioni, K. and Choudhari, M., 2024. Slat noise in high-lift systems. Progress in Aerospace Sciences, 146, p.100996.
119. Carr, L.W. and McAlister, K.W., "The Effect of a Leading-Edge Slat on the Dynamic Stall of an Oscillating Airfoil," AIAA Paper 83-2533, Oct. 1983.

120. Yu, Y.H., Lee, S., McAlister, K.W., Tung, C. and Wang, C.M., 1995. Dynamic stall control for advanced rotorcraft application. AIAA journal, 33(2), pp. 289-295.
121. Bechert, D.W., Hage, W. and Meyer, R., 2006. Self-actuating flaps on bird-and aircraft-wings. Flow phenomena in nature: inspiration, learning and applications, 2, pp. 435-446.
122. Meyer, R., Hage, W., Bechert, D.W., Schatz, M., Knacke, T. and Thiele, F., 2007. Separation control by self-activated movable flaps. AIAA Journal, 45(1), pp. 191-199.
123. Gardner, A.D., Opitz, S., Wolf, C.C. and Merz, C.B., 2017. Reduction of dynamic stall using a back-flow flap. CEAS Aeronautical Journal, 8(2), pp. 271-286.
124. Gerontakos, P. and Lee, T., 2006. Dynamic stall flow control via a trailing-edge flap. AIAA journal, 44(3), pp. 469-480.
125. Wang, J.J., Li, Y.C. and Choi, K.S., 2008. Gurney flap—Lift enhancement, mechanisms and applications. Progress in Aerospace sciences, 44(1), pp. 22-47.
126. Ivanković, M., Manolesos, M., Jentzsch, M., Kozmar, H. and Nayeri, C.N., 2024, June. Dynamic stall of vertical-axis-wind-turbine rotor blades equipped with Gurney flaps and vortex generators. In Journal of Physics: Conference Series (Vol. 2767, No. 7, p. 072023). IOP Publishing.
127. Karim, M.A. and Acharya, M., 1994. Suppression of dynamic-stall vortices over pitching airfoils by leading-edge suction. AIAA journal, 32(8), pp. 1647-1655.
128. Young, T.M., Humphreys, B. and Fielding, J.P., 2001. Investigation of hybrid laminar flow control (HLFC) surfaces. Aircraft design, 4(2-3), pp. 127-146.
129. McCloud, K. L. III, Hall, L. P. and Brady, J. A., “Full-scale wind tunnel tests of blowing boundary layer control applied to helicopter rotor”, NASA TN D-335, 1960.
130. Weaver, D., McAlister, K. W., and Tso, J., “Control of VR-7 Dynamic Stall by Strong Steady Blowing,” Journal of Aircraft, Vol. 41, No. 6, 2004, pp. 1404–1413.
131. Nagib, H., Kiedaisch, J., Greenblatt, D., Wygnanski, I. and Hassan, A., 2001. Effective flow control for rotorcraft applications at flight Mach numbers. In 15th AIAA Computational Fluid Dynamics Conference (p. 2974).
132. Müller-Vahl, H.F., Strangfeld, C., Nayeri, C.N., Paschereit, C.O. and Greenblatt, D., 2015. Control of thick airfoil, deep dynamic stall using steady blowing. AIAA journal, 53(2), pp. 277-295.
133. Ma, C.Y., Xu, H.Y. and Qiao, C.L., 2023. Comparative study of two combined blowing and suction flow control methods on pitching airfoils. Physics of Fluids, 35(3).
134. Matalanis, C.G., Bowles, P.O., Min, B.Y., Jee, S., Kuczek, A.E., Wake, B.E., Lorber, P.F., Crittenden, T.M., Glezer, A. and Schaeffler, N.W., 2017. High-speed experiments

on combustion-powered actuation for dynamic stall suppression. AIAA Journal, 55(9), pp. 3001-3015.

135. Beahan, J.J., Shih, C., Krothapalli, A., Kumar, R. and Chandrasekhara, M.S., 2014. Compressible dynamic stall control using high momentum microjets. Experiments in fluids, 55, pp. 1-11.
136. Singh, C., Peake, D.J., Kokkalis, A., Khodagolian, V., Coton, F.N. and Galbraith, R.A.M., 2006. Control of rotorcraft retreating blade stall using air-jet vortex generators. Journal of Aircraft, 43(4), pp. 1169-1176.
137. Magill, J. and McManus, K., 1998. Control of dynamic stall using pulsed vortex generator jets. In 36th AIAA Aerospace Sciences Meeting and Exhibit (p. 675).
138. Greenblatt, D., 2010. Active Control of Leading-Edge Dynamic Stall. International Journal of Flow Control, 2(1).
139. Post, M.L. and Corke, T.C., 2006. Separation control using plasma actuators: dynamic stall vortex control on oscillating airfoil. AIAA journal, 44(12), pp. 3125-3135.
140. Starikovskiy, A., Meehan, K., Persikov, N. and Miles, R., 2019. Static and dynamic stall control by NS SDBD actuators. Plasma Sources Science and Technology, 28(5), p.054001.
141. Greenblatt, D., Doron, G. and Treizer, A., 2014. Wind-Energy Generation by Active Flow Control. International Journal of Flow Control, 6(2).
142. Gardner, A.D., Richter, K., Mai, H. and Neuhaus, D., 2014. Experimental investigation of high-pressure pulsed blowing for dynamic stall control. CEAS Aeronautical Journal, 5, pp. 185-198.
143. Greenblatt, D. and Williams, D.R., 2022. Flow control for unmanned air vehicles. Annual Review of Fluid Mechanics, 54(1), pp. 383-412.
144. Wygnanski, I., 2024. On the need to reassess the design tools for active flow control. Progress in Aerospace Sciences, 146, p.100995.
145. Jones, G.S. and Joslin, R.D. eds., 2006. Applications of circulation control technology. American Institute of Aeronautics and Astronautics.
146. Sasson, B. and Greenblatt, D., 2011. Effect of leading-edge slot blowing on a vertical axis wind turbine. AIAA Journal, 49(9), pp. 1932-1942.
147. Attinello, J. S. “Design and engineering features of flap blowing installations”, in Lachmann, G. V., “Boundary layer and Flow Control. Its Principles and Application”, Volume 1, pp. 463-515, Pergamon Press, New York, 1961.

148. Seifert, A., Darabi, A. and Wyganski, I., 1996. Delay of airfoil stall by periodic excitation. Journal of aircraft, 33(4), pp. 691-698.
149. Greenblatt, D. and Wygnanski, I., "The control of separation by periodic excitation," Progress in Aerospace Sciences, Volume 36, Issue 7, 2000, pp. 487-545.
150. Visbal, M.R., 2014. Numerical exploration of flow control for delay of dynamic stall on a pitching airfoil. In 32nd AIAA Applied Aerodynamics Conference (p. 2044).
151. Visbal, M.R. and Benton, S.I., "Exploration of High-Frequency Control of Dynamic Stall Using Large-Eddy Simulations," *AIAA Journal*, Vol. 56, No. 8, 2018, pp. 2975-2991. https://doi.org/10.2514/1.J056720.
152. Lilley, A.J., Roy, S. and Visbal, M.R., 2024. Novel plasma actuator for mitigation of dynamic stall. Physica Scripta, 99(8), p. 085605.
153. Nishri, B. and Wygnanski, I., 1998. Effects of periodic excitation on turbulent flow separation from a flap. AIAA Journal, 36(4), pp. 547-556.
154. Greenblatt, D., Nishri, B., Darabi, A. and Wygnanski, I., "Dynamic stall control by periodic excitation, Part 2: Mechanisms," Journal of Aircraft, Vol. 38, No. 3, 2001, pp. 439-447. https://doi.org/10.2514/2.2811.
155. Corke, T.C., Enloe, C.L. and Wilkinson, S.P., 2010. Dielectric barrier discharge plasma actuators for flow control. Annual Review of Fluid Mechanics, 42(1), pp. 505-529.
156. Richardson, L.F., 1922. Weather prediction by numerical process. University Press.
157. Greenblatt, D. and Washburn, A.E., 2008. Influence of finite span and sweep on active flow control efficacy. AIAA Journal, 46(7), pp. 1675-1694.
158. Greenblatt, D., Kastantin, Y., Nayeri, C.N. and Paschereit, C.O., 2008. Delta-wing flow control using dielectric barrier discharge actuators. AIAA Journal, 46(6), pp. 1554-1560.
159. Margalit, S., Greenblatt, D., Seifert, A. and Wygnanski, I., 2005. Delta wing stall and roll control using segmented piezoelectric fluidic actuators. Journal of Aircraft, 42(3), pp. 698-709.
160. Naveh, T., Seifert, A., Tumin, A. and Wygnanski, I., 1998. Sweep effect on parameters governing control of separation by periodic excitation. Journal of Aircraft, 35(3), pp. 510-512.
161. McCroskey, W.J., McAlister, K.W., Carr, L.W., Pucci, S.L., Lambert, O. and Indergrand, R.F., 1981. Dynamic stall on advanced airfoil sections. Journal of the American Helicopter Society, 26(3), pp. 40-50.

162. Müller-Vahl, H.F., Pechlivanoglou, G., Nayeri, C.N., Paschereit, C.O. and Greenblatt, D., 2017. Matched pitch rate extensions to dynamic stall on rotor blades. Renewable Energy, 105, pp. 505-519.
163. Theodorsen, T., "General Theory of Aerodynamic Instability and the Mechanism of Flutter," NACA Rept. 496, 1935.
164. Visbal, M.R. and Garmann, D.J., 2022. Pitch-plunge Equivalence for Dynamic Stall of Unswept Finite Wings. AIAA Journal, 60(8), pp. 4807-4817. https://doi.org/10.2514/1.J061331.
165. Garmann, D.J. and Visbal, M.R., 2022. Pitch-plunge equivalence for dynamic stall of swept finite wings. AIAA Journal, 60(8), pp. 4818-4828. https://doi.org/10.2514/1.J061332.
166. Greenblatt, D., Neuburger, D. and Wygnanski, I., 2001. Dynamic stall control by intermittent periodic excitation. Journal of Aircraft, 38(1), pp. 188-190.
167. Ghee, T.A. and Leishman, J.G., 1992. Unsteady circulation control aerodynamics of a circular cylinder with periodic jet blowing. AIAA Journal, 30(2), pp. 289-299.
168. C. H. K. Williamson and R. Govardhan, "Vortex-Induced Vibrations," *Annu. Rev. Fluid Mech.*, Vol. 36, pp. 413-455, 2004.
169. J. Wang, L. Geng, L. Ding, H. Zhu, and D., Yurchenko, "The state-of-the-art review on energy harvesting from flow-induced vibrations," *Applied Energy*, Vol. 267, 2020, p.114902.
170. H. Zhu, T. Tang, T. Zhou, M. Cai, O. Gaidai and J. Wang, "High performance energy harvesting from flow-induced vibrations in trapezoidal oscillators," *Energy*, Vol. 236, 2021, 121484. https://doi.org/10.1016/j.energy.2021.121484.
171. W. Sun, S. Jo and J. Seok, "Development of the optimal bluff body for wind energy harvesting using the synergetic effect of coupled vortex induced vibration and galloping phenomena," *International Journal of Mechanical Sciences*, Vol. 156, pp. 435-445, 2019.
172. R.D. Gabbai and H. Benaroya, "An overview of modeling and experiments of vortex-induced vibration of circular cylinder," *Journal of Sound and Vibration*, Vol. 282, pp. 575-616, 2005.
173. A. Abdelkefi, "Aero-elastic energy harvesting: A review," *International Journal of Engineering Science*, Vol. 100, pp. 112-135, 2016.
174. D. Greenblatt et al., "Flow-control-induced vibrations for power generation using pulsed plasma actuators," *Journal of Fluids and Structures*, Vol. 34, pp. 170-189, 2012.

175. A. Garzozi and D. Greenblatt, “A pulsed Coandă-effect reciprocating wind energy generator,” *Energy*, Vol. 150, pp. 965-978, 2018.
176. A. Garzozi, L. Dunaevich, and D. Greenblatt, “High-torque oscillating wind energy generator,” *J. Phys.: Conf. Ser.*, Vol. 1618, 2020.
177. A. Garzozi and D. Greenblatt, “Exploiting the Coandă effect for wind-driven reciprocating RO desalination,” *Energy*, Vol. 238, p. 121963, 2022.
178. Garzozi, A. and Greenblatt, D., 2023. Wind energy generation by forced vortex shedding. Applied Energy, 349, p.121583.
179. Greenblatt, D., Schulman, M. and Ben-Harav, A., “Vertical axis wind turbine performance enhancement using plasma actuators,” Renewable Energy, Vol. 37, 2012, pp. 345-354. http://doi.org/10.1016/j.renene.2011.06.040.
180. Ben-Harav, A. and Greenblatt, D., “Feed-forward dynamic stall control on a vertical axis wind turbine,” Wind Energy, Vol. 19, Issue 1, 2016, Pages 3-16. http://dx.doi.org/10.1002/we.1814.
181. Greenblatt, D., 2006. Managing flap vortices via separation control. AIAA Journal, 44(11), pp. 2755-2764.
182. Spalart, P.R., 1998. Airplane trailing vortices. Annual Review of Fluid Mechanics, 30(1), pp. 107-138.
183. Jacquin, L., 2005. On trailing vortices: A short review. International journal of heat and fluid flow, 26(6), pp. 843-854.
184. Yu, Y.H., 2000. Rotor blade-vortex interaction noise. Progress in Aerospace Sciences, 36(2), pp. 97-115.
185. Enenkl, B., Klöppel, V., Preißler, D. and Jänker, P., 2002, September. Full scale rotor with piezoelectric actuated blade flaps. In 28th European Rotorcraft Forum (pp. 17-19). London: Royal Aeronautical Society.
186. Batchelor, G., 1964. Axial flow in trailing line vortices. Journal of Fluid Mechanics, 20(4), pp. 645-658.
187. Greenblatt, D., 2012. Fluidic control of a wing tip vortex. AIAA Journal, 50(2), pp. 375-386.
188. Coats, C.M., 1996. Coherent structures in combustion. Progress in Energy and Combustion Science, 22(5), pp. 427-509.
189. Dimotakis, P. E. (2005). "Turbulent Mixing." Annual Review of Fluid Mechanics, 37, 329–356.

190. Waitz, I.A., Qiu, Y.J., Manning, T.A., Fung, A.K.S., Elliot, J.K., Kerwin, J.M., Krasnodebski, J.K., O'Sullivan, M.N., Tew, D.E., Greitzer, E.M. and Marble, F.E., 1997. Enhanced mixing with streamwise vorticity. Progress in Aerospace Sciences, 33(5-6), pp. 323-351.
191. Müller-Vahl, H., Nayeri, C.N., Paschereit, C.O. and Greenblatt, D., 2015. Mixing enhancement of an axisymmetric jet using flaplets with zero mass-flux excitation. *Experiments in Fluids*, *56*, pp. 1-22.
192. Tutty, O., Blackwell, M., Rogers, E. and Sandberg, R., 2013. Iterative learning control for improved aerodynamic load performance of wind turbines with smart rotors. IEEE Transactions on Control Systems Technology, 22(3), pp. 967-979.
193. Allahverdy, D., Fakharian, A. and Menhaj, M.B., 2021, February. Application of PID and norm optimal iterative learning control to Swash mass helicopter. In 2021 7th International Conference on Control, Instrumentation and Automation (ICCIA) (pp. 1-6). IEEE.
194. Barlas, T.K. and van Kuik, G.A.M., "Review of State of the Art in Smart Rotor Control Research for Wind Turbines," Progress in Aerospace Sciences, Vol. 46, No. 1, 2010, pp. 1-27.
195. Johnson, S.J., Baker, J.P., Van Dam, C.P. and Berg, D., 2010. An overview of active load control techniques for wind turbines with an emphasis on microtabs. Wind Energy: An International Journal for Progress and Applications in Wind Power Conversion Technology, 13(2-3), pp. 239-253.
196. Aubrun, S., Leroy, A. and Devinant, P., 2017. A review of wind turbine-oriented active flow control strategies. Experiments in Fluids, 58, pp. 1-21.
197. Gao, Z. and Odgaard, P., 2023. Real-time monitoring, fault prediction and health management for offshore wind turbine systems. Renewable Energy, 218, p. 119258.
198. Kerstens, W., Williams, D., Pfeiffer, J., King, R., and Colonius, T., "Closed-Loop Control of Lift for Longitudinal Gust Suppression at Low Reynolds Numbers," AIAA Journal, Vol. 49, No. 8, 2011, pp. 1721–1728. doi:10.2514/1.J050954
199. Leishman, J. G., and Beddoes, T., "A Semi-Empirical Model for Dynamic Stall," Journal of the American Helicopter Society, Vol. 34, No. 3, 1989, pp. 3-17. https://doi.org/10.4050/JAHS.34.3.3.
200. Brunton, S. and Rowley, C., 2009, January. Modeling the unsteady aerodynamic forces on small-scale wings. In 47th AIAA Aerospace Sciences Meeting including the New Horizons Forum and Aerospace Exposition (p. 1127).

201. Santra, S. and Greenblatt, D., 2021. Dynamic stall control model for pitching airfoils with slot blowing. AIAA Journal, 59(1), pp. 400-404.
202. Smith, M.J., 2020. An assessment of the state-of-the-art from the 2019 ARO dynamic stall workshop. In *AIAA Aviation 2020 Forum* (p. 2697).
203. Ayancik, F. and Mulleners, K., 2022. All you need is time to generalise the Goman-Khrabrov dynamic stall model. Journal of Fluid Mechanics, 942, p.R8.
204. Magill, J., Bachmann, M., Rixon, G. and McManus, K., 2003. Dynamic stall control using a model-based observer. Journal of Aircraft, 40(2), pp. 355-362.
205. Brunton, S.L., Noack, B.R. and Koumoutsakos, P., 2020. Machine learning for fluid mechanics. Annual Review of Fluid Mechanics, 52(1), pp.477-508.
206. Lombardi, A.J., Bowles, P.O. and Corke, T.C., "Closed-loop dynamic stall control using a plasma actuator," *AIAA Journal*, Vol. 51, No. 5, 2013, pp. 1130-1141. https://doi.org/10.2514/1.J051988.
207. Zalovcik, J.A., "Summary of stall-warning devices," NACA-TN-2676, 1952.
208. Williams, D.R., Greenblatt, D., Müller-Vahl, H., Santra, S. and Reißner, F., 2019. Feed-forward dynamic stall control model. AIAA Journal, 57(2), pp. 608-615.
209. An, X., Williams, D.R., Eldredge, J. and Colonius, T., 2016. Modeling dynamic lift response to actuation. In 54th AIAA Aerospace Sciences Meeting (p. 0058).
210. Williams, D.R., An, X., Iliev, S., King, R. and Reißner, F., 2015. Dynamic hysteresis control of lift on a pitching wing. Experiments in Fluids, 56, pp. 1-12.
211. Shyy, W., Berg, M. and Ljungqvist, D., 1999. Flapping and flexible wings for biological and micro air vehicles. Progress in aerospace sciences, 35(5), pp. 455-505.
212. Ansari, S.A., Żbikowski, R. and Knowles, K., 2006. Aerodynamic modelling of insect-like flapping flight for micro air vehicles. Progress in Aerospace Sciences, 42(2), pp.129-172.
213. Harvey, C., Gamble, L.L., Bolander, C.R., Hunsaker, D.F., Joo, J.J. and Inman, D.J., 2022. A review of avian-inspired morphing for UAV flight control. Progress in Aerospace Sciences, 132, p. 100825.
214. Shyy W, Lian Y, Tang J, Viieru D, Liu H. Aerodynamics of low Reynolds number flyers. New York, NY: Cambridge University Press; 2008.
215. Buchholz, J.H. and Smits, A.J., 2006. On the evolution of the wake structure produced by a low-aspect-ratio pitching panel. Journal of Fluid Mechanics, 546, pp. 433-443.

216. Ringuette, M.J., Milano, M. and Gharib, M., 2007. Role of the tip vortex in the force generation of low-aspect-ratio normal flat plates. Journal of Fluid Mechanics, 581, pp. 453-468.
217. Jones, A.R. and Babinsky, H., 2010. Unsteady lift generation on rotating wings at low Reynolds numbers. Journal of Aircraft, 47(3), pp. 1013-1021.
218. Taylor, G.K., Nudds, R.L. and Thomas, A.L., 2003. Flying and swimming animals cruise at a Strouhal number tuned for high power efficiency. Nature, 425(6959), pp. 707-711.
219. Heathcote, S., Wang, Z. and Gursul, I., 2008. Effect of spanwise flexibility on flapping wing propulsion. Journal of Fluids and Structures, 24(2), pp. 183-199.
220. Young, J. and Lai, J.C., 2007. Mechanisms influencing the efficiency of oscillating airfoil propulsion. AIAA Journal, 45(7), pp. 1695-1702.
221. Greenblatt, D. and Lautman, R., 2015. Inboard/outboard plasma actuation on a vertical-axis wind turbine. Renewable Energy, 83, pp. 1147-1156.
222. Greenblatt, D., Göksel, B., Rechenberg, I., Schule, C.Y., Romann, D. and Paschereit, C.O., 2008. Dielectric barrier discharge flow control at very low flight Reynolds numbers. AIAA Journal, 46(6), pp. 1528-1541.
223. Aono, H., Liang, F. and Liu, H., 2008. Near-and far-field aerodynamics in insect hovering flight: an integrated computational study. Journal of Experimental Biology, 211(2), pp. 239-257.
224. Dickinson, M. H., Lehmann, F.-O., & Sane, S. P. 1999. Wing rotation and the aerodynamic basis of insect flight. Science, 284(5422), 1954–1960.
225. Sun, M., & Tang, J. (2002). Unsteady aerodynamic force generation by a model fruit fly wing in flapping motion. JEB, 205, 55–70.
226. Sane, S. P. (2003). The aerodynamics of insect flight. Journal of Experimental Biology, 206(23), 4191–4208. https://doi.org/10.1242/jeb.00663
227. Altshuler, D. L., et al. (2005). Short-amplitude high-frequency wing strokes determine the aerodynamics of honeybee flight. PNAS, **102**(50), 18213–18218.
228. Combes, S. A., & Daniel, T. L. (2003). *Flexural stiffness in insect wings I. Scaling and the influence of wing venation. JEB,* **206**, 2979–2987.
229. Willmott, A. P., & Ellington, C. P. (1997). The mechanics of flight in the hawkmoth Manduca sexta I. Kinematics of hovering and forward flight. Journal of Experimental Biology, 200, 2705–2722.

230. Kruyt, J.W., Quicazán-Rubio, E.M., Van Heijst, G.F., Altshuler, D.L. and Lentink, D., 2014. Hummingbird wing efficacy depends on aspect ratio and compares with helicopter rotors. *Journal of the royal society interface*, *11*(99), p.20140585.
231. Vey, S., Nayeri, C., Paschereit, C. and Greenblatt, D., 2010. Plasma flow control on low aspect ratio wings at low Reynolds numbers. In 48th AIAA Aerospace Sciences Meeting Including the New Horizons Forum and Aerospace Exposition (p. 1222).
232. Vey, S., Greenblatt, D., Nayeri, C. and Paschereit, C., 2010. Leading edge and wing tip flow control on low aspect ratio wings. In 40th Fluid Dynamics Conference and Exhibit (p. 4865).
233. Vey, S., "Low aspect ratio wing flow control at low Reynolds numbers," Dr.-Ing. Dissertation, Technical University of Berlin, 2014.
234. Liu, H., 2009. Integrated modeling of insect flight: from morphology, kinematics to aerodynamics. Journal of Computational Physics, 228(2), pp. 439-459.
235. Dietl, J.M. and Garcia, E., 2008. Stability in ornithopter longitudinal flight dynamics. Journal of Guidance, Control, and Dynamics, 31(4), pp. 1157-1163.
236. Liggett, N.D. and Smith, M.J., 2012. Temporal convergence criteria for time-accurate viscous simulations of separated flows. Computers & Fluids, 66, pp.140-156.
237. Visbal, M.R., 2011. Numerical investigation of deep dynamic stall of a plunging airfoil. AIAA Journal, 49(10), pp. 2152-2170.
238. Lee, S. and Gross, A., 2024. Large-eddy simulations of dynamic stall for a NACA0012 wing section. In AIAA Scitech 2024 Forum (p. 1352).
239. Mohamed, K., Nadarajah, S. and Paraschivoiu, M., 2009. Detached-eddy simulation of a wing tip vortex at dynamic stall conditions. Journal of Aircraft, 46(4), pp.1302-1313.
240. Kim, T., Jee, S., Kim, M. and Sohn, I., 2023. Numerical investigation on high-speed jet actuation for transient control of flow separation. Aerospace Science and Technology, 135, p.108171.
241. Spalart, P.R., 2009. Detached-eddy simulation. Annual Review of Fluid Mechanics, 41(1), pp.181-202.
242. Eggert, C.A. and Rumsey, C.L., 2017. CFD study of NACA 0018 airfoil with flow control (No. NASA/TM-2017-219602).
243. Mishra, H. and Venayagamoorthy, S.K., 2024. On the turbulent viscosity parameter Cμ in the k–ϵ model. Flow, 4, p.E16.
244. Zhu, C., Chen, J., Wu, J. and Wang, T., 2019. Dynamic stall control of the wind turbine airfoil via single-row and double-row passive vortex generators. Energy, 189, p. 116272.

245. Mereu, R., Passoni, S. and Inzoli, F., 2019. Scale-resolving CFD modeling of a thick wind turbine airfoil with application of vortex generators: Validation and sensitivity analyses. *Energy*, *187*, p.115969.
246. Kawai, S., and Lele, S. K. (2010). "Large eddy simulation of VGs in turbulent boundary layers", J. Fluid Mech.
247. Slotnick, J.P., Khodadoust, A., Alonso, J., Darmofal, D., Gropp, W., Lurie, E. and Mavriplis, D.J., 2014. CFD vision 2030 study: A path to revolutionary computational aerosciences (No. NF1676L-18332).
248. Kerho, M., 2007. Adaptive airfoil dynamic stall control. Journal of aircraft, 44(4), pp. 1350-1360.
249. Joo, W., Lee, B.S., Yee, K. and Lee, D.H., 2006. Combining passive control method for dynamic stall control. Journal of aircraft, 43(4), pp. 1120-1128.
250. Visbal, M.R. and Garmann, D.J., 2023. Passive control of dynamic stall using a flow-driven micro-cavity actuator. Theoretical and Computational Fluid Dynamics, 37(3), pp. 289-303.
251. Ekaterinaris, J.A., 2002. Numerical Investigations of Dynamic Stall Active Control for Incompressible and Compressible Flows. Journal of Aircraft, 39(1), pp.71-78.
252. Ekaterinaris, J., Chandrasekhara, M. and Platzer, M., 2005. Recent developments in dynamic stall measurements, computations and control. In 43rd AIAA aerospace sciences meeting and exhibit (p. 1296).
253. Laufer, M., Frankel, S.H. and Greenblatt, D., 2022. GPU-Accelerated Implicit Large Eddy Simulation of a NACA 0018 Airfoil with Active Flow Control. In AIAA SCITECH 2022 Forum (p. 0471).
254. Sun, M. and Sheikh, S.R., 1999. Dynamic stall suppression on an oscillating airfoil by steady and unsteady tangential blowing. Aerospace science and technology, 3(6), pp. 355-366.
255. Rehman, A. and Kontis, K., 2006. Synthetic jet control effectiveness on stationary and pitching airfoils. Journal of aircraft, 43(6), pp. 1782-1789.
256. Ekaterinaris, J.A., 2004. Prediction of active flow control performance on airfoils and wings. Aerospace Science and Technology, 8(5), pp. 401-410.
257. Greenblatt, D., Paschal, K. B., Yao, C.-S., Harris, J., "A Separation Control CFD Validation Test Case, Part 2: Zero Efflux Oscillatory Blowing," AIAA Journal, Vol. 44, No. 12, 2006, pp. 2831-2845, https://doi.org/10.2514/1.19324.

258. Rumsey, C.L. and Greenblatt, D., 2009. Flow control predictions using unsteady Reynolds-averaged Navier-Stokes modeling: a parametric study. AIAA Journal, 47(9), pp. 2259-2262.
259. Suzen, Y., Huang, G., Jacob, J. and Ashpis, D., 2005. Numerical simulations of plasma based flow control applications. In 35th AIAA Fluid Dynamics Conference and Exhibit (p. 4633).
260. Corke, T.C., Post, M.L. and Orlov, D.M., 2009. Single dielectric barrier discharge plasma enhanced aerodynamics: physics, modeling and applications. Experiments in Fluids, 46, pp.1-26.
261. Orlov, D.M., 2006. Modelling and simulation of single dielectric barrier discharge plasma actuators (Doctoral dissertation, University of Notre Dame).
262. Chen, Z., Hao, L., and Zhang, B., "A model for nanosecond pulsed dielectric barrier discharge (NSDBD) actuator and its investigation on the mechanisms of separation control over an airfoil," Science China Technological Sciences, Vol. 56, 2013, pp. 1055–1065.
263. K. Takashima, Z. Yin, I.V. Adamovich. 2012. Measurements and kinetic modeling of energy coupling in volume and surface nanosecond pulse discharges, Plasma Sources Sci. T. 22 (1), 015013.
264. Noonan, K.W., 1991. Aerodynamic characteristics of a rotorcraft airfoil designed for the tip region of a main rotor blade (Vol. 4264). NASA, Scientific and Technical Information Division.
265. Brocklehurst, A. and Barakos, G.N., 2013. A review of helicopter rotor blade tip shapes. Progress in Aerospace Sciences, 56, pp. 35-74.
266. Gaitonde, D.V. and Adler, M.C., 2023. Dynamics of three-dimensional shock-wave/boundary-layer interactions. Annual Review of Fluid Mechanics, 55(1), pp. 291-321.
267. Chandrasekhara, M.S., Wilder, M.C. and Carr, L.W., 2001. Compressible dynamic stall control using dynamic shape adaptation. AIAA Journal, 39(10), pp. 2021-2024.
268. Chandrasekhara, M. S., Martin, P. B., and Tung, C., "Compressible Dynamic Stall Control Using a Variable Droop Leading Edge Airfoil," Journal of Aircraft, Vol. 41, No. 4, July-Aug, 2004, pp. 862-869.
269. Carr, L.W., Chandrasekhara, M.S., Wilder, M.C. and Noonan, K.W., 2001. Effect of compressibility on suppression of dynamic stall using a slotted airfoil. Journal of Aircraft, 38(2), pp. 296-309.

270. Beahan, J.J., Shih, C., Krothapalli, A., Kumar, R. and Chandrasekhara, M.S., 2014. Compressible dynamic stall control using high momentum microjets. Experiments in fluids, 55, pp. 1-11.
271. Nagib, H., Kiedaisch, J., Greenblatt, D., Wygnanski, I. and Hassan, A., 2001. Effective flow control for rotorcraft applications at flight mach numbers. In 15th AIAA Computational Fluid Dynamics Conference (p. 2974).
272. Wilbur, M.L., Mistry, M.P., Lorber, P.F., Blackwell Jr, R., Barbarino, S., Lawrence, T.H. and Arnold, U.T., 2018. Rotary wings morphing technologies: state of the art and perspectives. Morphing Wing Technologies, pp. 759-797.
273. Zhuang, N., Alvi, F.S., Alkislar, M.B. and Shih, C., 2006. Supersonic cavity flows and their control. AIAA Journal, 44(9), pp. 2118-2128.
274. Alvi, F.S., Lou, H., Shih, C. and Kumar, R., 2008. Experimental study of physical mechanisms in the control of supersonic impinging jets using microjets. Journal of Fluid Mechanics, 613, pp. 55-83.
275. Huang, W., Wu, H., Yang, Y.G., Yan, L. and Li, S.B., 2020. Recent advances in the shock wave/boundary layer interaction and its control in internal and external flows. Acta Astronautica, 174, pp. 103-122.
276. Roupassov, D.V., Nikipelov, A.A., Nudnova, M.M. and Starikovskii, A.Y., 2009. Flow separation control by plasma actuator with nanosecond pulsed-periodic discharge. AIAA Journal, 47(1), pp. 168-185.
277. Kelley, C.L., Bowles, P.O., Cooney, J., He, C., Corke, T.C., Osborne, B.A., Silkey, J.S. and Zehnle, J., 2014. Leading-edge separation control using alternating-current and nanosecond-pulse plasma actuators. AIAA Journal, 52(9), pp. 1871-1884.
278. Starikovskiy, A. and Miles, R.B., 2018. Helicopter lift force increase in hover mode by NS-SDBD plasma actuators. In 2018 AIAA Aerospace Sciences Meeting (p. 0936).
279. Visbal, M.R. and Garmann, D.J., 2024. Structure of the Compressible Laminar Separation Bubble on a Stationary Airfoil. In AIAA Scitech 2024 Forum (p. 0074).
280. Polonsky, D., Keisar, D. and Greenblatt, D., 2021. Rotor Performance Enhancement Using Pulsed Plasma Actuation. AIAA Journal, 59(8), pp. 3275-3280.
281. Polonsky, D., Stalnov, O. and Greenblatt, D., 2023. Noise reduction on a model helicopter rotor using dielectric barrier discharge plasma actuators. AIAA Journal, 61(7), pp. 3134-3141.